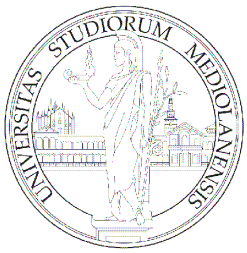

UNIVERSITÀ DEGLI STUDI DI MILANO
FACOLTÀ DI SCIENZE MATEMATICHE, FISICHE E NATURALI
DOTTORATO DI RICERCA IN
FISICA, ASTROFISICA E FISICA APPLICATA

AB INITIO APPROACH TO DENSITY RESPONSE AND EXCITATION SPECTRA IN METALLIC SYSTEMS

Settore Scientifico disciplinare FIS/03

Coordinatore: Prof. Gianpaolo Bellini
Tutore: Prof. Giovanni Onida

Tesi di Dottorato di:
Marco Cazzaniga
Ciclo XXI

Anno Accademico 2008-2009

Contents

Introduction

In the last decade, the *ab-initio* approach has become a standard theoretical tool to investigate the excited states of solids and molecules. Most *ab-initio* methods are based on the DFT (the Hohenberg-Kohn-Sham density-functional theory) [1], which is an exact method to predict the ground state properties. However, methods on the many body perturbation theory (MBPT) can also be based on standard Hartree-Fock descriptions. Several approaches are suitable to interpret different experimental results: for example, the *GW* approximation and the TDDFT (the time-dependent extension of the DFT) [2]. The *GW* approach describes the single quasiparticle excitation more accurately than the Kohn-Sham eigenvalues: the agreement with photoemission experiments is improved and, in addition, also finite quasiparticle lifetimes can be described. Similarly, TDDFT permits the theoretical interpretation of dielectric properties of a wide range of materials: from atoms, to surfaces and nanostructures. For these reasons a quite large effort has been spent in the simulation of dielectric properties of semiconductors. The successes obtained in describing bulk silicon [3, 4, 5] (usually chosen as benchmark system) pushed toward the application of these method to more complex systems, like surfaces or materials of technological applications.

The homogeneous electron gas (HEG) [6, 7] is a system widely studied by the scientific community. The simplicity of this model of electrons moving in an uniform positive background (the jellium) allows one to investigate very complex theories and approximations. By exploiting the translational invariance the equations can be strongly simplified. Although the HEG does not exist in nature, the possibility to perform complex calculations that can be compared with the realistic nearly free-electron metals makes this system of crucial importance.

The HEG does not take into account the presence of the periodic ionic structure typical of real metals. This applies to system with a complex electronic structure like the transition metals, and also to simple metals like Al, Na or K. Band structure effects are able to introduce new features not described by the HEG already when the correlation are dealt at the simplest level. This explains the reason of the interest in performing full *ab initio* calculation of excited-state properties of realsistic metallic systems. Despite they are close to the HEG the calculations for metals are more complicated than the ones of semiconductors. The main challenge is due to the presence of electronic transitions between states very close to the Fermi surface (intraband transitions), which add an additional difficulty compared to the case of semiconductors. The inclusion of these transitions in the response function is a still debated problem and

a standard solution has not been proposed yet. The few available studies introduce the intraband metallic contribution to the dielectric response mainly using a simplified Drude model, where only the plasma frequency is computed *ab initio* [8].

I faced this problem for the first time during my master thesis [9], where I was interested in jellium surface as a model for metallic surfaces. This project could not be completed, because, while performing a serie of tests, I discovered the unexpected and unphysical opening of a gap in the band structure of the metallic surface. We traced back this effect to the incorrect evaluation of the screening that was lacking of the intraband contributions. This motivated our interest in understanding how these systems can be simulated and how calculations compare with experiments.

In this thesis I propose a detailed discussion of the calculation of the dielectric response of metallic systems. We mainly performed simulations of Al and Na, since their near free-electron like behaviour permits also a comparison with the results of the HEG model. On the other hand, we also explored the possibility that our methods could be applied to more complex system. In this direction we performed calculation of the optical properties of ferromagnetic Fe, which includes the additional complexity of the presence of the *3d* electrons. We also tried to understand if the accuracy of *ab initio* calculations in the case of semiconductors can be extended to metallic systems.

The present thesis focuses on the frequency-dependent dielectric function $\epsilon(\mathbf{q}, \omega)$. In the first part of this thesis we review briefly the *GW* and TDDFT approaches used in our calculations. We will also motivate the study of bulk metals. In the second part of this thesis the new methods developed in this work do deal with the intraband contributions will be described. We will finally analyze the obtained results.

In the discussion of the *GW* calculations for metals, we propose a method to deal with the intraband term based on a fit of the finite-momentum screened interaction. This methods works efficiently when the plasmon pole approximation is an accurate assumption.

In addition to optical adsorption, other experiments permit to access the dielectric properties of metals, including the energy-loss spectroscopy and inelastic X-ray scattering spectroscopy (IXSS). In the present thesis we performed a systematic calculation of the dynamic structure factor of Na and Al to understand the role of electronic correlation beyond the random phase approximation (RPA). We perform TDDFT simulations using several exchange and correlation kernels and including quasiparticle effects, to understand how they are important to provide a satisfactory theoretical description of the experimental measurements. TDDFT is not only able to predict loss function measurements, but also optical properties. This thesis address also that problem proposing a new method to deal with the intraband transitions, method applied to Al chosen as benchmark and to ferromagnetic Fe.

In Chapter 1 we introduce the many-body problem, which is described in detail in Chapter 2, where we review the many-body perturbation theory and the *GW* approximation. In Chapter 3 the TDDFT and the linear response formalism are presented. We introduce the dielectric function and briefly discuss its main features in Chapter 4. In Chapter 5 we show the applications, by presenting the problem of the fictitious

gap introduced by the *GW* corrections and by proposing a fit on the polarizability to deal with the intraband transitions. We apply finally TDDFT, by discussing the IXSS spectra of Na and of Al in Chapter 6. Optical properties are discussed in Chapter 7.

Part I

Theoretical framework

Chapter 1

The many-body problem

To describe *ab initio* the macroscopic properties of condensed matter, one needs the following Hamiltonian which depends on a large number of degrees of freedom:

$$\begin{aligned} H(\{\mathbf{R}\},\{\mathbf{r}\}) &= T_e + T_I + V_{ee} + V_{eI} + V_{II} = \\ &= \sum_{i=1}^{N_e} -\frac{\nabla_i^2}{2} + \sum_{I=1}^{N_I} -\frac{\nabla_I^2}{2M_I} + \frac{1}{2}\sum_{i\neq j}\frac{1}{|\mathbf{r}_i - \mathbf{r}_j|} + \\ &- \sum_{i=1}^{N_e}\sum_{n=1}^{N_I}\frac{Z_n}{|\mathbf{R}_n - \mathbf{r}_i|} + \frac{1}{2}\sum_{n\neq m}\frac{Z_n Z_m}{|\mathbf{R}_n - \mathbf{R}_m|}. \end{aligned} \tag{1.1}$$

where atomic units has been adopted: $\hbar = e = m_e = 4\pi\epsilon_0 = 1$. In such an Hamiltonian there are five contributions: the kinetic energy of the electrons (whose coordinate are labelled by $\mathbf{r}$) T_e , that of the ions ($\mathbf{R}$) T_I, the electron-electron Coulomb repulsion V_{ee}, the electron-ion attraction V_{eI} and the repulsion of the ions V_{II}.

The determination of the eigenstates of H constitutes a formidable task because of the very high number of variables involved[1]. Moreover the interaction between particles makes impossible to separate the original problem in a set of simpler ones. For these reasons one must introduce several approximations in order to make such a problem treatable, and to obtain reliable theoretical predictions of electronic properties of condensed matter.

1.1 The Born-Oppenheimer separation

The first approximation that is widely used aims to separate the ionic problem from the electronic one. This is possible because the electronic mass is three orders of magnitude smaller than the ionic one. From this it follows that the characteristic time connected with the electronic motion is of the order of $10^{-15}\,\mathrm{s} \div 10^{-16}\,\mathrm{s}$, smaller than the one for the ionic motion, of the order of $10^{-12}\,\mathrm{s}$.

[1]One passes from a few tens degrees of freedom for an atom or a small molecule to a number comparable to the Avogadro number for a real solid.

These arguments motivate the use of the Born-Oppenheimer separation where the eigenfunction of the entire many-body problem is written as the product of an electronic part (depending only parametrically on the ions position) times a ionic one:

$$\Upsilon(\{\mathbf{R}\},\{\mathbf{r}\}) = \Phi_I(\{\mathbf{R}\})\Psi_{\{\mathbf{R}\}}(\{\mathbf{r}\}). \tag{1.2}$$

This assumption neglects the electron-ion overlap in the original problem, in such a way to introduce two partially separate equations of motion:

$$\left[T_e + V_{ee} + V_{ext\,\{\mathbf{R}\}}\right]\Psi_{\{\mathbf{R}\}}(\{\mathbf{r}\}) = E^e_{\{\mathbf{R}\}}\Psi_{\{\mathbf{R}\}}(\{\mathbf{r}\}) \tag{1.3}$$

$$T_I\Phi_I(\{\mathbf{R}\}) + [V_{II}(\{\mathbf{R}\}) + E^e_{\{\mathbf{R}\}}]\Phi_I(\{\mathbf{R}\}) = E_{TOT}\Phi_I(\{\mathbf{R}\}), \tag{1.4}$$

where we have called V_{ext} the electron-ion interaction at fixed ions position.

1.2 The electronic problem

Although the problem is largely simplified thanks to the reduction of the number of the degrees of freedom due to the exclusion of the ionic motion, it still remains challenging. The electronic wave functions are still depending on the electronic coordinates, which make the problem impossible to be treated by using brute force methods. To overcome this difficulty other approximations have been proposed. Two of the most used approaches are the Hartree-Fock approximation and the density functional theory (DFT), which are sketched in the following sections.

1.2.1 The Hartree-Fock approximation

One of the standard approximation used to treat the fully interacting electronic Hamiltonian is the Hartree-Fock approximation. In this approach one makes the assumption that the electrons moves in a mean filed generated by all electrons with, in addition, the correlations induced by the Pauli principle. Under these assumptions, the electronic many-body eigenfunction reduces to a Slater determinant of single-electron wavefunctions:

$$\Psi(\{\mathbf{r}\}) = \frac{1}{\sqrt{N!}}\sum_{i=1}^{N!}(-1)^{P_i}\phi_1(\mathbf{r}_{P_i(1)})\phi_2(\mathbf{r}_{P_i(1)}).....\phi_N(\mathbf{r}_{P_i(N)}) \tag{1.5}$$

where P_i is a permutation of the single-particle wavefunction indexes and the factor $(-1)^{P_i}$ takes in account the sign due to odd or even permutations.

With this assumption it is possible to write the total energy of the system as:

$$\begin{aligned} E^{e\,(HF)} &= \sum_{i=1}^{N}\int d^3r\phi_i^*(\mathbf{r})\left(-\frac{\nabla^2}{2}\phi_i(\mathbf{r})\right) + \sum_{i=1}^{N}\int d^3r|\phi_i(\mathbf{r})|^2V_{ext}(\mathbf{r}) + \\ &+ \frac{1}{2}\sum_{i,j}\int d^3rd^3r'\frac{|\phi_i(\mathbf{r})|^2|\phi_j(\mathbf{r}')|^2}{|\mathbf{r}-\mathbf{r}'|} - \frac{1}{2}\sum_{i,j}\int d^3rd^3r'\frac{\phi_i^*(\mathbf{r})\phi_i(\mathbf{r}')\phi_j(\mathbf{r})\phi_j^*(\mathbf{r}')}{|\mathbf{r}-\mathbf{r}'|} = \\ &= T + E_{ext} + E_H + E_X. \end{aligned} \tag{1.6}$$

In this expression the first term is the kinetic contribution, the second is the interaction with the external potential, E_H is the Hartree energy (interaction of an electron with the field generated by all electrons) and E_X is the exchange one (the term that takes into account the Pauli principle).

By applying the variational principle, imposing the orthonormality of the ϕ_i orbitals, it is possible to deduce the following set of equations for the single electron wavefunctions:

$$-\frac{\nabla^2}{2}\phi_i(\mathbf{r}) + V_{ext}(\mathbf{r})\phi_i(\mathbf{r}) + V_H([n],\mathbf{r})\phi_i(\mathbf{r}) + \int d^3r"\,\phi_i(\mathbf{r}")V_X(\mathbf{r},\mathbf{r}",[\tilde{n}]) = \epsilon_i\phi_i(\mathbf{r}). \quad (1.7)$$

where $V_H = \int d^3r' \frac{n(\mathbf{r}')}{|\mathbf{r}-\mathbf{r}'|}$ and $V_X = \int d^3r' \frac{\tilde{n}(\mathbf{r}')}{|\mathbf{r}-\mathbf{r}'|}$ are the Hartree and the exchange potential coming from the functional derivatives of the corresponding energies with respect to $\phi_i^*(\mathbf{r})$, $n(\mathbf{r})$ is the electron density $n(\mathbf{r}) = \sum_j |\phi_j(\mathbf{r})|^2$ and $\tilde{n}(\mathbf{r},\mathbf{r}') = \sum_j \phi_j(\mathbf{r})\phi_j^*(\mathbf{r}')$.

It is important to notice that the total energy of the system is not the mere summation of the eigenvalues since the Hartree and the exchange contributions would be counted twice; the total energy is given instead by:

$$E^{e\,(HF)} = \sum_i \epsilon_i - \frac{1}{2}E_H - \frac{1}{2}E_X. \quad (1.8)$$

1.2.2 The Density Functional Theory

The Density Functional Theory (DFT) [1] is based on a completely different approach to the many-body problem. Instead of considering the electronic ground-state eigenfunction as key quantity, the central role is assumed by the ground-state density $n(\mathbf{r})$. This permits a great simplification of the problem since $n(\mathbf{r})$ depends only on one set of spatial coordinates.

The starting point of this framework is the Hohenberg and Kohn (HK) theorem that states the existence of a biunivocal correspondence between the ground-state electron density and the corresponding external potential [10]. A consequence of this theorem is the possibility of writing the ground-state energy as a functional of the density only, once an external potential $V_{ext}(\mathbf{r})$ is chosen:

$$E^{e\,(HK)}[n(\mathbf{r}); v_{ext}(\mathbf{r})] = \langle\psi_G[n(\mathbf{r})]|T + V_{ee} + V_{ext}|\psi_G[n(\mathbf{r})]\rangle. \quad (1.9)$$

This is because the ground-state wavefunction is univocally identified once the density is given. Moreover it is possible to rewrite the HK functional as:

$$E^{e\,(HK)}[n(\mathbf{r}); v_{ext}(\mathbf{r})] = T[n(\mathbf{r})] + V_{ee}[n(\mathbf{r})] + \int d^3r[n(\mathbf{r})]_{ext}(\mathbf{r})n(\mathbf{r}). \quad (1.10)$$

The peculiarity of this functional is that the first two terms are universal, i.e. independent on the specific system. To this functional it is possible to apply the variational principle which implies that $E^{(HK)}$ assumes the minimum value when $\psi_G[n(\mathbf{r})]$ is in the ground state.

This theorem makes also possible the introduction of an auxiliary system of non interacting electrons [11] with the same density (and by consequence the same ground-state energy) of the real system, since it establishes the existence and unicity of an unknown external potential for the non interacting case that produces a density equal to the one of the original problem. The advantage of this operation is due to the fact that the eigenfunction of this auxiliary system is nothing else that a Slater determinant of single-electron orbitals. This auxiliary system permits also to simplify the energy functional, which becomes:

$$E^{e\,(HK)}[n(\mathbf{r}); v_{ext}(\mathbf{r})] = T_0[n(\mathbf{r})] + E_H + E_{XC}[n(\mathbf{r})] + \int d^3r V_{ext}(\mathbf{r}) n(\mathbf{r}), \qquad (1.11)$$

where in the exchange and correlation energy E_{XC} are placed all the differences between the kinetic term of non interacting particles and the kinetic energy of real electrons and between the Hartree energy and the actual electron-electron interaction. By applying the variational procedure to this functional one deduces the following Kohn-Sham set of equations

$$\left[-\frac{\nabla^2}{2} + V_{ext}(\mathbf{r}) + V_H(\mathbf{r}) + V_{XC}(\mathbf{r})\right] \phi_i = \epsilon_i \phi_i, \qquad (1.12)$$

where V_{XC} is the functional derivative of E_{XC} with respect to the density.

Once this set of equations is solved, it is possible to compute the total energy:

$$E^{e\,(KS)} = \sum_i \epsilon_i - \frac{1}{2}\sum_{i,j} \left\langle \phi_i\phi_j | \frac{1}{|\mathbf{r}_i - \mathbf{r}_j|} | \phi_i\phi_j \right\rangle + E_{XC}[n(\mathbf{r})] - \int d^3r V_{XC}(\mathbf{r}) n(\mathbf{r}). \qquad (1.13)$$

However the functional E_{XC} is still unknown. In practice, although DFT is in principle exact, one needs to make an approximation for E_{XC} in order to get an expression for this functional. One simple and widely used approximation is the local density approximation (LDA). In the LDA the E_{XC} chosen is taken locally equal to the one of an homogeneous electron gas with the same density:

$$E_{XC}^{(LDA)}[n(\mathbf{r})] = \int d^3r \epsilon_{XC}[n(\mathbf{r})] n(\mathbf{r}). \qquad (1.14)$$

Here, $\epsilon_{XC}[n(\mathbf{r})]$ is the many-body exchange and correlation per particle of a uniform electron gas. This approximation is particularly well justified in systems with slowly varying densities.

To determine ϵ_{XC} it is necessary to solve accurately the fully interacting uniform electron gas problem, and this is far from being trivial: in practice the starting point for its evaluation usually are the simulations made by Ceperley and Adler with Monte Carlo methods [12]. Based on these computations, different parameterizations of ϵ_{XC} have been proposed, e.g. the one given by Perdew and Zunger [13]. Other parameterizations consider spin polarized systems [14, 15]. In addition, more complex approximation for E_{XC} are available, like the generalized gradient approximations (GGA) [16]. The DFT formalism is reviewed in Ref. [1] and the numerical algorithm used for simulations can be found in Ref. [17]

Table 1.1: Wigner-Seitz radius for selected metals [18].

element	Li	Na	K	Cu	Al
r_S (a_0)	3.25	3.93	4.86	2.67	2.07

1.3 The homogeneous electron gas

The simplest model, that can be used as a first approximation to model the properties of a metal, is the homogeneous electron gas (HEG) or jellium model. The HEG model consists of a gas of electrons immerged in a uniform positive charge. In practice this charged background removes the $\mathbf{q} \neq 0$ component of the external potential V_{ext} produced by the ionic lattice. The resulting interacting system is translational invariant which permits to determinate analytically different properties.

In the HEG the electron density is constant, and it is often described by the parameter r_S (the Wigner-Seitz radius). r_S is related to background density (which in the homogeneous case is equal to the electron one) $n = \frac{N}{V}$ through the relation:

$$\frac{1}{n} = \frac{4\pi r_S^3}{3} \tag{1.15}$$

By considering only the conduction electron, r_S usually varies between 2 a_0 and 4 a_0. It can be as large as 6 a_0 for the heavy alkalis. In table 1.1 we report the r_S value for a few metals.

The presence of the uniform positive background with the same density of the electrons induces a cancellation of the electron-background with background-background interaction and the Hartree term. This means the resulting energy being only kinetic, therefore positive. As a consequence in the Hartree approximation the HEG is not bounded. The exchange and correlation energy comes to be necessary to yield negative energies per particle. Specifically in the Hartree-Fock approximation the total energy per particle is $\frac{3}{10}\left(\frac{9\pi}{4}\right)^{2/3}\frac{1}{r_S^2} - \frac{3}{4\pi}\left(\frac{9\pi}{4}\right)^{1/3}\frac{1}{r_S}$. On the other hand in DFT A constant density implies that a constant exchange and correlation potential with a resulting total energy per particle equal to the free electron kinetic term $\frac{3}{10}\left(\frac{9\pi}{4}\right)^{2/3}\frac{1}{r_S^2}$, diminished by ϵ_{XC}. By definition TDLDA is exact for the HEG.

Chapter 2

The many-body perturbation theory

In this chapter we present a different way approach to the many body problem ed on a perturbation theory. In such a scheme the Hartree-Fock approximation corresponds to the $1^{\mathtt{st}}$ order term of the expansion in the bare Coulomb potential. In this case the key variable is not the complicate many-body wave function, but a quantity that contains less informations: the Green's function.

2.1 The Green's function

The single particle Green's function is defined as the ground-state $|\Psi_{GS}\rangle$ expectation value ground state of the time-ordered product of a creation and of an annihilation field operator:

$$\begin{aligned} iG(1,2) &= \langle\Psi_{GS}|T[\hat{\psi}(1)\hat{\psi}^{\dagger}(2)]|\Psi_{GS}\rangle = \\ &= \theta(t_1-t_2)\langle\Psi_{GS}|\hat{\psi}(1)\hat{\psi}^{\dagger}(2)|\Psi_{GS}\rangle + \\ &- \theta(t_2-t_1)\langle\Psi_{GS}|\hat{\psi}^{\dagger}(2)\hat{\psi}(1)|\Psi_{GS}\rangle \end{aligned} \tag{2.1}$$

where generalized index 1 refers to the spatial, temporal and spin coordinates $(\mathbf{r}_1, t_1, \sigma_1)$, T is the time ordering operator and $\psi(1)$ and $\psi^{\dagger}(2)$ are the annihilation and creation field operators respectively. The Green's function can be interpreted as the amplitude connected with the propagation of an electron created at $(\mathbf{r}_2, t_2)$ and annihilated at $(\mathbf{r}_1, t_1)$ if $t_1 > t_2$, when $t_1 < t_2$ G describes the propagation of a hole.

Once G is known it is possible to calculate the expectation values of any single particle operator $\hat{O} = \int d1d2\, \delta(t_2 - t_1)\hat{\psi}^{\dagger}(1)O(1,2)\hat{\psi}(2)$:

$$\begin{aligned} \langle\Psi_{GS}|\hat{O}|\Psi_{GS}\rangle &= \int d1d2\delta(t_2-t_1)O(1,2)\langle\Psi_{GS}|\hat{\psi}^{\dagger}(1)\hat{\psi}(2)|\Psi_{GS}\rangle = \\ &= -i\int d1d2\delta(t_2-t_1^{+})O(1,2)G(2,1) \end{aligned} \tag{2.2}$$

where $t_1^+ = t_1 + \eta$ with η an infinitesimum. It is also possible to compute the total energy thanks to the Galitskii-Migdal equation [19]:

$$E^e = -\frac{i}{2}\sum_{\sigma_1,\sigma_2}\delta_{\sigma_1,\sigma_2}\int \lim_{\mathbf{r_2}\to\mathbf{r_1}}\lim_{t_2\to t_1^+}\left[i\frac{\partial}{\partial t_1} + h_0(\mathbf{r}_1)\right]G(1,2)d^3r_1 \tag{2.3}$$

where $h_0 = \frac{\nabla^2}{2} + V_{ext}$ is the single-particle Hamiltonian.

2.1.1 The independent particle Green's function

In case of non interacting fermions the Green's function can be calculated exactly. In this case the field operators, comparing in the definition, can be rewritten in the basis of creator and annihilator operators of the single particle states of h_0, $|n\rangle$ with energy E_n :

$$\hat{\psi}_\sigma(\mathbf{r},t) = \sum_n \hat{c}_n(t)\langle \mathbf{r},\sigma|n\rangle. \tag{2.4}$$

Thanks to this transformation the Green's function becomes:

$$\begin{aligned} iG(1,2) = \sum_{n,m}\langle \mathbf{r}_1,\sigma_1|n\rangle\langle m|\mathbf{r}_2,\sigma_2\rangle e^{-iE_nt_1+iE_mt_2} \qquad & \big[\theta(t_1-t_2)\langle\Psi_{GS}|\hat{c}_n\hat{c}_m^\dagger|\Psi_{GS}\rangle + \\ - \quad & \theta(t_2-t_1)\langle\Psi_{GS}|\hat{c}_m^\dagger\hat{c}_n|\Psi_{GS}\rangle\big] \end{aligned} \tag{2.5}$$

In the more special case non interacting HEG the natural space where describe the system is the momentum one and the matrix element $\langle \mathbf{r},\sigma|n\rangle$ are nothing else than plane waves. This permits to simplify further the expression (2.5) becomes:

$$iG_0(1,2) = \frac{e^{i\mathbf{k}\cdot(\mathbf{r}_1-\mathbf{r}_2)-i\epsilon_\mathbf{k}(t_1-t_2)}}{(2\pi)^3}\left[\theta(t_1-t_2)\theta(|\mathbf{k}|-k_F) - \theta(t_2-t_1)\theta(k_F-|\mathbf{k}|)\right]. \tag{2.6}$$

2.2 The Lehmann representation of the Green's function

If the Hamiltonian does not contain any term which depends explicitly on the time, it can be shown that the Green's function will depend only on the difference of the time coordinates $(t_1 - t_2)$. This makes it possible to write G in frequency space by means of a Fourier transform [20].

The starting point is Eq. (2.1) that we rewrite as:

$$\begin{aligned} iG(1,2) = & \sum_{\Psi_n^{N+1}}\theta(t_1-t_2)e^{-i(E_n^{N+1}-E_{GS}^N)(t_1-t_2)}\langle\Psi_{GS}^N|\hat{\psi}_\alpha(\mathbf{r}_1)|\Psi_n^{N+1}\rangle\langle\Psi_n^{N+1}|\hat{\psi}_\beta^\dagger(\mathbf{r}_2)|\Psi_{GS}^N\rangle + \\ & + \sum_{\Psi_n^{N-1}}\theta(t_2-t_1)e^{-i(E_n^{N-1}-E_0^N)(t_1-t_2)}\langle\Psi_{GS}^N|\hat{\psi}_\beta^\dagger(\mathbf{r}_2)|\Psi_n^{N-1}\rangle\langle\Psi_n^{N-1}|\hat{\psi}_\alpha(\mathbf{r}_1)|\Psi_{GS}^N\rangle \end{aligned} \tag{2.7}$$

where Ψ^N_{GS} is the N particles ground state and Ψ^{N+1}_n and Ψ^{N-1}_n are general states respectively of $N+1$ and $N-1$ particles, with energies E^N_{GS}, E^{N+1}_n and E^{N-1}_n.

At this point we observe that $\theta(t_1 - t_2) = \lim_{\eta\to 0} \frac{i}{2\pi} \int_{-\infty}^{\infty} d\omega \frac{e^{i\omega(t_1-t_2)}}{\omega+i\eta}$. As a consequence the Fourier transform of G is:

$$\begin{aligned} G(\mathbf{r}_1, \mathbf{r}_2, \omega) &= \sum_{\Psi^{N+1}_n} \frac{\langle \Psi^N_{GS}|\hat{\psi}_\alpha(\mathbf{r}_1)|\Psi^{N+1}_n\rangle\langle\Psi^{N+1}_n|\hat{\psi}^\dagger_\beta(\mathbf{r}_2)|\Psi^N_{GS}\rangle}{\omega - (E^{N+1}_n - E^N_0) + i\eta} + \\ &+ \sum_{\Psi^{N-1}_n} \frac{\langle \Psi^N_{GS}|\hat{\psi}^\dagger_\beta(\mathbf{r}_2)|\Psi^{N-1}_n\rangle\langle\Psi^{N-1}_n|\hat{\psi}_\alpha(\mathbf{r}_1)|\Psi^N_{GS}\rangle}{\omega + (E^{N-1}_n - E^N_0) - i\eta} \end{aligned} \tag{2.8}$$

which is known as Lehmann representation of the Green's function. By redefining the matrix elements and the energy differences [6]:

$$\begin{cases} f_j(\mathbf{r}) = \langle \Psi^N_{GS}|\hat{\psi}_\sigma(\mathbf{r})|\Psi^{N+1}_n\rangle & \epsilon_j = E^{N+1}_n - E^N_0 \quad \epsilon_j \geq \mu \\ f_j(\mathbf{r}) = \langle \Psi^{N-1}_n|\hat{\psi}_\sigma(\mathbf{r})|\Psi^N_{GS}\rangle & \epsilon_j = E^N_0 - E^{N-1}_n \quad \epsilon_j < \mu, \end{cases} \tag{2.9}$$

Eq. (2.8) can be further simplified as:

$$G(\mathbf{r}_1, \mathbf{r}_2, \omega) = \sum_j \frac{f_j(\mathbf{r}) f^*_j(\mathbf{r}')}{\omega - \epsilon_j + i\eta} + \sum_j \frac{f_j(\mathbf{r}) f^*_j(\mathbf{r}')}{\omega - \epsilon_j - i\eta}. \tag{2.10}$$

2.3 The Green's function expansion and the Dyson's equation

As pointed out before the knowledge of the full interacting Green's function permits to calculate exactly different observables. Nevertheless the determination of G is as complicate as the solution of the full interacting Hamiltonian. The advantage in approaching the many-body problem by means of the Green's function formalism is the possibility of write a perturbative expansion for this function. In this section the basics for writing such expansion will be presented.

2.3.1 The Gell-Mann and Law theorem

In the Shrödinger picturethe time evolution of an eigenfunction $\psi(0)$ is expressed as $\hat{U}(t)\psi(0)$, where $U(t)$ is the time evolution operator. In the interaction picture a slightly different approach is preferred: only the evolution due the external perturbing potential V is included in the operatorial part, while the evolution due to the unperturbed Hamiltonian is retained on the eigenfunction. It is than possible to introduce a generalized time evolution operator $\hat{U}(t, t')$ which satisfies the following equation of motion:

$$\frac{\partial}{\partial t}\hat{U}(t, 0) = -iV(t)\hat{U}(t, 0), \tag{2.11}$$

with initial condition $\hat{U}(0,0) = \mathbb{I}$. The solution of Eq. (2.11) can be formally written as:

$$\begin{aligned}\hat{U}(t,0) &= \mathbb{I} + \sum_{k=1}^{\infty}(-i)^k \int_0^t dt_1 \int_0^{t_1} dt_2 ... \int_0^{t_{k-1}} dt_k \left[T\left(V(t_1)V(t_2)...V(t_k)\right)\right] = \\ &= T\exp\left[-i\int_{t'}^{t} d\tau V(\tau)\right]. \end{aligned} \tag{2.12}$$

From Eq. (2.12) it can be shown that the generic evolution is $\hat{U}(t,t') = \hat{U}(t,0)\hat{U}^{\dagger}(t',0)$.

We consider now the Hamiltonian

$$H = H_0 + e^{-\epsilon|t|}V, \tag{2.13}$$

that connects with a slow time evolution (one is interested in the limit $\epsilon \to 0$) the unperturbed Hamiltonian ($t \to \pm\infty$) with the full interacting one ($t \to 0$). We are interested a state $|\Psi^{\pm}\rangle$ which evolves from $\pm\infty$ to 0:

$$|\Psi^{\pm}\rangle = \frac{\hat{U}(0,\pm\infty)|\Psi_0\rangle}{\langle\Psi_0|\hat{U}(0,\pm\infty)|\Psi_0\rangle} \tag{2.14}$$

where Ψ_0 is an eigenstate of the unperturbed Hamiltonian H_0. The Gell-Mann and Law theorem [21] states that $|\Psi^{\pm}\rangle$ is an eigenstate of the full interacting Hamiltonian $H = H +_0 V$. Under the assumption the evolution is adiabatic, and that the ground state is reasonably lower in energy than the excited ones, the ground state of H_0 has no other choice than evolve to the ground state of the interacting system.

In conclusion it is possible to write the Green's function as:

$$iG(1,2) = \frac{\langle\Psi^0_{GS}|T[\hat{U}(-\infty,t_1)\hat{\psi}(1)\hat{U}(t_1,t_2)\hat{\psi}^{\dagger}(2)\hat{U}(t_2+\infty)]|\Psi^0_{GS}\rangle}{\langle\Psi^0_{GS}|S|\Psi^0_{GS}\rangle}, \tag{2.15}$$

where $S = \hat{U}(-\infty,+\infty)$. With some algebra the previous equation can be simplified as:

$$iG(1,2) = \frac{\langle\Psi^0_{GS}|T[S\hat{\psi}(1)\hat{\psi}^{\dagger}(2)]|\Psi^0_{GS}\rangle}{\langle\Psi^0_{GS}|S|\Psi^0_{GS}\rangle}. \tag{2.16}$$

2.3.2 The Wick's theorem

If we consider the expansion of the operator S according to Eq. (2.12) it is possible to write an expansion for the Green's function, Eq. (2.16), as:

$$\begin{aligned} & iG_{\sigma,\sigma'}(\mathbf{r}t,\mathbf{r}'t') = \\ = \; & \frac{\sum_{n=0}^{\infty}\frac{(-i)^n}{n!}\int_{-\infty}^{\infty} dt_1..dt_n\langle\Psi^0_{GS}|T[V(t_1)..V(t_n)\hat{\psi}_{\sigma}(\mathbf{r}t)\hat{\psi}^{\dagger}_{\sigma'}(\mathbf{r}'t')]|\Psi^0_{GS}\rangle}{\sum_{n=0}^{\infty}\frac{(-i)^n}{n!}\int_{-\infty}^{\infty} dt_1..dt_n\langle\Psi^0_{GS}|T[V(t_1)..V(t_n)]|\Psi^0_{GS}\rangle}. \end{aligned} \tag{2.17}$$

If we replace the interaction potential with its second quantization expression:

$$V(t) = \frac{1}{2}\sum_{\sigma_1,\sigma_2}\int d^3r_1 d^3r_2 \hat{\psi}^\dagger_{\sigma_1}(\mathbf{r}_1,t)\hat{\psi}^\dagger_{\sigma_2}(\mathbf{r}_2,t)v_C(\mathbf{r}_1-\mathbf{r}_2)\hat{\psi}_{\sigma_2}(\mathbf{r}_2,t)\hat{\psi}_{\sigma_1}(\mathbf{r}_1,t). \quad (2.18)$$

Eq. (2.17) generates an expansion of the Green's function in terms of the Coulomb potentials and of the field operators. For example the numerator `Num` of Eq. (2.17) results:

$$\begin{aligned} \texttt{Num} &= \langle\Psi^0_{GS}|T[\hat{\psi}_\sigma(\mathbf{r}t)\hat{\psi}^\dagger_{\sigma'}(\mathbf{r}'t')]|\Psi^0_{GS}\rangle + \quad (2.19)\\ &- i\int_{-\infty}^{\infty} dt_1 \sum_{\sigma_1,\sigma_2}\int d^3r_1 d^3r_2 v_C(\mathbf{r}_1-\mathbf{r}_2)\\ &\quad \langle\Psi^0_{GS}|T[\hat{\psi}^\dagger_{\sigma_1}(\mathbf{r}_1,t)\hat{\psi}^\dagger_{\sigma_2}(\mathbf{r}_2,t)\hat{\psi}_{\sigma_2}(\mathbf{r}_2,t)\hat{\psi}_{\sigma_1}(\mathbf{r}_1,t)\hat{\psi}_\sigma(\mathbf{r}t)\hat{\psi}^\dagger_{\sigma'}(\mathbf{r}'t')]|\Psi^0_{GS}\rangle + ... \end{aligned}$$

which requires to evaluate the expectation value of the field operators.

The Wick's theorem provides a method to perform the evaluation of these expectation values. The basic idea underlying this theorem is to move all the annihilation operators coming from the field operators to the right[1], so that, when applied at the independent-particle ground state they will give 0. Similarly the creation operators will be moved to the left. For this reason the normal ordering is introduced as the permutation that permit to have all the annihilation operator on the right. Since in general in the passage from the time ordering to the normal ordering one must take into account the anticommutation rules, we need to define the contraction between two field operators as the difference between the time ordering and the normal ordering: $\overbrace{\psi\psi} = T[\psi\psi] - N[\psi\psi]$. The link between the Wick's theorem and many body perturbation theory is given by the fact that $\overbrace{\psi\psi^\dagger} = iG_0$.

The Wick's theorem [22] states that the time ordering of a serie of field operators is equal to the sum of the normal ordering of the fields operator with increasing number of contracted operator:

$$T[\psi\psi\psi..\psi] = N[\psi\psi\psi..\psi] + \sum_{\sqcap} N[\overbrace{\psi\psi\psi}..\psi] + \sum_{\sqcap\sqcap} N[\overbrace{\psi\psi}\,\overbrace{\psi\psi}..\psi] \quad (2.20)$$

2.3.3 The self-energy and the Dyson's equation

When Wick's theorem is applied to the Green's function the only non zero contribution comes from the terms where all the field operators are contracted, as $\langle N[..]\rangle = 0$.

[1] This is always possible since thanks to a canonical transformation the field operators can be written as sum of a creation and annihilation part.

The Green's function at the first order can, therefore, be written as[2]:

$$\begin{aligned} G(1,2) &= G_0(1,2) + \\ &- i\int d3d4 G_0(1,3)v_C(\mathbf{r}_3-\mathbf{r}_4)G_0(3,2)G_0(4,4) \\ &+ i\int d3d4 G_0(1,3)v_C(\mathbf{r}_3-\mathbf{r}_4)G_0(3,4)G_0(4,2)+... \end{aligned} \tag{2.21}$$

Eq. (2.21) can be summarized as:

$$G(1,2) = G_0(1,2) + \int d3d4 G_0(1,3)\tilde{\Sigma}(3,4)G_0(4,2) \tag{2.22}$$

where $\tilde{\Sigma}(3,4)$ defines the reducible self-energy which is defined by comparing Eq. (2.21) and Eq. (2.22).

Eq. (2.22) can be further simplified by observing that $\tilde{\Sigma}$ can be expressed as a product of a series of simpler functions (the irreducible self-energy Σ) separated by non interacting Green's functions. Thanks to this observation Eq. (2.22) becomes:

$$\begin{aligned} G(1,2) &= G_0(1,2) + \int d3d4 G_0(1,3)\Sigma(3,4)G_0(4,2) + \\ &+ \int d3d4d5d6 G_0(1,3)\Sigma(3,4)G_0(4,5)\Sigma(5,6)G_0(6,2)+... \end{aligned} \tag{2.23}$$

By some manipulation the previous equation becomes:

$$\begin{aligned} G(1,2) &= G_0(1,2) + \int d3d4\, G_0(1,3)\Sigma(3,4)\times \\ &\times \left[G_0(4,2) + \int d5d6\, G_0(4,5)\Sigma(5,6)G_0(6,2)+...\right] \end{aligned} \tag{2.24}$$

$$G(1,2) = G_0(1,2) + \int d3d4\, G_0(1,3)\Sigma(3,4)G(3,4), \tag{2.25}$$

which is the Dyson's equation for the Green's function.

2.4 The equation of motion for the Green's function

Starting from the equation of motion for the field operators it is possible to write a similar equation also for the Green's function [23]:

$$\left[i\frac{\partial}{\partial t_1} - h_0(\mathbf{r}_1)\right] G(1,2) - i\int d3\, v_C(1,3)G_2(1,3^+;2,3^{++}) = \delta(1,2). \tag{2.26}$$

[2]At first order only two addends appear since the remaining simplify with the denominator in Eq. (2.17).

This equation connects the one particle Green's function $G(1,2)$ with the two particle Green's function G_2 defined as $G_2(1,2;3,4) = \langle\Psi_{GS}|T[\psi(1)\psi(2)\psi^\dagger(4)\psi^\dagger(3)]|\Psi_{GS}\rangle$. In the same way it is possible to write an equation of motion for the two-particle Green's function which will involve the three-particle Green's function and so on.

A different approach to introduce the self-energy is based on the Schwinger derivative technique [24]. One introduces a small perturbation $U(\mathbf{r}_1, \mathbf{r}_2, t)$ in the Hamiltonian, which will be vanished at the end of the calculation.

Starting from Eq. (2.16) and by taking the functional derivative of the Green's function with respect to U (which affects the S-matrix only) it is possible to write:

$$i\delta G(1,2) = \frac{\langle\Psi_{GS}|T[\delta S\psi(1)\psi^\dagger(2)]|\Psi_{GS}\rangle}{\langle\Psi_{GS}|T[S]|\Psi_{GS}\rangle} - iG(1,2)\frac{\langle\Psi_{GS}|T[\delta S]|\Psi_{GS}\rangle}{\langle\Psi_{GS}|T[S]|\Psi_{GS}\rangle}. \tag{2.27}$$

Since the variation of S can be written as:

$$T[\delta S] = -iT[S\int_{-\infty}^{\infty} dt \int d^3r_3 d^3r_4 \psi^\dagger(\mathbf{r}_3, t^+)\delta U(\mathbf{r}_3, \mathbf{r}_4, t)\psi(\mathbf{r}_4, t), \tag{2.28}$$

we rewrite Eq. (2.27) as:

$$\begin{aligned} i\delta G(1,2) = -\int_{-\infty}^{\infty} dt \int d^3r_3 d^3r_4 \delta U(\mathbf{r}_3, \mathbf{r}_4, t) \quad [\ & G_2(1, \mathbf{r}_4 t; 2, \mathbf{r}_3 t^+) + \\ & - G(1,2)G(\mathbf{r}_4 t, \mathbf{r}_3 t^+)]. \end{aligned} \tag{2.29}$$

Since the previous equation can be extended to the case $t_3 \neq t^+$ the result is:

$$\frac{\delta G(1,2)}{\delta U(3,4)} = -G_2(1,4;2,3) + G(1,2)G(4,3). \tag{2.30}$$

Applying the previous result to the special case of a local potential $U(3,4) = U(3)\delta(3,4)$ the equation of motion (2.26) can be rewritten as:

$$\begin{aligned} \left[i\frac{\partial}{\partial t_1} - h_0(\mathbf{r}_1)\right] G(1,2) \quad &- \quad i\int d3 v_C(1,3)G(3,3^+)G(1,2) + \\ &- \quad i\int d3 v_C(1^+,3)\frac{\delta G(1,2)}{\delta U(3)} = \delta(1,2), \end{aligned} \tag{2.31}$$

or equivalently:

$$\begin{aligned} \left[i\frac{\partial}{\partial t_1} - h_0(\mathbf{r}_1) + i\int d3 v_C(1,3)G(3,3^+)\right] G(1,2) + \\ -i\int d5 \left[\int d3 d4 v(1^+,3)\frac{\delta G(1,4)}{\delta U(3)}G^{-1}(4,5)\right] G(5,2) = \delta(1,2). \end{aligned} \tag{2.32}$$

In Eq. (2.32) it is possible to recognize the Hartree potential $V_H(1) = -i\int d3 v_C(1,3)$ $G(3,3^+)$ and to define the self-energy as:

$$\begin{aligned} \Sigma(1,2) \quad &= \quad i\int d3 d4 v(1^+,3)\frac{\delta G(1,4)}{\delta U(3)}G^{-1}(4,2) = \\ &= \quad -i\int d3 d4 v(1^+,3)G(1,4)\frac{\delta G^{-1}(4,2)}{\delta U(3)}. \end{aligned} \tag{2.33}$$

Thanks to these definitions Eq. (2.32) becomes:

$$\left[i\frac{\partial}{\partial t_1} - h_0(\mathbf{r}_1) - V_H(\mathbf{r}_1)\right] G(1,2) - i\int d3\Sigma(1,3)G(3,2) = \delta(1,2). \tag{2.34}$$

The self-energy defined in Eq. (2.33) is the same quantity appearing in Eq. (2.25), rewritten in term of a new function $\delta G^{-1}/\delta U$.

2.5 The quasiparticle approximation

In an interacting systems the concept of single-particle states can be recovered by using the quasiparticle concept. Quasiparticles can be interpreted as single electrons surrounded by a screening cloud created by the polarization of the electronic substrate. Quasiparticles can interact with each other through the screened Coulomb interaction instead of the bare one. Since these states are just approximations of the real eigenvalues of the problem, their energy will be complex, thus implying a finite lifetime proportional to the inverse of the imaginary part of the self-energy. The aim of the present section is to formally introduce this concept.

2.5.1 The spectral representation of the Green's function

We start by defining the spectral function as

$$A(\mathbf{r}_1, \mathbf{r}_2, \omega) = \frac{1}{\pi}\text{sign}(\mu - \omega)\Im G(\mathbf{r}_1, \mathbf{r}_2, \omega) = \sum_j f_j(\mathbf{r}_1) f_j^*(\mathbf{r}_2)\delta(\omega - \epsilon_j), \tag{2.35}$$

where f_j are the Lehmann amplitudes defined in Eq. (2.9), μ is the chemical potential, and ϵ_j the single particle energies. The $A(\mathbf{r}_1, \mathbf{r}_2, \omega)$ function is real and contains all the informations included in the Green's function. Indeed by its knowledge it is possible to determine the full Green's function thanks to the relation:

$$G(\mathbf{r}_1, \mathbf{r}_2, \omega) = \int_{-\infty}^{\mu} d\omega' \frac{A(\mathbf{r}_1, \mathbf{r}_2, \omega)}{\omega - \omega' - i\eta} + \int_{\mu}^{\infty} d\omega' \frac{A(\mathbf{r}_1, \mathbf{r}_2, \omega)}{\omega - \omega' + i\eta} \tag{2.36}$$

In addition several observables can be calculated in terms of A, which satisfies the following sum-rule:

$$\int_{-\infty}^{\infty} d\omega\, A(\mathbf{r}_1, \mathbf{r}_2, \omega) = \delta(\mathbf{r}_1 - \mathbf{r}_2). \tag{2.37}$$

The spectral function can also be used to calculate the ground state density:

$$\int_0^{\mu} d\omega A(\mathbf{r}_1, \mathbf{r}_1, \omega) = n(\mathbf{r}_1). \tag{2.38}$$

In the case of non-interacting electrons the spectral function simplifies to $A(\mathbf{r}_1, \mathbf{r}_2, \omega) = \sum_j \phi_j(\mathbf{r}_1)\phi_j^*(\mathbf{r}_2)\delta(\omega - \epsilon_j)$ and $\langle j|A(\mathbf{r}_1, \mathbf{r}_2, \omega)|j'\rangle = \delta_{j,j'}\delta(\omega - \epsilon_j)$.

In the interacting case, assuming that both G and Σ are diagonal operators when projected in the basis of the single particle states we have that:

$$\begin{aligned}
\langle j|A(\mathbf{r}_1, \mathbf{r}_2, \omega)|j\rangle = A_{jj}(\omega) &= \frac{1}{\pi}\Im\left\{\frac{1}{(\omega - \epsilon_j) - \Sigma_{jj}(\omega)}\right\} = \\
&= \frac{1}{\pi}\frac{|\Im\Sigma_{jj}(\omega)|}{|\omega - \epsilon_j - \Re\Sigma_{jj}(\omega)|^2 + |\Im\Sigma_{jj}(\omega)|^2} \approx \qquad (2.39)\\
&\approx \frac{1}{\pi}\frac{\Im\Sigma_{jj}\Re Z_j + (\omega - \epsilon_j - \Re\Sigma_{jj})\Im Z_j}{|\omega - \epsilon_j - \Re\Sigma_{jj}(\omega)|^2 + |\Im\Sigma_{jj}(\omega)|^2} \qquad (2.40)
\end{aligned}$$

where $Z_j = \frac{1}{1-\partial\Sigma/\partial\omega|_{\omega=E_j}}$

In this case the spectral function present a sharp peak at energy $E_j = \epsilon_j + \Sigma(E_j)$, which can be interpreted as the quasiparticle energy, and width given by $|\Im\Sigma|$ which corresponds to the inverse lifetime of the quasiparticle state. In addition, due to the energy dependence of Σ, the interacting spectral function will not only exhibit the quasiparticle peak, but it can also show one or more additional structures, called satellites, that cannot be interpreted in terms of single-particle excitations. The renormalization factor Z_j estimates the relative weight of the quasiparticle peaks to the satellites, because it represents the area below the quasiparticle peak. This quantity is smaller than 1 (see Eq. (2.37)) and gives an hint of the importance of correlation in the system. If $Z_j \approx 1$ it means that most of the spectral weight is in the quasiparticle peak, while a smaller Z_j indicates that a fraction of the spectral weight moved to the satellites, which makes the quasiparticle approximation less accurate.

2.5.2 The quasiparticle equation

A different way to introduce the quasiparticle concept starts from the equation of motion of the Green's function (2.34). It is possible to replace the Green's function by its Lehmann expansion, Eq. (2.10) [23]. The result is:

$$\begin{aligned}
&\int d^3r_3 \left\{\left[\omega - h_0(\mathbf{r}_1) - V_H(\mathbf{r}_1)\right]\delta(\mathbf{r}_1 - \mathbf{r}_3) - \Sigma(\mathbf{r}_1, \mathbf{r}_3, \omega)\right\} \\
&\qquad \sum_j \frac{f_j(\mathbf{r}_3)f_j^*(\mathbf{r}_2)}{\omega - \epsilon_j + i\eta\,\mathrm{sign}(\epsilon_j - \mu)} = \delta(\mathbf{r}_1 - \mathbf{r}_2) \qquad (2.41)
\end{aligned}$$

By focusing the attention to just one state i, and assuming that Σ has no poles for $\omega = \epsilon_j$, the previous equation can be rewritten as in the limit for $\omega \to \epsilon_j$:

$$\left[h_0(\mathbf{r}_1) + V_H(\mathbf{r}_1)\right] f_j(\mathbf{r}_1) + \int d^3r_3 \Sigma(\mathbf{r}_1, \mathbf{r}_3, \omega) f_j(\mathbf{r}_3) = \omega f_j(\mathbf{r}_1), \qquad (2.42)$$

which provides the quasiparticle equation, i.e. a Schrödinger like equation for the Lehmann amplitudes, where the self-energy plays the role of a complex, non-local,

dynamical and non-Hermitian potential. This implies that the corresponding eigenvalues are complex, implying a finite lifetime of the quasiparticles.

2.6 Hedin's equations

The perturbative expansion presented in Sec. 2.3 diverges when it is written in term of the bare v_C. In the HEG case already the second order is infinite. A more efficient scheme has been proposed in 1965 by Hedin. Its approach is based on a close set of five equations [25] written in term of the screened Coulomb interaction. This section reviews this approach.

To derive Hedin's equation we consider the external interaction screened by the Hartree term[3]

$$V(1) = U(1) - V_H(1) \tag{2.43}$$

where U corresponds to the interaction introduced in Sec. 2.4 and $V_H(1) = -i \int d2 v_C(1,2)$ $G(2,2^+)$. In this case the self-energy in Eq. (2.33) can be rewritten as:

$$\Sigma(1,2) = -i \int d3d4d5 v_C(1^+,3) \frac{\delta G^{-1}(1,4)}{\delta V(5)} \frac{\delta V(5)}{\delta U(3)} G(4,2) \tag{2.44}$$

By defining the time-ordered inverse dielectric function ϵ^{-1}, the screened interaction W and the irreducible vertex function Γ as

$$\epsilon^{-1}(1,2) = \frac{\delta V(1)}{\delta U(2)} \tag{2.45}$$

$$W(1,2) = \int d3 v_C(1,3) \epsilon^{-1}(3,2) \tag{2.46}$$

$$\Gamma(1,2;3) = -\frac{\delta G^{-1}(1,2)}{\delta V(3)} \tag{2.47}$$

Eq. (2.44) becomes:

$$\Sigma(1,2) = i \int d3d4 G(1,4) W(3,1^+) \Gamma(4,2;3). \tag{2.48}$$

The inverse dielectric function can be rewritten in terms of the polarizability χ by using:

$$\epsilon^{-1}(1,2) = \frac{\delta[U(1) - i \int d3 v(1,3) G(3,3^+)]}{\delta U(2)} = \delta(1,2) + \int d3 v_C(1,3) \chi(3,2) \tag{2.49}$$

[3]In the case one starts from the DFT Green's function one must also take care of the exchange and correlation potential.

where $\chi(1,2) = -i\frac{\delta G(1,1^+)}{\delta U(2)}$ is the reducible polarizability. In the same way it is possible to define the irreducible polarizability by taking the derivative of G with respect to V instead of U:

$$\tilde{\chi}(1,2) = -i\frac{\delta G(1,1^+)}{\delta V(2)}. \tag{2.50}$$

By definition the two quantities are related through the following relation:

$$\chi(1,2) = -i\int d3\frac{\delta G(1,1^+)}{\delta V(3)}\frac{\delta V(3)}{\delta U(2)} = \tilde{\chi}(1,2) + \int d3d4\tilde{\chi}(1,3)v_C(3,4)\chi(4,2). \tag{2.51}$$

In addition by applying to Eq. (2.50) the chain-rule property of the functional derivative it is possible to write:

$$\tilde{\chi}(1,2) = i\int d3d4G(1,3)\frac{\delta G^{-1}(3,4)}{\delta V(2)}G(4,1) = -i\int d3d4G(1,3)G(4,1)\Gamma(3,4;2) \tag{2.52}$$

and as a consequence the screened interaction is:

$$W(1,2) \;=\; v_C(1,2) + \int d3d4v_C(1,3)\tilde{\chi}(3,4)W(4,2). \tag{2.53}$$

By using the Dyson's equation $G^{-1} = G_0^{-1} - V - \Sigma$ the vertex can be expressed as:

$$\begin{aligned}
\Gamma(1,2:3) &= \delta(1,2)\delta(1,3) + \frac{\delta\Sigma(1,2)}{\delta V(3)} = \\
&= \delta(1,2)\delta(1,3) + \int d4d5\frac{\delta\Sigma(1,2)}{\delta G(4,5)}\frac{G(4,5)}{\delta V(3)} = \\
&= \delta(1,2)\delta(1,3) + \int d4d5d6d7\frac{\delta\Sigma(1,2)}{\delta G(4,5)}G(4,6)G(7,5)\Gamma(6,7;3).
\end{aligned} \tag{2.54}$$

In summary, we obtain a formally closed set of five coupled equation (including the Dyson's equation for the Green's function) which constitutes the Hedin's equations [25]:

$$G(1,2) = G_0(1,2) + \int d3d4G_0(1,3)\Sigma(3,4)G(4,2) \tag{2.55}$$

$$W(1,2) = v_C(1,2) + \int d3d4v_C(1,3)\tilde{\chi}(3,4)W(4,2) \tag{2.56}$$

$$\Sigma(1,2) = i\int d3d4G(1,4)W(3,1^+)\Gamma(4,2;3) \tag{2.57}$$

$$\tilde{\chi}(1,2) = -i\int d3d4G(1,3)G(4,1)\Gamma(3,4;2) \tag{2.58}$$

$$\Gamma(1,2;3) = \delta(1,2)\delta(1,3) + \int d4d5d6d7\frac{\delta\Sigma(1,2)}{\delta G(4,5)}G(4,6)G(7,5)\Gamma(6,7;3). \tag{2.59}$$

This set of equations can be in principle solved iteratively: starting from some guess for the Green's function and for the self-energy it is possible to evaluate the vertex from Eq. (2.59). then one can solve Eq. (2.58) for the polarizability, and Eq. (2.56) for the screened interaction. Now one owns all the ingredients to update the self-energy via Eq. (2.57) followed by the Green's function, Eq. (2.55), and start a new cycle until self-consistency is achieved. If one starts from the DFT Green's function the Hedin's equations are modified by the replacement of the self-energy with $\Sigma(1,2) - V_{XC}(1)\delta(1,2)$.

2.6.1 The GW approximation

The main difficulty in the solution of Hedin equations is due to the presence of the vertex function. On the other hand, the choice of using as perturbative potential W insted of v is expected to lead to a faster convergence. This is the reason why for most calculations a standard approximation is to retain just the zeroth order contribution to the vertex $\Gamma(1,2:3) = \delta(1,2)\delta(1,3)$ in order to simplify Hedin's equations:

$$G(1,2) = G_0(1,2) + \int d3d4 G_0(1,3)\Sigma(3,4)G(4,2) \tag{2.60}$$

$$W(1,2) = v_C(1,2) + \int d3d4 v_C(1,3)\tilde{\chi}(3,4)W(4,2) \tag{2.61}$$

$$\Sigma(1,2) = iG(1,2)W(2,1^+) \tag{2.62}$$

$$\tilde{\chi}(1,2) = -iG(1,2)G(2,1). \tag{2.63}$$

This is the so called GW approximation [6, 25] for the self-energy. Although there is no rigorous theoretical justification of the GW approximation, the improvement it usually produces over DFT results layed down the success of this approximation.

2.7 Technical implementation of the GW approximation

To calculate quasiparticle energies with the GW approximation, we should solve the simplified Hedin's equations (2.60-2.63) in a self-consitsent way. This means that from the non interacting Green's function G_0 deduced by a DFT calculation one must, first of all, calculate the polarizability thanks to Eq. (2.63). Its knowledge perimts to solve Eq. (2.61) to obtain the screened interaction. With the already computed Green's function one is allowed to calculate the self energy via Eq. (2.62). Its knowledge permits to update the Green's function, thanks to Eq. (2.60) and iterate this procedure until self-consistency is reached.

An equivalent method is the so called quasiparticle self-consistent GW where one uses the spectral representation of the response functions appearing in Hedin's equations [26, 27]. In this case the calculation starts from the computation of χ_0. This is

used to calculate the GW self-energy, which is then diagonalized. Thanks to the eigenfunctions and eigenvectors obtained in this way it is possible to compute the second step polarization function using its spectral representation. The procedure is iterated until self-consistency is reached.

Nevertheless the computational weight of the fully self-consistent GW remains prohibitive and a simpler approach is preferred. A well established method is, for the reasons just explained, the so called G_0W_0 approximation [3, 28], which avoids self-consistency, by using the first iteration of Hedin's equations. This approach is justified by the fact that the Kohn-Sham equation and the quasiparticle equation are formally similar. Approximate corrections of the Kohn-Sham eigenvalues are, therefore, obtained applying the perturbation theory in $\Sigma - V_{XC}$, where Σ is the one obtained at the first iteration. In practice, the G_0W_0 corrected quasiparticle energies are given by the following equation:

$$E_i \simeq \epsilon_j + \frac{\langle \Sigma(\epsilon_j) \rangle - \langle V_{XC} \rangle}{1 - \langle \frac{\partial \Sigma(\epsilon_j)}{\partial \omega} \big|_{\omega=\epsilon_j} \rangle}, \tag{2.64}$$

where ϵ_j is the Kohn-Sham eigenvalue and each expectation value is taken on the corresponding Kohn-Sham state $|j\rangle$. In Eq. (2.64) the denominator comes from the linearization of the self-energy frequency dependence around the bare energy ϵ_j.

This approximation is currently used since the fully self-consistent GW often leads to a worst treatment of electron correlations in prototypal systems such as the uniform electron gas (bandwidth larger than DFT bandwidth [29]) and solid silicon (where it produces a too large band gap [30]), pointing to a crucial role of the neglected vertex corrections [31]. As the vertex corrections are important in correlated materials, the simple G_0W_0 approach is usually considered well suited to study the effect of weak electron-electron correlations.

To further simplify the nontrivial problem of calculating the self-energy, different solutions are available. The most common are the plasmon-pole approximation, which models the frequency dependence of ϵ^{-1}, and the contour deformation approach.

2.7.1 The plasmon pole approximation

To calculate the ω-convolution between G and W in Eq.(2.62) the inverse dielectric matrix ϵ^{-1} must be calculated on at a fine frequency mesh extending over a significantly wide energy interval. Since this procedure is very cumberstone, a faster approach is often preferred. The idea of the plasmon-pole approximation is to fit the frequency dependence of ϵ^{-1} by a Drude like expression:

$$\epsilon^{-1}_{\mathbf{GG'}}(\mathbf{q}, \omega) = \delta_{\mathbf{GG'}} + \frac{\Omega^2_{\mathbf{GG'}}(\mathbf{q})}{\omega^2 - \tilde{\omega}^2_{\mathbf{GG'}}(\mathbf{q})}. \tag{2.65}$$

The model parameters $\Omega^2_{\mathbf{GG'}}(\mathbf{q})$ and $\tilde{\omega}^2_{\mathbf{GG'}}(\mathbf{q})$ can be computed in different ways. A first possibility [3] is to compute the inverse dielectric matrix only at $\omega = 0$ and to impose

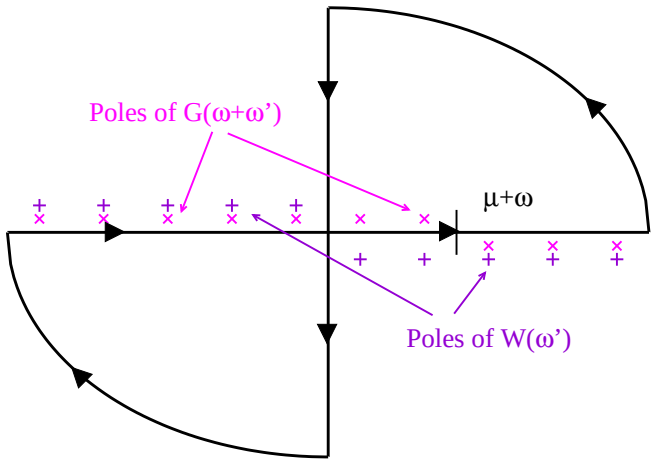

Figure 2.1: Schematic representation of the path used in the contour deformation technique.

the fulfilment of the *f*-sum rule (see appendix C). A completely different approach computes ϵ^{-1} at two frequencies, which are often chosen to be $\omega = 0$ and $\omega = i\omega_P$ (where ω_P corresponds to the plasma frequency of that specific material) and using the expression (2.65) to fit the two numerical values. In this thesis we will use this second approach.

The advantages of this approximation is a simplification of the calculation of the screened interaction, and the possibility of performing analytically all frequency integrations. By separating the contributions to the the self energy coming from the first and the second addend of the plasmon-pole inverse dielectric function, Eq. (2.65), we introduce the exchange and the correlation part of the self-energy:

$$\langle \mathbf{k}j|\Sigma_X|\mathbf{k}j\rangle = -\frac{4\pi}{V_{BZ}}\int_{BZ} d^3q \sum_{j'} f(\epsilon_j(\mathbf{k})) \sum_{\mathbf{G}} \frac{\langle \mathbf{k}-\mathbf{q}, j'|e^{-i(\mathbf{q}+\mathbf{G})\cdot\hat{\mathbf{r}}}|\mathbf{k}, j\rangle\langle \mathbf{k}, j|e^{i(\mathbf{q}+\mathbf{G}')\cdot\hat{\mathbf{r}}}|\mathbf{k}-\mathbf{q}, j\rangle}{|\mathbf{q}+\mathbf{G}|^2} \tag{2.66}$$

$$\langle \mathbf{k}j|\Sigma_C|\mathbf{k}j\rangle = \frac{1}{2\pi V_{BZ}}\int_{BZ} d^3q \sum_{j'}\sum_{\mathbf{G},\mathbf{G}'} -\frac{4\pi\langle \mathbf{k}-\mathbf{q}, j'|e^{-i(\mathbf{q}+\mathbf{G})\cdot\hat{\mathbf{r}}}|\mathbf{k}, j\rangle\langle \mathbf{k}, j|e^{i(\mathbf{q}+\mathbf{G}')\cdot\hat{\mathbf{r}}}|\mathbf{k}-\mathbf{q}, j\rangle}{|\mathbf{q}+\mathbf{G}'|^2} \frac{2\pi\Omega^2_{\mathbf{G}\mathbf{G}'}(\mathbf{q})}{2\tilde{\omega}^2_{\mathbf{G}\mathbf{G}'}(\mathbf{q})} \left[\frac{f(\epsilon_j(\mathbf{k}))}{\omega+\tilde{\omega}^2_{\mathbf{G}\mathbf{G}'}(\mathbf{q})-\epsilon_j(\mathbf{k})-i\eta} + \frac{1-f(\epsilon_j(\mathbf{k}))}{\omega-\tilde{\omega}^2_{\mathbf{G}\mathbf{G}'}(\mathbf{q})-\epsilon_j(\mathbf{k})+i\eta}\right]. \tag{2.67}$$

2.7.2 The contour deformation technique

The main problem in dealing with a numerical integration along the real ω axis is the presence of poles of both the Green's function and the screened interaction W. To overcome this difficulty the integration can be moved on the much smoother imaginary axis by calculating the integral on a complex contour to which the real axis belongs. The contour chosen, represented in Fig. 2.1, is composed by the real and the

imaginary axes closed by two semicircles in the top-right and bottom left quadrants. This trick permits to write the original integral over the real axis, thanks to the Cauchy theorem, as an integration over the imaginary axis plus a summation of poles, since the integration vanishes on the arcs:

$$\Sigma_C(\mathbf{r},\mathbf{r}',\omega) = \frac{i}{2\pi}\left[2\pi i \sum_{z_p,\text{poles of G or W in the contour}} \lim_{z\to z_p} G(\mathbf{r},\mathbf{r}',\omega+z)W(\mathbf{r},\mathbf{r}',z)(z-z_p) + \right.$$
$$\left. - \int_{-\infty}^{\infty} d(i\omega')G(\mathbf{r},\mathbf{r}',\omega+i\omega')W_p(\mathbf{r},\mathbf{r}',i\omega')\right]. \quad (2.68)$$

where $W_p(\mathbf{r},\mathbf{r}',\omega) = W(\mathbf{r},\mathbf{r}',\omega) - v_C(\mathbf{r},\mathbf{r}')$ is the screened interaction minus the bare one. The exchange part of the self-energy is calculated by Eq. (2.66) with this method, too.

The contribution due to the poles can be further simplified since the screened interaction has no poles inside the integration region and only part of the poles of the Green's function fall inside it. In particular in the case that we are interested to a frequency smaller than the chemical potential $\omega < \mu$ the poles due to the occupied state in the Green's function will fall in the upper-right part of the contour. The resulting pole contribution to Σ_C is:

$$\sum_{\text{poles in the upper-right region}} ... = \sum_j \phi_j(\mathbf{r})\phi_j^*(\mathbf{r}')\theta(\mu-\epsilon_j)\theta(\epsilon_j-\omega)W_p(\mathbf{r},\mathbf{r}',\epsilon_j-\omega+i\eta). \quad (2.69)$$

In the same way, in the case $\omega > \mu$ the contribution will be from the empty-states poles in the Green's function falling in the lower-left part giving:

$$\sum_{\text{poles in the lower-left region}} ... = \sum_j \phi_j(\mathbf{r})\phi_j^*(\mathbf{r}')\theta(\epsilon_j-\mu)\theta(\omega-\epsilon_j)W_p(\mathbf{r},\mathbf{r}',\epsilon_j-\omega-i\eta). \quad (2.70)$$

Since W is even in the frequency and odd in the broadening η, the total contribution can be summarized as:

$$\sum_{z_p,\text{poles of G or W in the contour}} ... = \sum_j \phi_j(\mathbf{r})\phi_j^*(\mathbf{r}')\left[-\theta(\mu-\epsilon_j)\theta(\epsilon_j-\omega)+\theta(\epsilon_j-\mu)\theta(\omega-\epsilon_j)\right]$$
$$W_p(\mathbf{r},\mathbf{r}',|\epsilon_j-\omega|-i\eta) \quad (2.71)$$

In a similar way the symmetry $W_p(\mathbf{r},\mathbf{r}',i\omega) = W_p(\mathbf{r},\mathbf{r}',-i\omega)$ implies:

$$\begin{aligned}\int_{-\infty}^{\infty} d(i\omega')... &= i\phi_j(\mathbf{r})\phi_j^*(\mathbf{r}')\int_{-\infty}^{\infty} d\omega' \frac{\omega-\epsilon_j-i\omega'}{(\omega-\epsilon_i)^2+\omega'^2} W_p(\mathbf{r},\mathbf{r}',i\omega') = \\ &= 2i\phi_j(\mathbf{r})\phi_j^*(\mathbf{r}')\int_0^{\infty} d\omega' \frac{\omega-\epsilon_j}{(\omega-\epsilon_j)^2+\omega'^2}\Re W_p(\mathbf{r},\mathbf{r}',i\omega') \quad (2.72)\end{aligned}$$

Accordingly the expression used in practice for the calculations is:

$$\begin{aligned}\Sigma_C(\mathbf{r},\mathbf{r}',\omega) &= \frac{1}{\pi}\sum_j \phi_j(\mathbf{r})\phi_j^*(\mathbf{r}')\int_0^\infty d\omega' \frac{\omega-\epsilon_j}{(\omega-\epsilon_j)^2+\omega'^2}\Re W_p(\mathbf{r},\mathbf{r}',i\omega') + \\ &+ \sum_j \phi_j(\mathbf{r})\phi_j^*(\mathbf{r}')\left[-\theta(\mu-\epsilon_j)\theta(\epsilon_j-\omega)+\theta(\epsilon_j-\mu)\theta(\omega-\epsilon_j)\right] \\ &\quad W_p(\mathbf{r},\mathbf{r}',|\epsilon_j-\omega|-i\eta). \end{aligned} \tag{2.73}$$

This method allows to perform more accurate calculations than the ones obtained by using the plasmon-pole approximation. Moreover, the contour deformation technique is more efficient than a direct evaluation of the ω-convolution. This is due to the fact that the integrands are smooth on the imaginary axis and only few frequencies are needed to converge the integral. On the other hand, also the contribution coming from the poles close to the real axis simplifies since the screened interaction is evaluated only for a relatively small number of frequencies.

Chapter 3

The TDDFT

A more recent approach to the many body problem is the time dependent density functional theory [32, 33] (TDDFT). This theory can be viewed as an extension of the Hohenberg-Kohn-Sham DFT to a time-dependent phenomena. As a consequence TDDFT can go beyond the standard DFT by accessing excited states.

3.1 The Runge Gross theorem and the time dependent Kohn-Sham scheme

TDDFT is based on the Runge-Gross (RG) theorem [34] that proves the existence of a biunivocal correspondence between the time-dependent density of the system $n(\mathbf{r},t)$ and the external potential $V_{ext}(\mathbf{r},t)$ under two mild assumptions. The first is the assumed knowledge of the initial state $\Psi(\mathbf{r},t=t_0)$. This condition is automatically fulfilled when the system evolves starting from its ground state computed accordingly to the ordinary Hohenberg-Kohn theorem. On the other hand the RG theorem takes into account also the case when the system evolves starting from an arbitrary excited state. However in this case the knowledge of the status of the system at $t=t_0$ becomes necessary. The second assumption of this theorem is that the external time dependent potential must be Taylor expandable around $t=t_0$. This condition is in general fulfilled by any well behaving potential appearing in physical problems.

When the Runge-Gross theorem applies it is possible to extend the Kohn-Sham set of equation (1.12) in the time-dependent case:

$$\begin{aligned} i\frac{\partial}{\partial t}\phi_i(\mathbf{r},t) &= H_{KS}(\mathbf{r},t)\phi_i(\mathbf{r},t) = \\ &= \left[-\frac{\nabla^2}{2} + V_{ext}(\mathbf{r},t) + V_H(\mathbf{r},t) + V_{XC}(\mathbf{r},t)\right]\phi_i(\mathbf{r},t) \end{aligned} \tag{3.1}$$

where the time dependence in the Hartree and exchange-correlation potentials comes through the density. In this scheme the single particle wavefunctions have the only property of generating the correct density $n(\mathbf{r},t)=\sum_i |\phi_i(\mathbf{r},t)|^2$.

While for the static DFT a variational principle permits to deduce the Kohn-Sham equations by the minimization of the total energy, in TDDFT the energy functional is replaced by the quantum mechanical action $\mathcal{A}$, which describes the time evolution of the interacting systems from t_1 to t_2[1]. The stationary condition of $\mathcal{A}$ yields the time dependent Schrödinger equation:

$$\mathcal{A}[\Phi] = \int_{t_1}^{t_2} dt \langle \Phi(t) | i\frac{\partial}{\partial t} - \hat{H}(t) | \Phi(t) \rangle. \tag{3.2}$$

3.2 The linear response regime

Within the linear response regime it is possible to study the response of the system to a small time-dependent perturbation [36]:

$$\hat{H} = \hat{H}_0 + F(t)\hat{O} \tag{3.3}$$

where $\hat{H}_0$ is the unperturbed Hamiltonian and $F(t)\hat{O}$ is the weak perturbation switched on at $t = t_0$.

We are interested in calculating the average of a generic operator $\hat{A}$ after the perturbation is switched on. By considering all the operators in their interaction representation and using the Dyson's expansion of the time evolution operator (2.12) it is possible to write the following expansion for the average of $\hat{A}$ at a generic time t [36]:

$$\langle A(t) \rangle = \langle A(t_0) \rangle_0 - i \int_{t_0}^{t} dt' \langle [\hat{A}(t), \hat{O}(t')] \rangle_0 F(t') + \dots, \tag{3.4}$$

where the notation $\langle ... \rangle_0$ means that the average is computed on a state of the unperturbed Hamiltonian. Equation (3.4) permits to define the response function:

$$\chi_{AO}(t, t') = -i\theta(t - t') \langle [\hat{A}(t), \hat{O}(t')] \rangle_0. \tag{3.5}$$

Equivalently, the time invariance of the unperturbed Hamiltonian permits to shift the time variables $\tau = t - t'$ so that the response function becomes:

$$\chi_{AO}(\tau) = -i\theta(\tau) \langle [\hat{A}(\tau), \hat{O}] \rangle_0. \tag{3.6}$$

Using this definition, the change in the average value of A with and without the perturbation can be written at first order as:

$$\Delta A = \langle A(t) \rangle - \langle A(t_0) \rangle = \int_0^{\infty} d\tau \chi_{AO}(\tau) F(t - \tau). \tag{3.7}$$

A particular case involves periodic perturbations. In these cases it can be useful to write the previous result in reciprocal space. The evaluation of the Fourier transform

[1] This kind of expression for the action $\mathcal{A}$ does not respect the causality requirement, since it is symmetric with respect to the two time arguments. This problem is circumvented by the Kledysh contour technique [35].

presents problems similar to the one encountered in the Sec. 2.2 for the evaluation of the Lehmann representation of the Green's function[2]. Since the perturbation does not vanish for $t \to -\infty$ a factor $e^{\eta t}$ is introduced in order to permit the evaluation of Fourier transformations. This trick can be justified only if the results will be independent on η when, in the end of the calculation, $\eta \to 0$. Aftere Fourier transforming Eq. (3.7) becomes:

$$\Delta A(\omega) = \chi_{AO}(\omega) F(\omega) \tag{3.8}$$

where $\chi_{AO}(\omega)$ is the Fourier transformed of $\chi_{AO}(\tau)$:

$$\chi_{AO}(\omega) = -i \lim_{\eta \to 0} \int_0^\infty d\tau \langle [\hat{A}(\tau), \hat{O}] \rangle_0 e^{i(\omega + i\eta)\tau}. \tag{3.9}$$

Expanding the commutator and introducing a identity between the two operators the matrix element in the previous equation can be rewritten as:

$$\langle [\hat{A}(\tau), \hat{O}] \rangle_0 = \sum_{n,m} P_m - P_n \langle \Psi_n | \hat{A} | \Psi_m \rangle \langle \Psi_m | \hat{O} | \Psi_n \rangle e^{-i(E_n - E_m)\tau}. \tag{3.10}$$

where P_m is the average population of the state $|\Psi_m\rangle$ with energy E_m. Performing the Fourier transform, the response function in reciprocal space can be expressed as:

$$\chi_{AO}(\omega) = \sum_{n,m} \frac{P_m - P_n}{\omega - (E_n - E_m) + i\eta} \langle \Psi_n | \hat{A} | \Psi_m \rangle \langle \Psi_m | \hat{O} | \Psi_n \rangle. \tag{3.11}$$

3.2.1 Response to an external field

In this section we consider the response to an external scalar potential coupled to the density through the perturbation $\int d^3r V_{ext}(\mathbf{r}, t) \hat{n}(\mathbf{r})$. Applying the linear response formalism to calculate the average of the electronic density $\hat{n}(\mathbf{r}) = \sum_j \delta(\mathbf{r} - \mathbf{r}_j)$ we obtain:

$$n(\mathbf{r}, t) - n(\mathbf{r}) = \Delta n(\mathbf{r}, t) = \int_0^\infty d\tau \int d^3r' \chi_{n,n}(\mathbf{r}, \mathbf{r}', \tau) V_{ext}(\mathbf{r}', t - \tau) \tag{3.12}$$

where the density-density response function is defined as:

$$\chi_{n,n}(\mathbf{r}, \mathbf{r}', \tau) = -i\theta(\tau) \langle [\hat{n}(\mathbf{r}, \tau), \hat{n}(\mathbf{r}', 0)] \rangle. \tag{3.13}$$

If the external potential is also periodic it can be convenient to Fourier transform this response function to reciprocal space:

$$\chi(\mathbf{q}, \mathbf{q}', \omega) = \frac{1}{V} \int d^3r e^{-i\mathbf{q}\cdot\mathbf{r}} \int d^3r' e^{-i\mathbf{q}'\cdot\mathbf{r}'} \int d\tau e^{i\omega\tau} \chi(\mathbf{r}, \mathbf{r}', \tau). \tag{3.14}$$

[2]The difference is that in this case we deal with retarded correlators while in the many-body perturbation theory with time-ordered ones.

By using the TDDFT it is also possible to define the density response function of the time-dependent Kohn-Sham system, which possesses by construction the exact density. In this case the total field composed by the external potential plus the Kohn-Sham effective potential. This is the sum of the Hartree contribution and of the exchange and correlation one. The non interacting density response function is defined, then, by

$$\begin{aligned}\Delta n(\mathbf{r},t) &= \int_0^\infty d\tau \int d^3r' \chi_0(\mathbf{r},\mathbf{r}',\tau) V_{tot}(\mathbf{r}',t-\tau) = \\ &= \int_0^\infty d\tau \int d^3r' \chi_0(\mathbf{r},\mathbf{r}',\tau)[V_{ext}+V_H+V_{xc}](\mathbf{r}',t-\tau). \end{aligned} \tag{3.15}$$

χ_0 can be written, for the case of a system in its ground state, in terms of the single particle orbitals as:

$$\chi_0(\mathbf{r},\mathbf{r}',\omega) = \sum_{j,j'} \delta_{\sigma_j,\sigma'_j}(f_{j'}-f_j)\frac{\phi_j(\mathbf{r})\phi_j^*(\mathbf{r}')\phi_{j'}(\mathbf{r}')\phi_{j'}^*(\mathbf{r})}{\omega-(\epsilon_j-\epsilon_{j'})+i\eta} \tag{3.16}$$

where f_i are the occupations of the Kohn-Sham orbital. In addition one must consider that in the presence of continuous spectra (like in the case of Bloch wavefunction) the summation is replaced by an integral.

From Eq. (3.12) it follows:

$$\begin{aligned}\chi(\mathbf{r},\mathbf{r}'\omega) &= \frac{\delta n(\mathbf{r},\omega)}{\delta V_{ext}(\mathbf{r}',\omega)} \\ &= \int d^3r_1 \frac{\delta n(\mathbf{r},\omega)}{\delta V_{tot}(\mathbf{r}_1,\omega)}\frac{\delta V_{tot}(\mathbf{r}_1,\omega)}{\delta V_{ext}(\mathbf{r}',\omega)}. \end{aligned} \tag{3.17}$$

It is possible to recognize the definitions of χ_0 given in Eq. (3.15), so that the previous equation can be further manipulated to give:

$$\begin{aligned}\chi(\mathbf{r},\mathbf{r}'\omega) &= \int d^3r_1 \chi_0(\mathbf{r},\mathbf{r}_1,\omega)\left[\delta(\mathbf{r}-\mathbf{r}_1)+\frac{\delta V_H(\mathbf{r}_1,\omega)}{\delta V_{ext}(\mathbf{r}',\omega)}+\frac{\delta V_{xc}(\mathbf{r}_1,\omega)}{\delta V_{ext}(\mathbf{r}',\omega)}\right] = \\ &= \chi_0(\mathbf{r},\mathbf{r}',\omega)+\int d^3r_1 d^3r_2 \chi_0(\mathbf{r},\mathbf{r}_1,\omega)\left[\frac{\delta V_H(\mathbf{r}_1,\omega)}{\delta n(\mathbf{r}_2,\omega)}+\frac{\delta V_{xc}(\mathbf{r}_1,\omega)}{\delta n(\mathbf{r}_2,\omega)}\right]\chi(\mathbf{r}_2,\mathbf{r}'\omega). \end{aligned} \tag{3.18}$$

Since the functional derivative of the Hartree potential is v_C and defining as exchange and correlation kernel $f_{XC} = \delta V_{xc}/\delta n$ it is possible to write a Dyson-like equation, connecting the interacting response functions with the non-interacting one:

$$\begin{aligned}\chi(\mathbf{r},\mathbf{r}'\omega) &= \chi_0(\mathbf{r},\mathbf{r}'\omega)+ \\ &+ \int d^3r_1 d^3r_2 \chi_0(\mathbf{r},\mathbf{r}_1\omega)\left[v_C(\mathbf{r}_1-\mathbf{r}_2)+f_{XC}(\mathbf{r}_1,\mathbf{r}_2,\omega)\right]\chi(\mathbf{r},\mathbf{r}'\omega). \end{aligned} \tag{3.19}$$

While everything else in this equation is straightforward, the exchange-correlation kernel $f_{XC}(\mathbf{r}_1,\mathbf{r}_2,\omega)$ is far from trivial, and only approximations of it are available.

3.2.2 The exchange and correlation kernel

The less trivial ingredient of the TDDFT linear response approach is the exchange and correlation kernel, which must be approximated. Several functionals have been proposed in literature, while only few are commonly used.

The simplest approximation (the random phase approximation or RPA) consists in neglecting f_{XC}:

$$f_{XC}(\mathbf{r}_1, \mathbf{r}_2, \omega) = 0. \tag{3.20}$$

There exists also an extension of the static LDA to the time-dependent problem, known as TDLDA [37]. In this case f_{XC} is assumed to be a functional local in space and in time:

$$f_{XC}(\mathbf{r}_1, \mathbf{r}_2, \omega) = \delta(\mathbf{r}_1 - \mathbf{r}_2) f_{XC}^{HEG}[n(\mathbf{r}_1, \omega)] \tag{3.21}$$

where f_{XC}^{HEG} is the kernel for the homogeneous electron gas evaluated at the corresponding time-dependent density. Nevertheless the commonly used the f_{XC} in the TDLDA corresponds to Eq. (3.21) with $n(\mathbf{r}_1, \omega) \approx n(\mathbf{r}_1, \omega = 0)$.

Other more complex kernels arising from the many-body perturbation theory will be discussed later in Sec. 4.2.

3.3 Dielectric properties of a solid

In general the description of the response of a solid to an external electromagnetic field for anisotropic systems [38] requires the introduction of the dielectric tensor, the current-density and current-current correlation functions. The full description of this problem is beyond the aim of this thesis. In this section we will consider only the special case of the response to a longitudinal field. This case can be described using a scalar potential and the density-density response function previously introduced.

3.3.1 Response to a longitudinal field

When a system of electrons is perturbed by a scalar potential $V_{ext}(\mathbf{r}, \omega)$ the potential screened by the electrons in the system can be written as the sum of the external potential plus the one induced by the modification of the density,

$$V_{tot}(\mathbf{r}, \omega) = V_{ext}(\mathbf{r}, \omega) + V_{ind}(\mathbf{r}, \omega) = V_{ext}(\mathbf{r}, \omega) + \int d^3r' \frac{\Delta n(\mathbf{r}', \omega)}{|\mathbf{r} - \mathbf{r}'|}. \tag{3.22}$$

By using Eq. (3.12) the previous equation can be written as

$$V_{tot}(\mathbf{r}, \omega) = \int d^3r' \epsilon^{-1}(\mathbf{r}, \mathbf{r}', \omega) V_{ext}(\mathbf{r}', \omega), \tag{3.23}$$

which defines the inverse dielectric function:

$$\epsilon^{-1}(\mathbf{r},\mathbf{r}',\omega) = \delta(\mathbf{r}-\mathbf{r}') + \int d^3r_1 \frac{1}{|\mathbf{r}-\mathbf{r}_1|}\chi(\mathbf{r}_1,\mathbf{r}',\omega). \tag{3.24}$$

In the case of a periodic system it is convenient to rewrite the above equations in reciprocal space, taking advantage of the properties discussed in Appendix A. In this case Eq. (3.12) becomes:

$$\Delta n(\mathbf{q}+\mathbf{G},\omega) = \sum_{\mathbf{G}'} \chi(\mathbf{q}+\mathbf{G},\mathbf{q}+\mathbf{G}',\omega) V_{ext}(\mathbf{q}+\mathbf{G}',\omega), \tag{3.25}$$

or using a matricial notation:

$$\Delta n_{\mathbf{G}}(\mathbf{q},\omega) = \sum_{\mathbf{G}'} \chi_{\mathbf{G},\mathbf{G}'}(\mathbf{q},\omega) V_{ext\,\mathbf{G}'}(\mathbf{q},\omega). \tag{3.26}$$

Similarly Eq. (3.23) becomes:

$$V_{tot,\mathbf{G}}(\mathbf{q},\omega) = \sum_{\mathbf{G}'} \epsilon^{-1}_{\mathbf{G},\mathbf{G}'}(\mathbf{q},\omega) V_{ext,\mathbf{G}'}(\mathbf{q},\omega) \tag{3.27}$$

where the inverse dielectric function is:

$$[\epsilon^{-1}]_{\mathbf{G},\mathbf{G}'}(\mathbf{q},\omega) = \delta_{\mathbf{G},\mathbf{G}'} + v_{C\mathbf{G}}(\mathbf{q})\chi_{\mathbf{G},\mathbf{G}'}(\mathbf{q},\omega) \tag{3.28}$$

where $v_{C\mathbf{G}}(\mathbf{q}) = \frac{4\pi}{|\mathbf{q}+\mathbf{G}|^2}$ is the Fourier transformed of the coulomb potential $v_C(\mathbf{r},\mathbf{r}') = \frac{1}{|\mathbf{r}-\mathbf{r}'|}$. In the RPA presented in Sec. 3.2.2 the dielectric function is approximated as:

$$\epsilon_{\mathbf{G},\mathbf{G}'}(\mathbf{q},\omega) = \delta_{\mathbf{G},\mathbf{G}'} - v_{C\mathbf{G}}(\mathbf{q})\chi_{0\,\mathbf{G},\mathbf{G}'}(\mathbf{q},\omega) \tag{3.29}$$

3.3.2 The Macroscopic average and the local fields

By using different experimental techniques it is possible to measure the dielectric properties of a solid. For example, optical absorption permits to determine the imaginary part of the refractive index (the square root of ϵ for null momentum transfer). Reflectivity measurements are also related to the refraction index. On the other hand it is also possible to measure the finite-momentum dielectric function by means of the electron energy loss spectroscopy, which measures the loss function $-\Im\frac{1}{\epsilon}$, or by inelastic X-ray scattering spectroscopy (see Appendix B).

The external fields used in optical experiments have usually a wavelength larger than the typical lattice spacing. Nevertheless the induced perturbations can acquire rapidly oscillating components. As a consequence a macroscopic description of dielectric properties requires an average over the periodic unit cell [39, 40]. In reciprocal space this average procedure is equivalent to consider the $\mathbf{G}=\mathbf{G}'=\mathbf{0}$ component of the dielectric matrix, so that the macroscopic dielectric function will be defined as:

$$\epsilon_M(\mathbf{q},\omega) = \frac{1}{\left[\epsilon^{-1}_{\mathbf{G},\mathbf{G}'}(\mathbf{q},\omega)\right]_{0,0}}. \tag{3.30}$$

Particular care must be taken in evaluating Eq. (3.30), as it involve matrices in the **G** indices. This means that one must first perform the inversion of the full dielectric matrix, and then to consider its $0,0$ element. This procedure is not equivalent to take only the $0,0$ element of the ϵ matrix, which constitutes an approximation that neglects the "local fields". These local fields are microscopic fields arising from the anisotropies of the charge density.

3.4 Numerical calculation of the dielectric matrix

The state-of-the-art approach to calculate the dielectric response of a periodic solid involves, as initial step, the solution of the Kohn-Sham equations, and the evaluation of the independent-particle polarizability χ_0 by Eq. (3.16) Fourier transformed into the momentum space [41]:

$$\begin{aligned}\chi_{0\,\mathbf{G},\mathbf{G}'}(\mathbf{q},i\omega) &= -\frac{1}{V_{BZ}}\sum_{j,j'}\int_{BZ} d^3k\delta_{\sigma_j,\sigma_{j'}}\frac{f(\epsilon_{j'}(\mathbf{k}+\mathbf{q}))-f(\epsilon_j(\mathbf{k}))}{\omega-[\epsilon_{j'}(\mathbf{k}+\mathbf{q})-\epsilon_j(\mathbf{k})]+i\eta}\cdot \\ &\cdot \quad \langle \mathbf{k},j|e^{-i(\mathbf{q}+\mathbf{G})\cdot\hat{\mathbf{r}}}|\mathbf{k}+\mathbf{q},j'\rangle\langle\mathbf{k}+\mathbf{q},j'|e^{i(\mathbf{q}+\mathbf{G}')\cdot\hat{\mathbf{r}}}|\mathbf{k},j\rangle. \qquad (3.31)\end{aligned}$$

where the kets $|\mathbf{k},j\rangle$ represent Bloch Kohn-Sham states for the point $\mathbf{k}$ and band j.

Eq. (3.31) requires to perform a double summation over the bands plus an integration on the Brillouin zone, which can be numerically heavy. To mitigate the numerical difficulties, different algorithms have been devised to speed up the calculations [42].

3.4.1 The $\mathbf{q}\to\mathbf{0}$ limit

To describe optical adsorption one needs to evaluate the $\mathbf{q}\to\mathbf{0}$ limit of the dielectric function. By naively performing the $\mathbf{q}\to\mathbf{0}$ limit of the $\mathbf{G}=\mathbf{G}'=\mathbf{0}$ of Eq. (3.31) we have that

$$\lim_{\mathbf{q}\to\mathbf{0}}\langle \mathbf{k},j|e^{-i(\mathbf{q}+\mathbf{G})\cdot\hat{\mathbf{r}}}|\mathbf{k}+\mathbf{q},j'\rangle = \delta_{j,j'} \qquad (3.32)$$

$$\lim_{\mathbf{q}\to\mathbf{0}} f(\epsilon_j(\mathbf{k}+\mathbf{q}))-f(\epsilon_j(\mathbf{k}))=0. \qquad (3.33)$$

As a consequence the resulting χ_0 would be 0[3]. A more careful analysis of Eq. (3.31) reveals, for example, that for a metal at $\omega=0$ the χ_0 limit is a constant. Anyway in all the remaining cases, a correct evaluation of the asymptotic behaviour is necessary to calculate this limit, because $\chi_0\sim\mathbf{q}^2$ is multiplicated by $v_C\sim\mathbf{q}^{-2}$ to calculate ϵ.

To deal with semiconductors [41] we expand the operatorial part of the matrix elements of Eq. (3.31) in the small-$\mathbf{q}$ limit, which leads to the expression

$$\langle \mathbf{k},j|e^{-i\mathbf{q}\mathbf{r}}|\mathbf{k}+\mathbf{q},j'\rangle \underset{\mathbf{q}\to 0}{\simeq} \delta_{j,j'} - i\mathbf{q}\cdot\langle\mathbf{k},j|\mathbf{r}|\mathbf{k},j'\rangle\,. \qquad (3.34)$$

[3] If $j=j'$ the difference of the occupancies will make the contribution to χ_0 to vanish, while if $j\neq j'$ the same effect is provided by the matrix elements.

The δ function does not contribute in semiconductors. Since the position operator depends on the choice of the origin and it is ill-defined in a periodic system, it must be replaced with the momentum operator thanks to the relation

$$\langle \mathbf{k}, j|\mathbf{r}|\mathbf{k}, j'\rangle = \frac{\langle \mathbf{k}, j|[H, \mathbf{r}]|\mathbf{k}, j'\rangle}{\epsilon_j(\mathbf{k}) - \epsilon'_j(\mathbf{k})}\,. \tag{3.35}$$

Finally we obtain:

$$\langle \mathbf{k}, j|e^{-i\mathbf{q}\mathbf{r}}|\mathbf{k}+\mathbf{q}, j'\rangle \underset{\mathbf{q}\to 0}{\simeq} \frac{\mathbf{q}\cdot\langle \mathbf{k}, j| - \nabla + i[V_{NL}, \mathbf{r}]|\mathbf{k}, j'\rangle}{(\epsilon'_j(\mathbf{k}) - \epsilon_j(\mathbf{k}))} \tag{3.36}$$

where V_{NL} is the non local part of the pseudopotential and in general any part of the Hamiltonian, besides the kinetic energy, which does not commute with the position operator. By substituting this expansion into Eq. (3.31), one obtains the $\mathbf{q} \to \mathbf{0}$ limit for the polarizability, which must be evaluated at a small but non zero $\mathbf{q}$.

As already pointed this approach is accurate when applied to semiconductors, but gives rise to substantial difficulties in describing the metals. This is due to the fact that Eq. (3.36) does not include intraband transitions $j = j'$, since the eigenfunctions are evaluated at the same $\mathbf{k}$-point. For metals there is no well established method and only few calculations with the full inclusion of intraband transitions are available [8, 43, 44]. These are generally taken into account by calculating the metal plasma frequency and adding an approximate Drude like contribution to χ_0.

3.4.2 Inclusion of quasiparticle effects

The independent-particle Kohn-Sham response function χ_0 is the natural starting point for a TDDFT calculation and to be rigorous, it should be calculated using DFT eigenstates. Indeed, the kernel is in principle expected to take into account all the many-body physics leading to the combined effects of the quasiparticle shift of the poles and of the particle-hole interaction (excitonic effects). Despite the efforts spent to construct a kernel cable to describe correctly all this physics [45, 46], the standard approximations used in numerical calculations do not take into account some of these effects. To overcome these difficulties several techniques are used to include some of the missing physics.

One of these approaches requires the use a slightly modified equation for χ_0 in order to include already at this stage the quasiparticle corrections or their finite lifetimes. Self-energy corrections can be introduced by replacing the Kohn-Sham dispersion with the *GW* corrected band structure in Eq. (3.31) [4]. In general, even if this inclusion can be in principle always performed, in practice it should be done only when the χ_0 thus obtained is used in the RPA approximation. Indeed in a TDDFT calculation also the kernel contribute to drive the poles from the Kohn-Sham energy toward the correct quasiparticle ones, thus inducing an uncontrolled superposition of the two effects.

A second effect of the inclusion of quasiparticle effects is some accounting of the finite lifetimes through the imaginary part of the self-energy [4, 47]. In this case their

inclusion is done by replacing the imaginary infinitesimum η with the absolute value of the difference of the imaginary parts of the self-energies $|\Im\Sigma(\epsilon_{j'}(\mathbf{k}+\mathbf{q})) - \Im\Sigma(\epsilon_j(\mathbf{k}))|$.

Chapter 4

The dielectric function

As described in the previous chapters, the basic task in a GW or in a TDDFT calculation is the computation of the independent-particle polarizability χ_0. χ_0 is the key ingredient needed to evaluate the frequency-dependent screened interaction and the dielectric function ϵ. For this reason the present chapter aims to summarize the basic properties of χ_0 and of ϵ.

4.1 The Lindhard dielectric function

The simplest system one can use to study χ_0 and ϵ is the HEG model, introduced in Sec. 1.3 where it is possible to perform analytically all integrations [7].

The calculation starts from the RPA expression of the dielectric function Eq. (3.29):

$$\epsilon(q,\omega) = 1 - \frac{4\pi}{q^2}\chi_0 = 1 + \frac{1}{q^2\pi^2}\int d^3k \frac{\theta(k_F - |\mathbf{k}+\mathbf{q}|) - \theta(k_F - |\mathbf{k}|)}{\omega - \left(\frac{(\mathbf{k}+\mathbf{q})^2}{2} - \frac{\mathbf{k}^2}{2}\right) + i\eta}, \tag{4.1}$$

Due to the translational invariance, the dielectric function depends only on the wave vector modulus.

Thanks to the Cauchy principal value theorem it is possible to separate the real and the imaginary part of ϵ, and to performe the integrations. The resulting expression for the real part of the dielectric function ϵ is:

$$\begin{aligned}\Re\,\epsilon(q,\omega) = 1 + \frac{q_{TF}^2}{2q^2}\Bigg\{1 + \frac{1}{2k_Fq^3}\left[k_F^2q^2 - \left(\frac{q^2}{2}+\omega\right)^2\right]\log\left|\frac{q^2/2+qk_F+\omega}{q^2/2-qk_F+\omega}\right| + \\ + \frac{1}{2k_Fq^3}\left[k_F^2q^2 - \left(\frac{q^2}{2}-\omega\right)^2\right]\log\left|\frac{q^2/2+qk_F-\omega}{q^2/2-qk_F-\omega}\right|\Bigg\},\end{aligned} \tag{4.2}$$

where $q_{TF} = 2\sqrt{\frac{k_F}{\pi}}$ is the Thomas-Fermi wavevector. The calculation of $\Im\epsilon(q,\omega)$

involves the following integration:

$$\Im\,\epsilon(q,\omega) = \frac{1}{q^2 2\pi}\int d^3k\theta(k_F-|\mathbf{k}|)\theta(|\mathbf{k}+\mathbf{q}|-k_F)\left[\delta\left(\omega+\frac{\mathbf{k}^2}{2}-\frac{(\mathbf{k}+\mathbf{q})^2}{2}\right)+\right.$$
$$\left.+\,\delta\left(\omega-\frac{\mathbf{k}^2}{2}+\frac{(\mathbf{k}+\mathbf{q})^2}{2}\right)\right]. \quad (4.3)$$

The imaginary part of ϵ is connected with the electron-hole electronic transitions, that to conserve the momentum and the energy, are permitted only in the region delimited by the parabolas $\omega = \frac{q^2}{2} + qk_F$ and $\omega^2 = \frac{q^2}{2} - qk_F$ (see Fig. 4.1). The resulting expression is:
for $q < 2k_F$:

$$\Im\,\epsilon(q,\omega) = \begin{cases} \frac{2\omega}{q^3} & 0 < \omega \leq -\frac{q^2}{2} + qk_F \\ \frac{1}{q^3}\left[k_F^2 - \frac{1}{q^2}\left(\omega - \frac{q^2}{2}\right)^2\right] & -\frac{q^2}{2} + qk_F < \omega \leq \frac{q^2}{2} + qk_F \\ 0 & \omega > \frac{q^2}{2} + qk_F \end{cases} \quad (4.4)$$

for $q \geq 2k_F$:

$$\Im\,\epsilon(q,\omega) = \begin{cases} \frac{1}{q^3}\left[k_F^2 - \frac{1}{q^2}\left(\omega - \frac{q^2}{2}\right)^2\right] & \frac{q^2}{2} - qk_F < \omega \leq \frac{q^2}{2} + qk_F \\ 0 & \omega \leq \frac{q^2}{2} - qk_F \text{ and } \omega > \frac{q^2}{2} + qk_F \end{cases} \quad (4.5)$$

4.1.1 The plasmon

The loss function $-\frac{1}{\epsilon}$ shows a sharp pole with energy ω_P when $\Im\epsilon(q,\omega) = \Re\epsilon(q,\omega) = 0$, see Fig. 4.1[1]. This peak corresponds to a collective oscillation of the electrons that can be classically described as the oscillation of the negatively charged electrons with respect to the positive jellium background [18]. For $q \to 0$, this simple model leads to a collective harmonic oscillation of the charge density at a frequency $\omega_P = 4\pi n$.

The dispersion relation of this excitation can be determined by imposing the condition that the real part of the Lindhard function should vanish. This equation can be solved only numerically, but an explicit expression at the second order in q is available:

$$\Omega_P(q) = \omega_P\left[1 + \frac{9}{10}\left(\frac{q}{q_{TF}}\right)^2 + ...\right]. \quad (4.6)$$

4.2 Beyond the RPA approximation

The random phase approximation discussed in the previous section constitutes the simplest approximation to the response function for the HEG. In the framework of

[1] A small broadening is added to widen the peak.

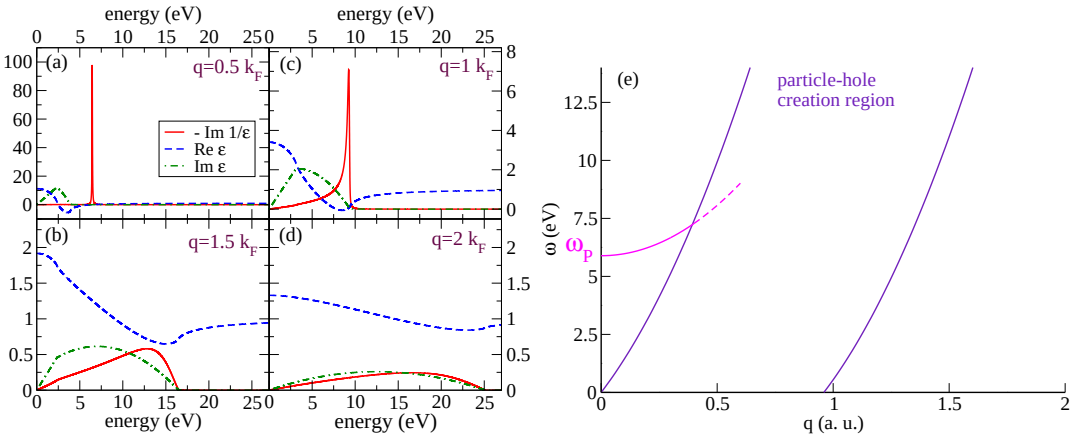

Figure 4.1: Dielectric function and loss function for the HEG $r_S = 4$ for different momenta transfer. Panel (a) $0.5k_F$, (b) $1k_F$, (c) $1.5k_F$ and (d) $2k_F$. Panel (e) region where the single particle excitation are permitted and plasmon dispersion.

many-body perturbation theory this approximation corresponds to build the screened interaction W as a summation of an infinite class of $\chi_0 = -iG_0G_0$ "bubble" terms However, in case of an high electronic density the RPA fails, giving incorrect positive values of the correlation energy per particle [7]. Similarly the RPA is not expected to work correctly in the case of a large momentum longitudinal response function, due to the fact that it does not describe properly parallel spins electronic correlations (they cannot have short range interaction because kept far away by the Pauli principle). Modeover, being ϵ real at the plasmon energy for momenta smaller q_C where the plasmon enters in the particle-hole continuum, the HEG RPA plasmon is not dumped.

To go beyond the RPA in the HEG it is common wisdom to add a *local effective potential* $v_C G(q,\omega)n(q,\omega)$ to the Hartree term, thus modifying the dielectric function as:

$$\epsilon(q,\omega) = 1 - \frac{v_C\chi_0(q,\omega)}{1 + v_C G(q,\omega)\chi_0(q,\omega)} \tag{4.7}$$

where $G(q,\omega)$ is the local field factor. This approach for the jellium model is equivalent to the TDDFT and it can be easily shown that $f_{XC}(q,\omega) = -v_C G(q,\omega)$.

Different local field factors, have been proposed in literature. In the following we will consider the Hubbard and the Corradini expressions.

4.2.1 The Hubbard local field factor

The Hubbard local field factor is the simplest analytic and static expression which satisfies the constrains due to the exchange effects [36][2]. this implies the local effective potential must vanish for small-q since the exchange hole must be well screened for large distances. This implies $G(q) \propto q^2$ for small-q. On the other hand the impossibility for

[2]Two electrons of the same spin cannot come too close each other (exchange hole).

electrons of the same spin to interact at short distance implies the exchange term due to the local field factor to cancel the Hartree term of the effective potential, so that $\lim_{q\to\infty} G(q) = 1$ (in the response function of Eq. (3.31) a δ-function selects transition only between states with parallel spin).

The simplest expression which respect these constrains and scales with k_F defines the Hubbard local field factor:

$$G(q) = \frac{q^2}{q^2 + k_F^2} \tag{4.8}$$

4.2.2 The Corradini local field factor

A slightly more complex local field factor has been proposed by Corradini et al. [48] by performing a simple analytical fit of the QMC results by Moroni et al. [49]. Their local field factor is given by the following parameterization:

$$G(q) = CQ^2 + \frac{BQ^2}{g + Q^2} + \alpha Q^4 e^{-\beta Q^2} \tag{4.9}$$

where $Q = q/k_F$ and the parameters are defined as follow:

$$B = \frac{1 + 2.15\sqrt{r_S} + 0.435 r_S^{3/2}}{3. + 1.57\sqrt{r_S} + 0.409 r_S^{3/2}} \tag{4.10}$$

$$C = -\frac{\pi}{2k_f}\frac{d(r_S\epsilon_C)}{r_S} \tag{4.11}$$

$$g = \frac{B}{A - C} \tag{4.12}$$

$$\alpha = \frac{1.5}{r_S^{1/4}}\frac{A}{Bg} \tag{4.13}$$

$$\beta = \frac{1.2}{Bg} \tag{4.14}$$

$$A = \frac{1}{4} - \frac{k_F^2}{4\pi}\frac{d^2(n\epsilon_C)}{dn^2} \tag{4.15}$$

where ϵ_C is the correlation energy per particle of the HEG.

4.2.3 The plasmon dispersion beyond RPA

To compare the behaviour of the different kernels described in the previous section we consider, as an example, the modification of the plasmon dispersion induced by different kernels. A more complete discussion about how these kernels perform when applied to a solid system can be found in Chapter 6 and 7, while a discussion about other kernels can be found in Ref. [50]

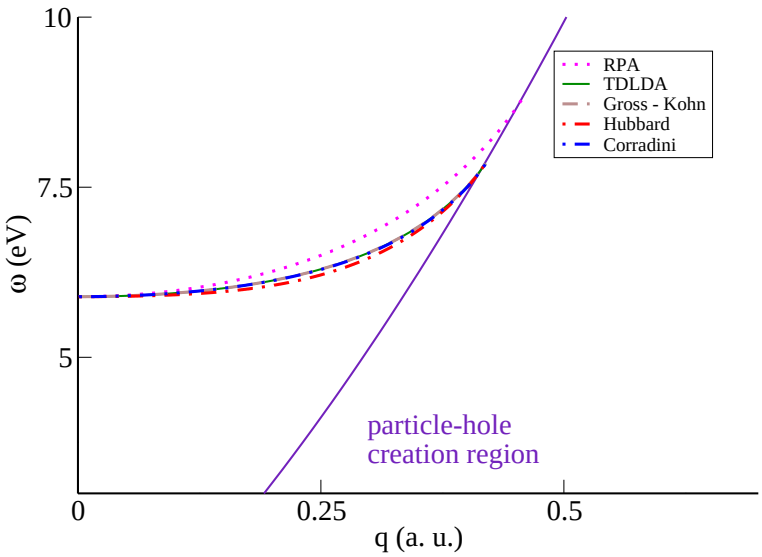

Figure 4.2: Numerically calculated plasmon dispersion for an HEG of $r_S = 4$ with different local field factors.

First of all, similarly to the case of, RPA is possible to calculate a second order expansion of the dispersion law for the plasmon frequency $\Omega_P(q)$:

$$\Omega_P(q) = \omega_P \left[1 + \left(\frac{9}{10 q_{TF}^2} + \frac{f_{XC}(0, \omega_P)}{8\pi} \right) q^2 + ... \right] . \tag{4.16}$$

From this equation it is possible to observe that in the long-wavelength limit, if the kernel does not diverge, the plasmon dispersion converges to the RPA plasma frequency.

When the condition $\epsilon(\mathbf{q}, \omega) = 0$ is solved numerically to obtain the plasmon energy one gets the results shown in Fig. 4.2. As expected all curves tend to the RPA long wavelength limit. All kernels presented here slow down the dispersion with respect to RPA. In particular the TDLDA, the Gross and Kohn kernel, and the Corradini one provide comparable results, while the Hubbard local field factor decreases even more the dispersion.

In addition, in the HEG case, all kernels with the exception of the Gross and Kohn one are real which means that they do not introduce any plasmon damping. Only the Gross and Kohn kernel does it but its effect is very small.

4.3 The dielectric function in presence of a periodic lattice

The simple HEG model allows to treat the electronic correlations at different levels or approximations. Nevertheless it does not include band-structure effects, which modify the dielectric function with respect to the Lindhard expression. For this reason in this section we illustrate, at least qualitatively, the peculiar modifications of the dielectric function induced by the presence of the band structure and of interband transitions, even at the simple RPA level.

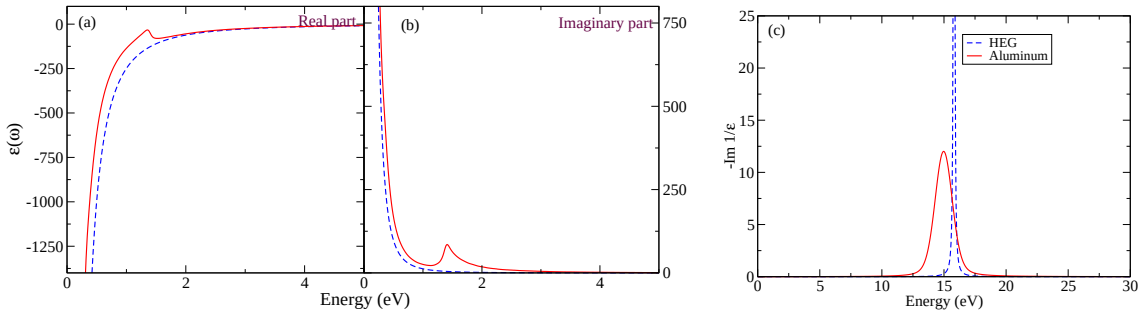

Figure 4.3: Comparison of the long range HEG Lindhard function (dashed, for $r_S = 2.07a_0$ corresponding to the density of Al) with the calculated response for aluminum (solid, for the details of its numerical evaluation see Sec. 7.2). A broadening of 0.05 eV has been added to both the calculations. Notice the main differences introduced in the RPA dielectric function by the presence of interband transition as the 1.5 eV peak in the imaginary part of ϵ with the consequent structure in the real part. The loss function shows the broadening and the shift of the plasmon peak.

The main additional feature is the presence of interband transitions which introduce new poles in the response function. As a consequence new peaks appear in the $\mathbf{q} \to 0$ imaginary part of dielectric function (see Fig. 4.3 b), which substantially differs from the Lindhard function.

Band effects induce modifications also in the plasmon resonance [51, 52]. The interband transitions prevent the imaginary part of the dielectric function to vanish at the plasma frequency. For this reason the plasmon peak becomes a Lorentzian with a finite width also in the case of small wave vectors. This feature is absent in the jellium case where Ω_P falls outside the region where the creation of particle-hole excitation is allowed. In addition the interband contributions modify the real part of ϵ causing also a shift in the plasmon peak position with respect to the HEG one at the same electron density. Band effects originate also a dependence of the plasmon dispersion on the direction of the momentum $\mathbf{q}$ which of course does not appear in the HEG. These effects can be seen in Fig. 4.3 (c) where the loss functions of jellium and of aluminum are compared in the long wavelength limit: notice that the plasmon peak of aluminum appears at smaller energy than in the HEG and it is broad.

4.3.1 The zone boundary collective states

Interband and intraband transitions are not the only differences that the band structure introduces in the density response of a periodic system when compared to the HEG model. In particular in this section we will discuss a new collective excitation clearly visible in the loss function for non vanishing momentum transfer. These collective states, called zone-boundary collective states (ZBCS), are induced by the periodic potential which, as demonstrated by using a nearly free electron model, is responsible for the opening of a gap in the band structure close to the Brillouin zone boundary

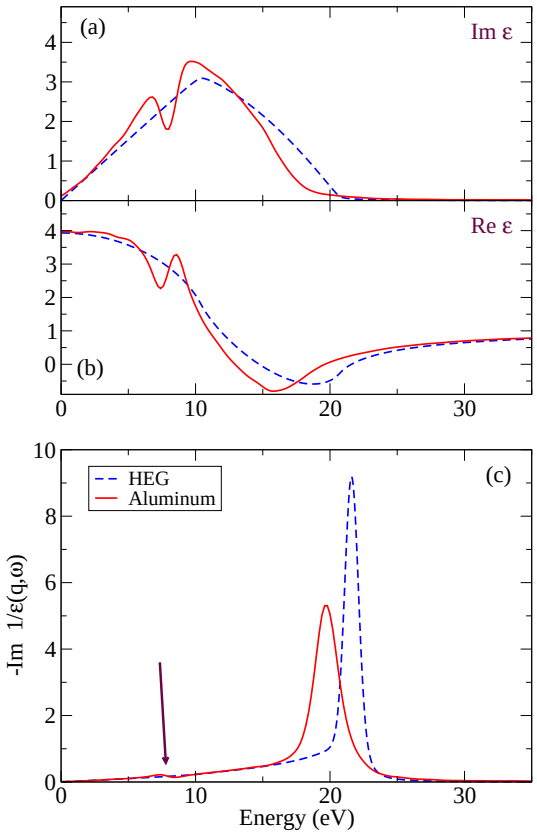

Figure 4.4: Real (a) and imaginary (b) part of ϵ for the HEG and for aluminum, at a momentum q =0.616 a_0^{-1}. It is possible to notice the shift and broadening of the plasmon similar to the long wavelength case and the new collective state seen in the loss function (c) due to the zone-boundary gap (pointed by the arrow).

[18].

To understand, at least qualitatively, the origin of these new collective excitations we consider a system where a perturbative periodic potential modifies the HEG in such a way to open a gap at the zone boundary (for a more quantitative description see [53, 54]). This gap modifies the region where the creation of particle-hole excitations is allowed, and reduces the overall energy concentration of electron-hole pairs. This causes the imaginary part of the dielectric function of the system with periodic lattice to be smaller than the Lindhard function[3] (see Fig. 4.4 a and b). When looking at the loss function (Fig. 4.4 c) this effect induces a weak, low energy, peak, that can be interpreted as a new collective excitation induced by a zone boundary effect.

[3]By consequence also the real part is modified.

Part II

Numerical applications

Chapter 5

Intraband transitions in the G_0W_0 approximation for metals

More than 20 years of successful applications have established Hedin's *GW* approach [6, 25] and its numerical implementations [28, 3] as the state-of-the-art theoretical method and most widely used for *ab-initio* many-body bandstructure calculations. Efficient algorithms have been devised to encompass the major numerical bottlenecks in the *GW* calculations: e.g. by avoiding **k**-space convolutions by a space-time method [55], avoiding summations over empty states in the evaluation of the polarizability [56, 57], and using localized basis functions [58], and/or model screening functions [59, 60, 61]. However, systems with metallic screening present an additional, challenging, difficulty due to the evaluation of the **k**-space integrals appearing in the intraband contribution to the electronic screened interaction. These transitions, occurring at the Fermi surface, can dramatically slow down the convergence with respect to the **k**-space sampling. As a consequence, the possibility to perform such *ab-initio GW* calculations in metallic systems with a large unit cell is hindered. Even worse, when calculations are performed using an unconverged **k**-point sampling, a spurious gap at the Fermi level may appear. The gap vanishes only in the limit of infinitely dense sampling, and is shown to close very slowly as the number of **k**-points increases. Solutions based on explicit Fermi surface integration [44] are effective but result in cumbersome coding and substantial increase of computation time.

In this chapter we present a numerically stable and efficient method, based on a Taylor expansion of the polarizability matrix in the small-**q** region, which includes intraband contributions and avoids explicit Fermi-surface calculations. The method has been implemented successfully into the `abinit` [62, 63] package, and is shown to remove the spurious gap at the Fermi level already with a limited number of **k**-points.

The present chapter follows the discussion published in Ref. [64].

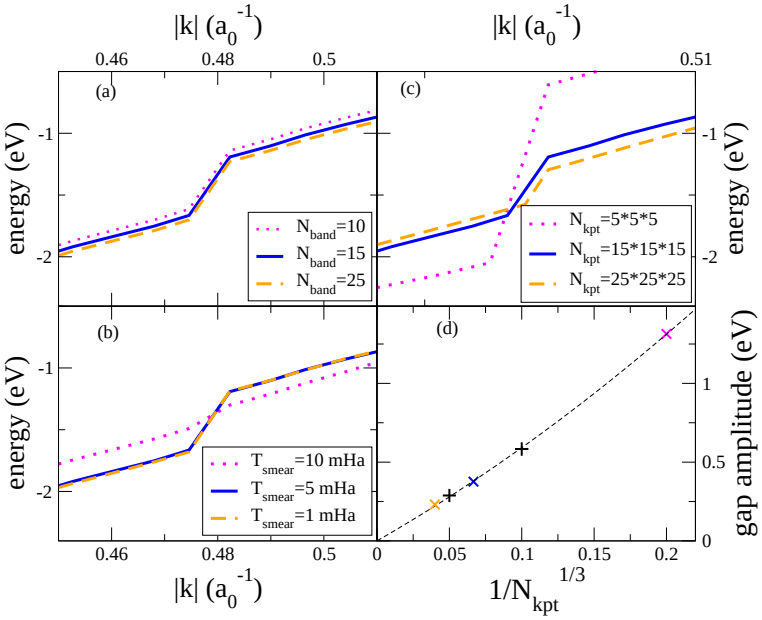

Figure 5.1: Self-energy corrected G_0W_0 band structure of Na (110 direction), showing the appearance of an unphysical gap, and its dependence on different numerical convergence parameters. Panel (a) shows the dependence with respect to the number of empty states in Eq. (3.31); (b) with respect to the smearing temperature; (c) with respect to the **k**-point mesh. Panel (d) shows the dependence of the unphysical gap on the inverse number of **k**-points in each direction; the dashed line is a fitted $a_1 N_{\text{kpt}}^{-1/3} + a_2 N_{\text{kpt}}^{-2/3}$.

5.1 Naive application of a standard G_0W_0 code to metallic systems

When a standard G_0W_0 code for semiconductor or insulator is used to calculate the self-energy correction for metals, the incorrect small-**q** values of χ_0 induce the opening of an unphysical gap at the Fermi energy in the G_0W_0 band dispersion, as shown in Fig. 5.1. The figure shows the convergence properties of the width of this unphysical gap, computed by extrapolation from the two sides of the band dispersion. The spurious gap is essentially independent on most numerical convergence parameters, such as the number of empty states and the smearing temperature, as shown in Fig. 5.1(a,b). The only dependence is on the number N_{kpt} of sample points in the **k**-space mesh: Fig. 5.1(c,d) shows that the unphysical gap does tend to close for increasing mesh size, but only extremely slowly, as $N_{\text{kpt}}^{-\frac{1}{3}}$, as it will be explained later. Therefore, it is practically impossible to close the gap by brute-force mesh refinement, especially because the computation time of the dielectric matrix grows as N_{kpt}^2. A larger smearing temperature for electronic occupancy would reduce this unphysical gap, but it is a mere technical device, and convergence should be checked in the limit of vanishingly small smearing, where the actual metallic state is recovered.

The origin of the unphysical gap is the incorrect $\mathbf{q} = \mathbf{0}$ screening function, due to the missing intraband contribution. At first sight, as χ_0 enters the calculation of Σ through a N_{kpt}-discretized **q**-convolution in reciprocal space, one might think that this single incorrect value should affect the energy corrections $\langle \Sigma - V_{XC} \rangle$, with an error of order N_{kpt}^{-1}. However, the singular behaviour of the Coulomb repulsion v_C near

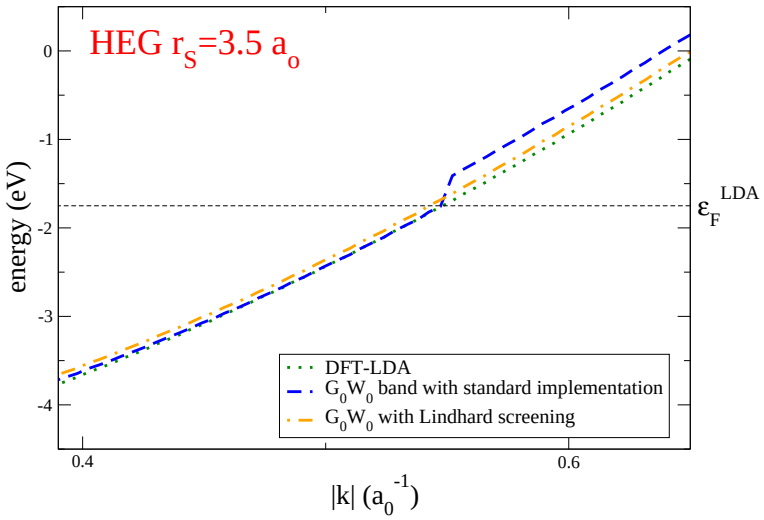

Figure 5.2: Self-energy corrected bandstructure for the HEG ($r_s = 3.5\,a_0$) computed with the standard implementation of the G_0W_0 method and with the Lindhard screening compared to the DFT dispersion. The spurious gap, caused by the lack of the intraband term in the screening, is removed when the computed polarizability is replaced by the Lindhard one (dot-dashed line). The Kohn-Sham band is also displayed for reference (dotted line).

$\mathbf{q} = \mathbf{0}$ requires an explicit integration around the singular point, which makes the final outcome sensitive to the incorrect $\chi_{0\,\mathbf{0},\mathbf{0}}(\mathbf{0}, i\omega)$ with an error of order $N_{\mathrm{kpt}}^{-\frac{1}{3}}$. Fig. 5.2 shows this effect in the HEG, where the gap is shown to disappear when the numerical dielectric matrix is replaced by the Lindhard function described in Sec. 4.1.

In metals, the dielectric function ϵ is expected to diverge when both $\omega \to 0$ and $\mathbf{q} \to \mathbf{0}$ (by contrast, it goes to its finite static limit in semiconductors and insulators). The expression (3.36) vanishes exactly for the HEG and $\mathbf{q} = \mathbf{0}$ since, for free electrons, only intraband transitions can contribute to the sum in Eq. (3.31), and the latter vanish due to the occupancy factors f_i. The resulting incorrect null value of $\chi_0(\mathbf{q} \to \mathbf{0}, i\omega)$ yields $\epsilon^{-1}(\mathbf{q} \to \mathbf{0}, i\omega) = 1$, rather than the correct $\epsilon^{-1}(\mathbf{q} \to \mathbf{0}, i\omega) = \frac{\omega^2}{\omega^2+\omega_P^2}$, as shown in Fig. 5.3 where numerical results are compared with the Lindhard function.

A similar discontinuity in G_0W_0 corrections occurs for real metals such as Na and Al. Differently from the HEG, we find $\epsilon^{-1}(\mathbf{0}, \omega) < 1$, due to the nonzero interband contributions. In particular we obtain $\epsilon^{-1}_{\mathrm{Na}}(\mathbf{q} = \mathbf{0}, 0) \simeq 0.94$, similar to the incorrect HEG value, and $\epsilon^{-1}_{\mathrm{Al}}(\mathbf{q} = \mathbf{0}, 0) \simeq 0.008$. The latter nears the proper Drude value, due to a substantial part of the aluminum Fermi surface being very close to a Brillouin-zone boundary. The so originated interband transitions makes ϵ to be large for small frequencies. Thus the error induced by neglecting the intraband term is so small that the unphysical gap is almost invisible.

5.2 Extrapolated small-q polarizability

The solution we propose avoids the explicit integration over the Fermi surface that is required in a straightforward inclusion of the intraband term. We prefer to compute the small $\mathbf{q}$ polarizability by a fit of the expected asymptotic behaviour of χ_0. The time-reversal invariance implies the polarizability matrix to respect the following symmetry

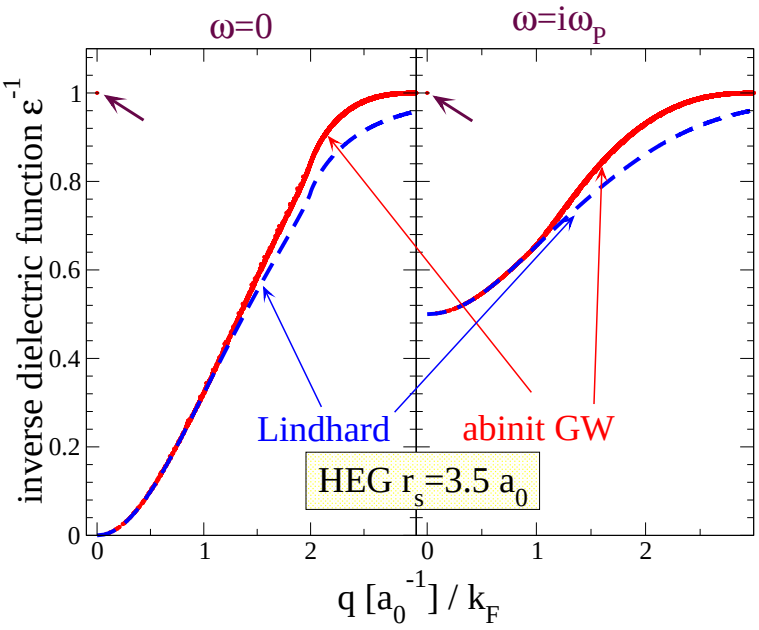

Figure 5.3: Numerically computed HEG screening function $\epsilon^{-1}(\mathbf{q},\omega)$ ($r_s = 3.5\,a_0$), for $\omega = 0$ and $\omega = i\omega_P$, compared to the Lindhard function. For $\mathbf{q} \to 0$ the discontinuously incorrect points –pointed at by arrows– appear, due to the lack of the intraband term. The differences at large $\mathbf{q}$ are due to the finite number of empty states included in the sums of Eq. (3.31).

(see Appendix A):

$$\chi_{0\,\mathbf{G},\mathbf{G}'}(\mathbf{q},\omega) = \chi_{0\,-\mathbf{G}',-\mathbf{G}}(-\mathbf{q},\omega)\,. \tag{5.1}$$

Therefore, the small-$\mathbf{q}$ expansion of $\chi_{0\,\mathbf{0},\mathbf{0}}(\mathbf{q},i\omega)$ includes only even powers of $\mathbf{q}$.

The asymptotical trend of the diagonal element of Eq. (3.31) in the small wavevector limit can be easily derived using a Taylor expansion in powers of $\mathbf{q}$:

$$\chi^{intra}_{0\,\mathbf{0},\mathbf{0}}(\mathbf{q},i\omega) \underset{\mathbf{q}\to 0}{\simeq} \frac{2}{V_{BZ}} \sum_j \int d^3k \frac{\frac{df(\epsilon_j)}{d\epsilon_j}\mathbf{q}\cdot\nabla_{\mathbf{k}}\epsilon_j}{i\omega - \mathbf{q}\cdot\nabla_{\mathbf{k}}\epsilon_j} |1 + \mathbf{q}\cdot\langle\mathbf{k},j|\nabla_{\mathbf{k}} - i\mathbf{r}|\mathbf{k},j\rangle|^2. \tag{5.2}$$

By simplifying the previous equation we get the intraband contribution to χ_0 to be:

$$\chi^{intra}_{0\,\mathbf{0},\mathbf{0}}(\mathbf{q},i\omega) \underset{\mathbf{q}\to 0}{\simeq} \frac{2}{V_{BZ}} \sum_j \int d^3k\, \delta(\mu - \epsilon_j(\mathbf{k})) \frac{\mathbf{q}\cdot\nabla_{\mathbf{k}}\epsilon_j}{i\omega - \mathbf{q}\cdot\nabla_{\mathbf{k}}\epsilon_j} |1 + \mathbf{q}\cdot\langle\mathbf{k},j|\nabla_{\mathbf{k}} - i\mathbf{r}|\mathbf{k},j\rangle|^2 \tag{5.3}$$

The diagonal matrix element in Eq. (5.3) is purely imaginary, therefore the last factor is 1 plus a $\mathbf{q}$-quadratic contribution. For $\omega = 0$ the intraband term is then a constant proportional to the density of states at the Fermi energy, plus corrections quadratic in $\mathbf{q}$. For $\omega \neq 0$ the term linear in $\mathbf{q}$ cancels because $\nabla_{\mathbf{k}}\epsilon_j$ is odd (time reversal implies $\epsilon_j(\mathbf{k}) = \epsilon_j(-\mathbf{k})$) and the integral vanishes: the expansion begins with quadratic terms. The expansion of the interband $j \neq j'$ term is easily seen to be no less than quadratic in $\mathbf{q}$. To sum up, we use the following expression:

$$\chi^{fit}_{0\,\mathbf{0},\mathbf{0}}(\mathbf{q},\omega|_{\omega=0;\omega=i\omega_P}) = A^{\omega} + \sum_{rs} B^{\omega}_{rs} q_r q_s\,, \tag{5.4}$$

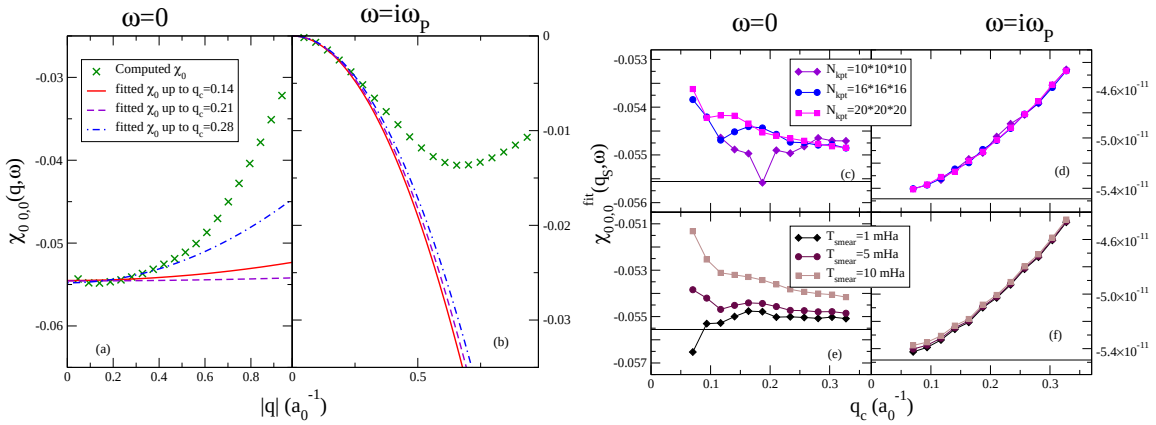

Figure 5.4: The parabolic polarizability χ_0^{fit}, Eq. (5.4), fitted to the computed $\chi_{0\,\mathbf{0},\mathbf{0}}(\mathbf{q},\omega)$ of the HEG restricted to $\mathbf{q}$-points within in a sphere of radius q_c centered at $\mathbf{q}=\mathbf{0}$, and compared to the computed polarizability itself, for (a) $\omega=0$ and (b) $\omega=i\omega_P$. The computation involves a cut-off energy of 3 Ha, $N_{\rm kpt}=16\times16\times16$ and a smearing temperature $T_{\rm smear}=0.005$ Ha. Panels (c)-(f): convergence of the fitted values $\chi_0^{fit}(\mathbf{q}_s,\omega)$ (where the tiny $\mathbf{q}_s=(7,14,21)\,10^{-6}\,a_0^{-1}$) as a function of the cutoff radius q_c, for different $\mathbf{k}$-points sampling, and with (c) $\omega=0$ and (d) $\omega=i\omega_P$, and for different smearing temperature, and with (e) $\omega=0$ and (f) $\omega=i\omega_P$. Horizontal lines: the exact (Lindhard) values.

where A^ω, B^ω_{rs} are real adjustable parameters, and $A^{i\omega_P}=0$ for $\omega=i\omega_P$. The matrices B^ω are symmetric, and may have further symmetries depending on the crystal geometry.

The off-diagonal elements $\mathbf{G}=\mathbf{0}\;\mathbf{G}'\neq\mathbf{0}$ of χ_0 (the so-called "wings" of the matrix) are affected by a similar error, since they also contain the contributions of Eq. (3.36). We also fit the intraband contribution to

$$\chi^{fit}_{0\,\mathbf{0},\mathbf{G}'}(\mathbf{q},\omega|_{\omega=0;\omega=i\omega_P}) = C^{\omega\,\mathbf{G}'} + \sum_r D^{\omega\,\mathbf{G}'}_r q_r\,, \tag{5.5}$$

where $C^{\omega\,\mathbf{G}'}$, $D^{\omega\,\mathbf{G}'}_r$ are complex adjustable parameters, and $C^{i\omega_P\,\mathbf{G}'}=0$ for $\omega=i\omega_P$.

5.3 Results

We determine the parameters A^ω, B^ω_{rs}, $C^{\omega\,\mathbf{G}'}$, and $D^{\omega\,\mathbf{G}'}_r$ in Eqs. (5.4) and (5.5) by a standard linear regression on values $\chi_{0\,\mathbf{0},\mathbf{0}}(\mathbf{q},\omega)$ and $\chi_{0\,\mathbf{0},\mathbf{G}'}(\mathbf{q},\omega)$ computed for nonzero $\mathbf{q}$-points inside a sphere of radius q_c centered in Γ. We implement this procedure within the `abinit` [62] package. To test the effectiveness of the method, we apply it to the HEG in a simple-cubic cell geometry, and to bulk sodium and aluminum in their experimental crystal structures (bcc $a=8.107\,a_0$, and fcc $a=7.652\,a_0$, respectively).

Figure 5.4 displays the fitting of the computed polarizability χ_0 of the HEG. Panels (a) and (b) compare the computed χ_0 and its small-$\mathbf{q}$ fitted parabolic expansion, for different cut-off radii q_c. Panels (c)-(f) display the resulting extrapolated small-$\mathbf{q}$ values of the polarizability as functions of the main parameters involved in the simulations

Table 5.1: Occupied bandwidth for the metals studied in this paper. The present results are compared to similar calculations and experimental data. For the HEG, the DFT-LDA result coincides with the free-electron model Fermi energy $\mathcal{E}_{\mathrm{F}} = E_{\mathrm{Ha}}\,(9\pi/4)^{2/3}(r_s/a_0)^{-2}$. All energies are in eV.

	HEG			Na	Al
r_s/a_0	3	3.5	4	3.93	2.07
DFT-LDA	5.57	4.09	3.13	3.15	11.01
HEG G_0W_0 [25]	5.24	-	2.86	-	-
HEG [65]	5.19	3.71	2.77	-	-
G_0W_0 for metals [66]	-	-	-	2.52	10.0
present work	5.17	3.84	2.89	2.81	10.03
experiment	-	-	-	2.65 [67]	10.6 [68]

and the fit. In these fits, the cut-off radius q_{c} cannot be chosen too small, otherwise the number of **q**-points becomes insufficient to perform a reliable fit. Likewise, if q_{c} is increased so much that it becomes comparable with the Fermi momentum k_{F}, the outer points are affected by the non-parabolic **q**-dependency of χ_0. Thus, an intermediate reasonably q_{c} must be used. This is especially important for $\omega = i\omega_P$, where the fit is comparably more sensitive to the value of q_{c}, as shown in Fig. 5.4(d,f).

As Fig. 5.5 shows, the corrected screening closes successfully the unphysical gap. Of course in aluminum, where the fictitious gap is almost invisible, we see no significant difference in the G_0W_0 corrections computed with and without the fit. The resulting curves are not very sensitive to the fit details, such as the value of q_{c}, or N_{kpt}. For the HEG we can compare the obtained bands with those computed *via* the Lindhard screening. The tiny and almost uniform shift is due to the truncation in the number of empty states included in the summations of Eq. (3.31), which makes the screening different in the large-**q** region, as illustrated in Fig. 5.3.

Table 5.1 reports the occupied bandwidths of the metals studied in this work compared to previous calculations and experimental values. The comparison with the DFT-LDA values shows the well-known bandwidth reduction. The results for the HEG are close to Hedin's computations [25], while in the case of Na and Al the numerical value are comparable with data in the literature [66] and are in agreement with the experimental values.

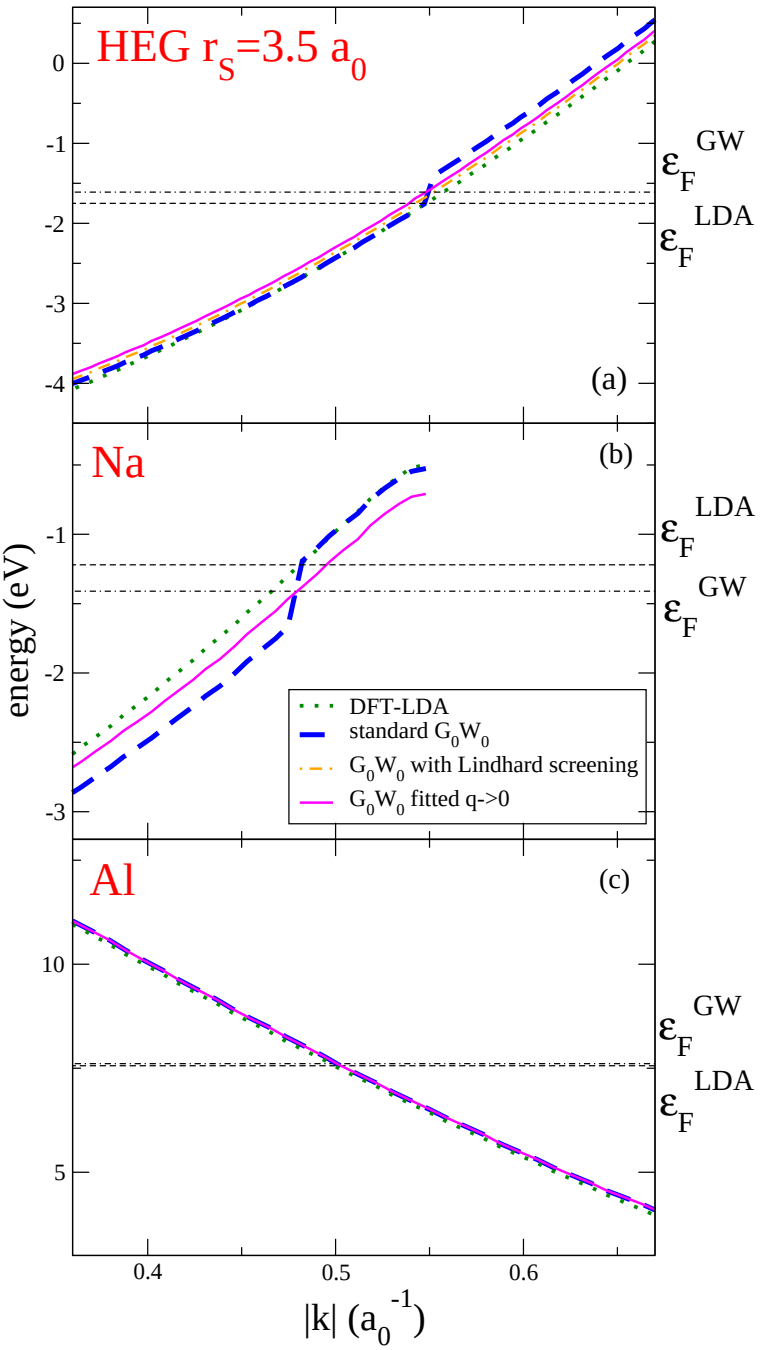

Figure 5.5: Comparison of the band energy obtained via the naive G_0W_0 calculation (dashed) to those obtained with the $\mathbf{q} \simeq 0$ corrected polarizability (solid). For the HEG (a) the figure also shows G_0W_0 results obtained with the analytic (Lindhard) polarizability. For sodium (b) and aluminum (c) the bands are plotted along the (110) and (11$\bar{1}$) directions, respectively.

Chapter 6

The inelastic X-ray scattering spectra in metals

The non-resonant inelastic X-ray scattering spectroscopy (IXSS) technique permits to access the dynamical dielectric response of solids through the measurement of the dynamical structure factor (see Appendix B). Although this kind of spectroscopy is complementary to the electron energy loss (EEL), it presents the advantage of being less surface sensitive allowing access large momenta transfer. For these reasons this technique is particularly appealing for studying the electronic excitation is solid systems [69].

From the introduction of this experimental method, several theoretical and experimental studies have been realized on a large variety of solids, including the prototypical semiconductor: bulk silicon [4, 70, 71]. Metallic systems are particularly appealing, and alkali metals, in particular, permit a direct comparison of experimental results with the HEG calculations. The interest in the HEG is due to the fact that in such a system it is possible to treat the electronic correlations beyond the simplest RPA or TDLDA approaches [50, 72, 73]. Anyway the HEG calculation cannot describe all the features appearing in the experiments as already pointed out in Sec. 4.3. For this reason full band structure calculations have been performed for both elementary metals such as aluminum [74, 75, 76], beryllium [77], and transition metals [78, 79].

In this chapter we compare both measured and calculated spectra for sodium and aluminum, considered as paradigmatic systems for nearly free-electron metals. The experiment considered here has been performed at ID16 at the ESRF by Giulio Monaco's group [73, 80]. Experimental curves have been normalized to absolute units by means of the *f*-sum rule (Appendix C). The calculations are performed in the TDDFT-linear response, as described in chapter 3, using different exchange and correlation kernels.

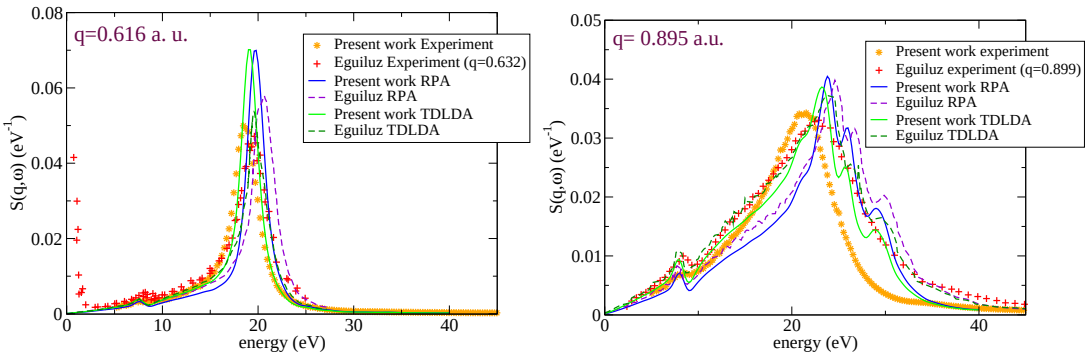

Figure 6.1: Comparison of our results with the ones in Refs. [74, 75, 76] for aluminum for two different momenta transfer along the (100) direction.

6.1 The dynamical structure factor for sodium and aluminum

The calculations presented here have been performed starting from a DFT-LDA band structure calculated with the `abinit` code [62] and taken as input for the TDDFT linear response `dp` code [81]. All the integrations on the Brillouin zone required for the calculation of the independent-particle polarizability χ_0 have been performed using 4096 shifted **k**-point mesh and including 40 bands. An electronic temperature of 5 10^{-4} Ha is needed to provide a correct evaluation of the Fermi energy and of the independent particle polarizability. For the smaller momenta, transfer a temperature of 5 10^{-5} Ha is required to converge the plasmon energy.

Despite the simplicity of these systems only few experiments and calculations have already been published. In particular, to our knowledge, some experimental results and calculated spectra are availabe for aluminum [74, 75, 76], while an electron energy loss measurement is available for sodium [82] and the comparison with theory is limited to the plasmon dispersion [83]. To be consistent with the available result we compared the measurement used for this thesis and our calculation with the ones already published. We perform such a comparison for two momenta transfer in the case of aluminum (Fig. 6.1). The two measurements reveal some differences while the calculations are very close each other. In both cases there is a good agreement between the calculations and the experiments.

6.1.1 RPA and TDLDA results

It is now possible to analyze the complete **q** dependence of the dynamical structure factor for both sodium and aluminum comparing RPA and TDLDA calculations to the IXSS measurements. Due to its similarity with the HEG we approximate sodium as an isotropic system neglecting the direction of the momenta transfer. Indeed a calculation for the same $|\mathbf{q}|$ but oriented in two different directions provided spectra with negligible differences. On the other hand aluminum, despite its simplicity, presents

some important anisotropy and the **q** direction becomes relevant. For this thesis we concentrate on **q** directed along the (100) direction. The results (Fig. 6.2, 6.3) show a sharp plasmon peak at small momenta whose energy is blueshifted even if compared with experiment. In all cases studied here TDLDA improves the agreement. On the other hand, as soon as the momentum transfer **q** increases and the plasmon falls in the electron-hole creation region ($q_C \simeq 0.4\ a_0^{-1}$ for Na and $q_C \simeq 0.6\ a_0^{-1}$ for Al) the agreement in the case of sodium worsens and the shape of the spectra starts to be different. TDLDA improves only slightly the agreement with the experiment which remains unsatisfactory. In the case of aluminum, instead, we observe smaller differences between experiment and calculations. The small peak observed in the experimental curves at intermediate momenta transfer, with energy that is twice the plasmon energy is not present at all in our numerical calculations. This feature is explained [73, 84] as a double plasmon excitation, and is not present in our results because we consider only first order polarization contributions.

6.1.2 The inclusion of quasiparticle lifetimes

We already discussed in Sec. 2.5 that the DFT energies are just a first approximation of the quasipartile energies. In particular DFT completely misses the description of the finite lifetime of the single quasiparticle states. To take into account quasiparticle lifetimes in our calculations we proceed by applying the approach described in Ref. [47], where lifetimes are introduced in χ_0 by replacing the infinitesimal broadening with the imaginary part of the self-energy (see Sec. 3.4.2).

The TDLDA together with the inclusion of lifetime effects, provides an improvement in the results for bulk silicon (Ref. [4]), although for larger frequencies the agreement becomes less clear. Such an improvement suggest that their effect is missing in TDLDA. The inclusion of the lifetimes in the calculation for both sodium and aluminum has been done by using the imaginary part of the self-energy for the HEG of Ref. [85]. At each state of the bulk solid the lifetime has been associated as imaginary part of the HEG self-energy for a state at the same energy (taking as reference the Fermi energy).

We find that also for alkali metals the effect of the lifetimes is to drive the calculation to a better agreement with the experiment (see Fig. 6.4, 6.5). In particular their effect is practically negligible for the smallest momenta since the main contributions to the spectra come from transitions close to the Fermi energy where the quasiparticles have a long lifetime. As soon as **q** increases the inclusion of lifetime turns to be decisive to provide a improvement in the results with respect to standard TDLDA. The case of sodium for very large **q** constitutes an exception, as neither standard TDLDA nor the inclusion of lifetimes are capable to provide a satisfactory agreement with the experiment. Moreover, it is not easy to pin down the reason for this disagreement as the use of the HEG lifetimes for a solid, or to a general shortcoming of this approach. In addition, as one expects, quasiparticle lifetimes just introduce a energy dependent broadening in the spectra and are not able to originate the additional double plasmon peak.

For aluminum the calculations of lifetimes present in literature, with the full inclusion of band structure, focus only on a rather limited energy range [86, 87]. For this reason the result of these calculations are not useful as starting point for the calculation of our TDDFT spectra. On the contrary, in the case of sodium a calculation of quasiparticle lifetimes for a wide energy range is available [88]. The authors show some differences in the lifetimes with respect to the HEG ones attributed to the plasmon broadening typical of real systems. In figure 6.6 the spectra calculated with the lifetimes of Ref. [88] are plotted. Despite the differences in the lifetimes the resulting spectra does not differ significantly.

6.1.3 Calculations with different kernels

The simplicity of the alkali metals permits us to evaluate the effect due to more complex kernels which exhibit a frequency or a momentum dependence.

A frequency dependent kernel is the one proposed by Gross-Kohn [37], which is a generalization of the usual static TDLDA (see Sec. 3.2.2). In this case in addition to the frequency dependency the kernel presents also an imaginary part, which is expected to broad the resulting response function spectra in similar way as the quasiparticle lifetimes. The implementation of this kernel has been performed in the same way as standard TDLDA. First of all one calculates the real space density which determines the kernel (accordingly to the assumption of locality in space the kernel depends on one spatial coordinate and on one frequency). Finally the kernel is transformed in reciprocal space using a Fourier transformation. The results are represented in Fig. 6.7. The Gross-Kohn kernel are very close to static TDLDA ones, and the differences are limited to a slight broadening of the spectra.

To test the effect of a $\mathbf{q}$-dependent kernel we considered the Hubbard local field factor [7] and the Corradini one [48]. In these cases we implemented both the kernels as if they would be applied to jellium with the density of sodium. The kernel matrix in reciprocal space is diagonal in $\mathbf{G}$ and $\mathbf{G}'$ and with the diagonal term dependent on $|\mathbf{q}+\mathbf{G}|$. The results of the calculation are plotted in Fig. 6.7. In the case of the Hubbard kernel, when we consider small momenta transferred, the plasmon dispersion is moved in the right direction. On the other hand, as soon as the $\mathbf{q}$ increases the kernel moves the spectra towards a better agreement with experiment compared to the RPA, while showing a poor agreement compared to TDLDA. Similar conclusions apply to the results with the Corradini kernel, which does not improve the TDLDA results.

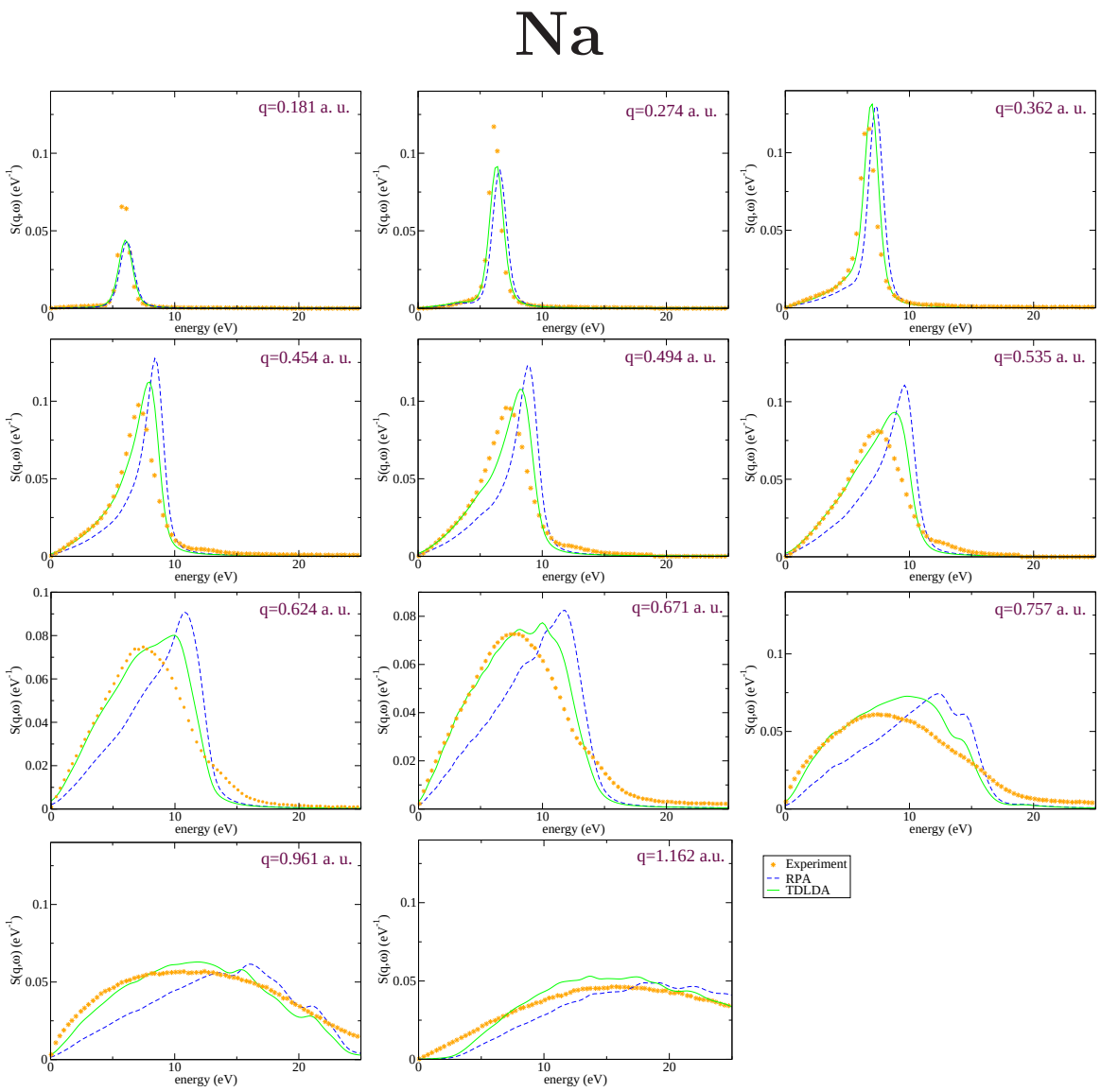

Figure 6.2: Comparison of experimental (stars) and calculated dynamical structure factor for sodium and different momentum transfer. Calculation are performed in RPA (dashed) and TDLDA (solid).

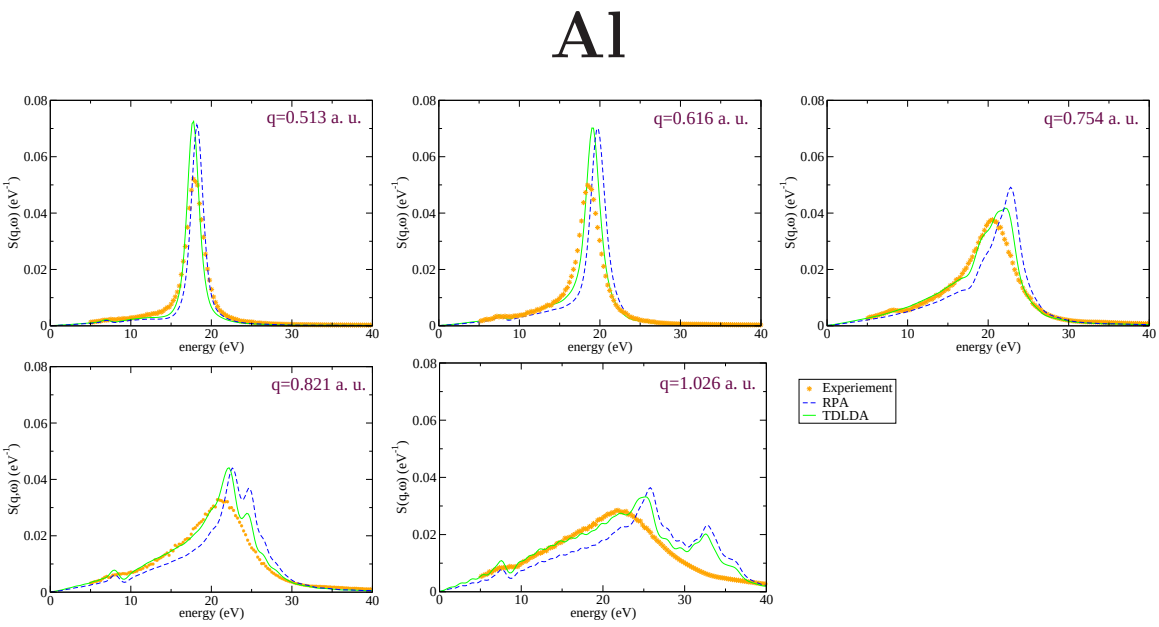

Figure 6.3: Comparison of experimental (stars) and calculated dynamical structure factor for aluminum; **q** along the (100) direction. Calculation are performed in RPA (dashed) and TDLDA (solid).

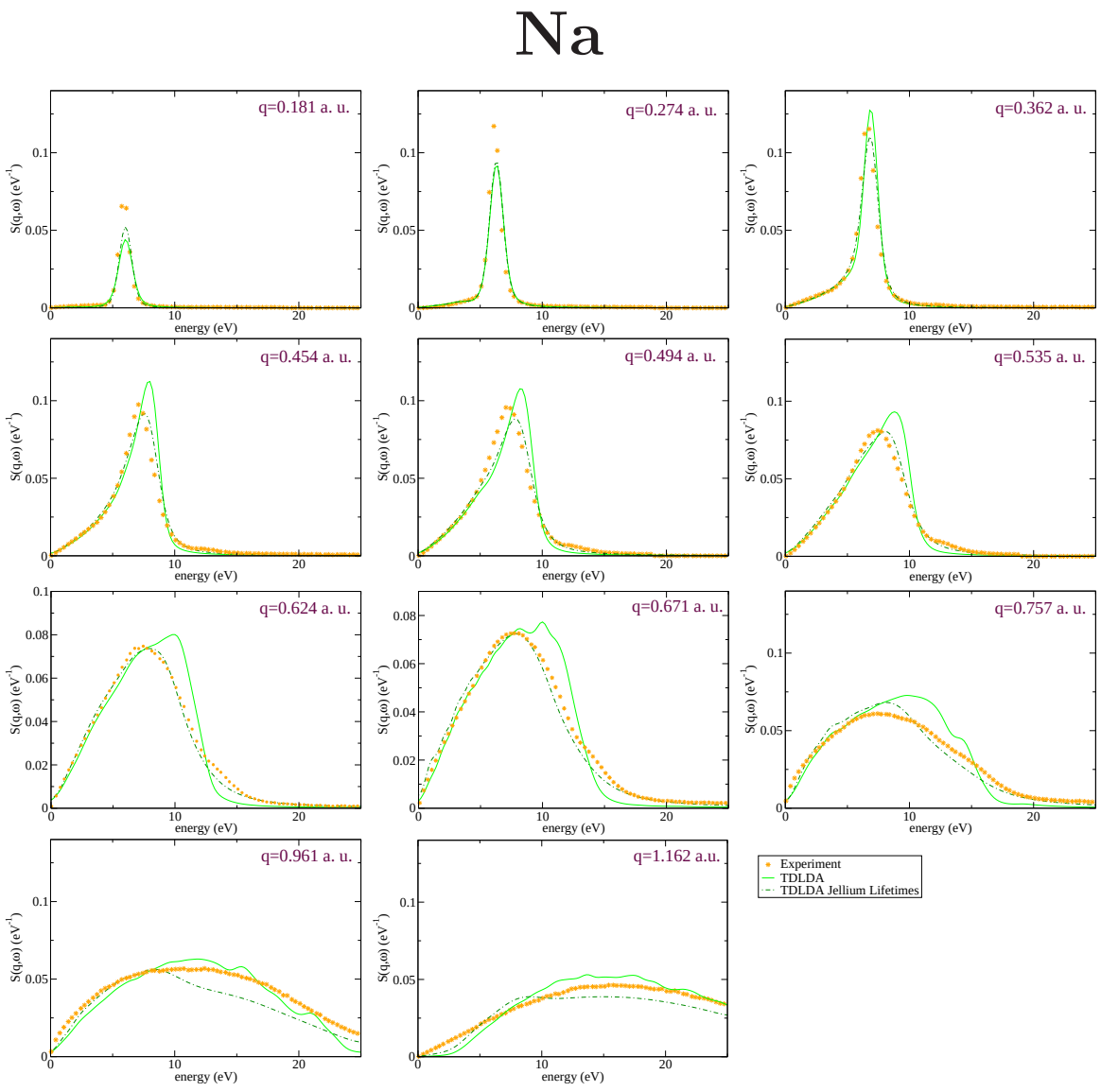

Figure 6.4: Comparison of experimental (stars) and calculated dynamical structure factor for sodium. Calculation are performed in TDLDA with (dot-dashed) and without (solid) lifetime effects.

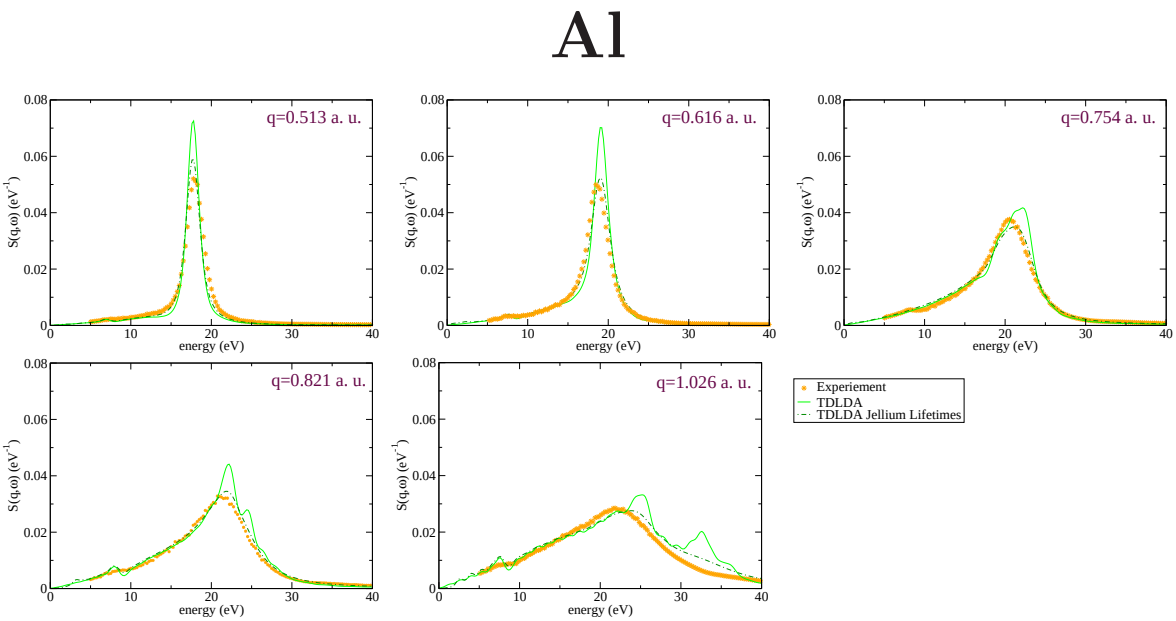

Figure 6.5: Comparison of experimental (stars) and calculated dynamical structure factor for aluminum; **q** along the (100) direction. Calculation are performed TDLDA with (dot-dashed) and without (solid) lifetime effects.

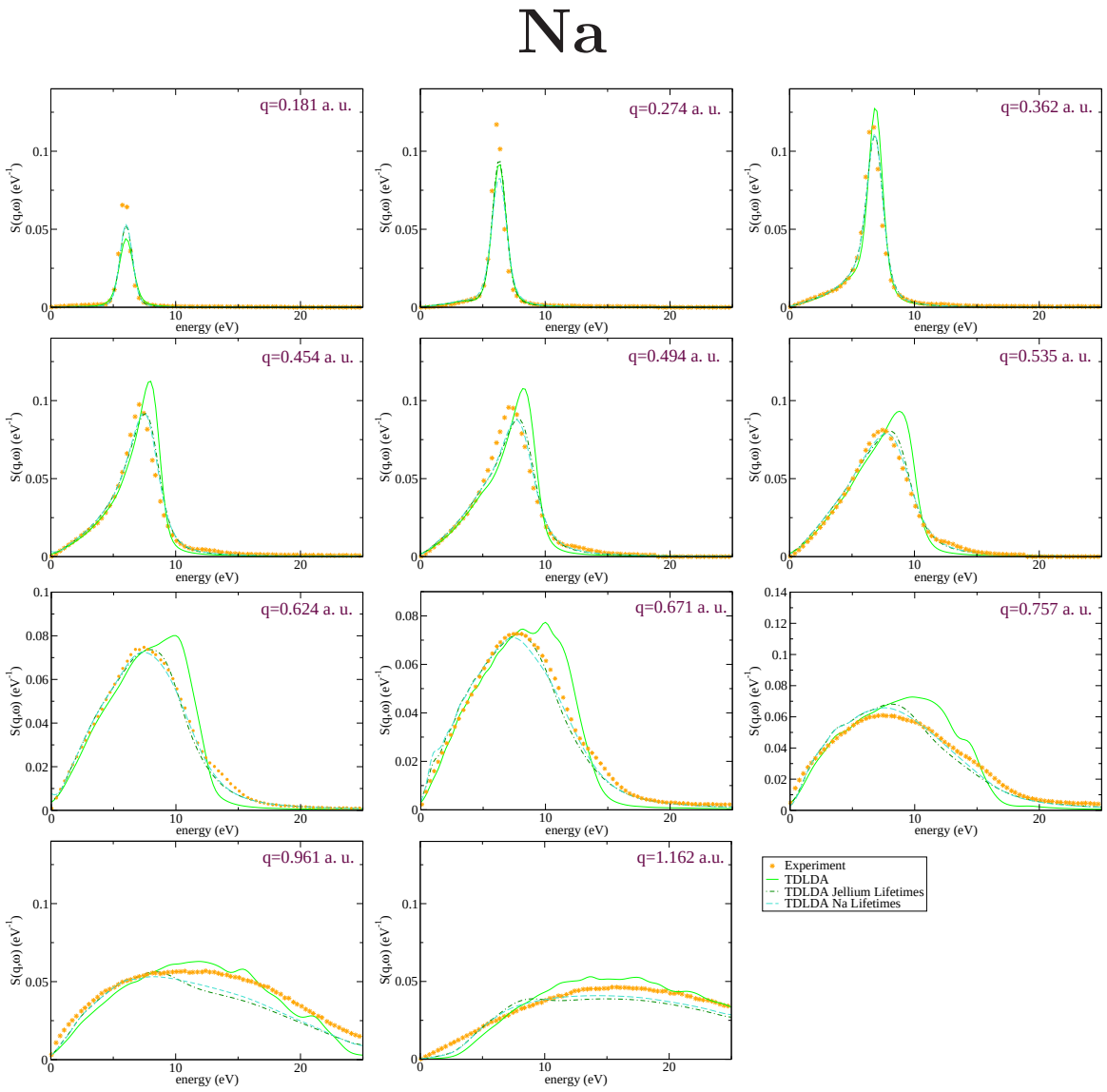

Figure 6.6: Comparison of experimental (stars) and calculated dynamical structure factor for sodium. Calculations compare the results by approximating the lifetimes with the HEG ones (dot-dashed) or with the ones calculated with the inclusion of band structure (dashed). For reference are plotted also the results for TDLDA without lifetimes (solid).

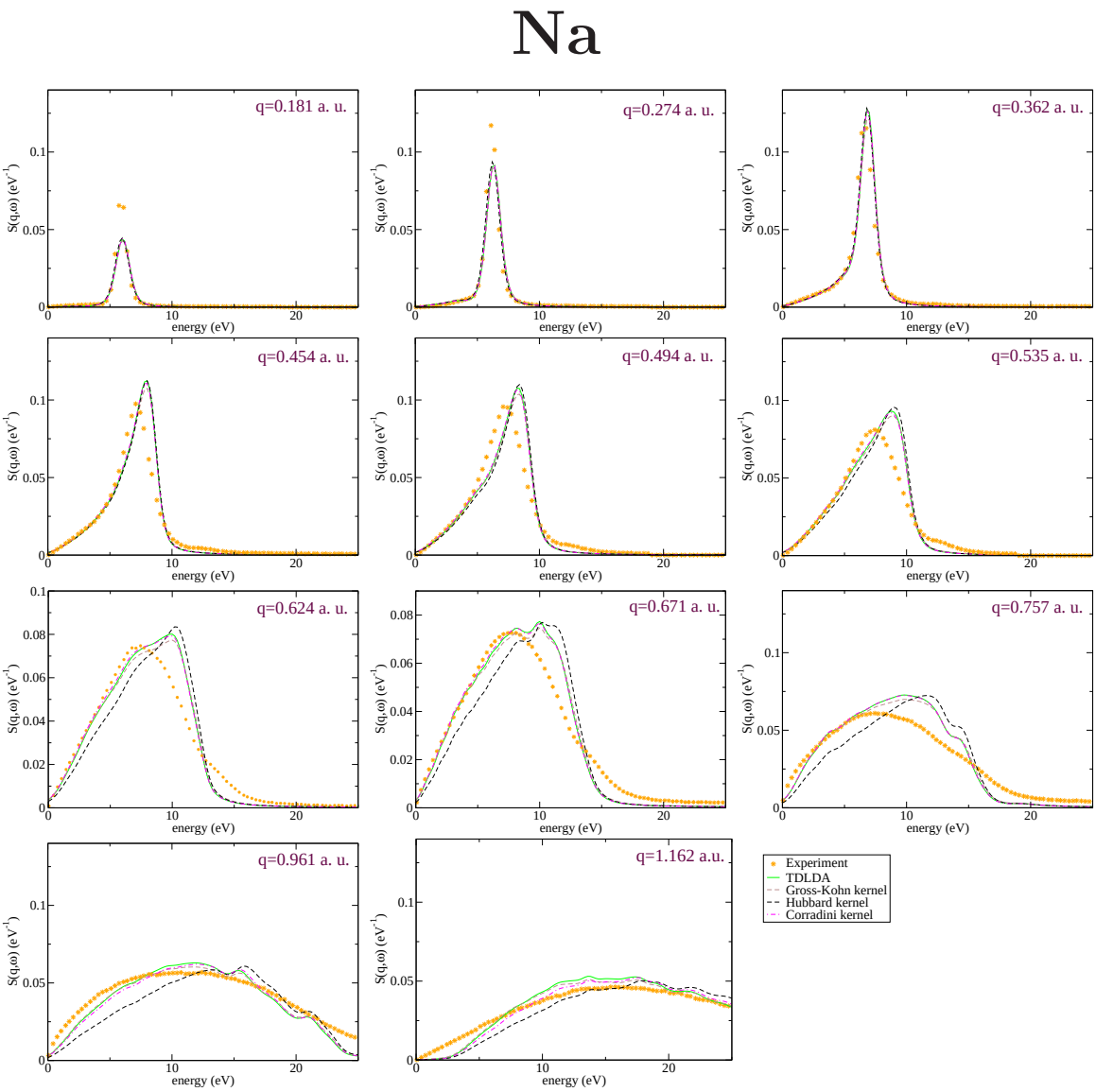

Figure 6.7: Comparison of experimental and calculated dynamical structure factor for sodium. Calculation are performed in TDLDA (solid), Gross-Kohn (brown dashed), Hubbard (black dashed) and Corradini kernels (dot-dashed).

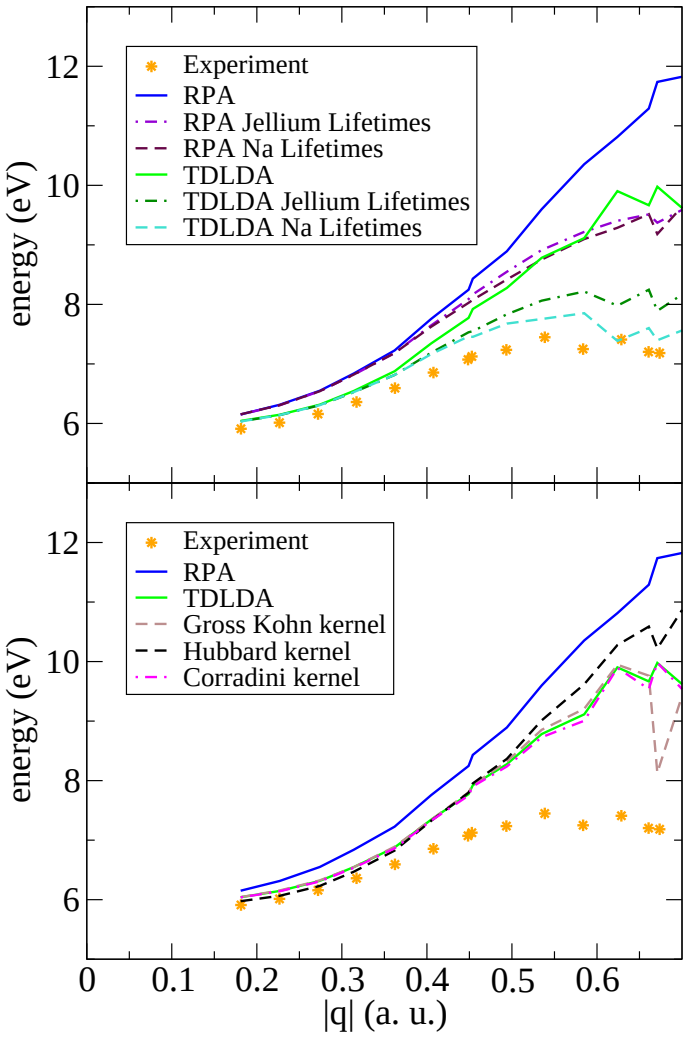

Figure 6.8: Comparison of experimental plasmon dispersion of sodium with theoretical ones. Upper panel calculation in RPA and TDLDA, and with the inclusion of quasiparticle lifetimes approximated with the HEG ones [85] and from a full band structure calculation [88]. Lower panel calculation with different exchange and correlation kernels: RPA, TDLDA, Gross-Kohn, Hubbard, and Corradini kernels.

6.2 The plasmon dispersion for sodium

To summarize the results with different kernels we present the plasmon dispersion of sodium in Fig. 6.8. The plasmon energy is defined as the energy corresponding to the maximum of the loss function, which merges with the particle-hole continuum for $q_c \simeq 0.4\ a_0^{-1}$. For $\mathbf{q} \gg q_C$ the plasmon mixes with the single particle excitations becoming less coherent. Similarly to what already observed for the HEG (Ref. [50] and Sec. 4.2.3) we observe that the TDLDA, the Gross-Kohn and Corradini kernels improve upon the RPA result for all the momentum transfers. The Hubbard kernel performs even better only for $q < q_C$, while for $q > q_C$ it provides result poorer than the TDLDA. The inclusion of quasiparticle lifetimes, calculated for the HEG, leads to a drastic improvement in the agreement with experiment especially for $q > q_C$. The approximation of lifetimes with the HEG ones is not crucial for the quality of the results.

6.3 A TDDFT kernel including lifetimes

In the previous section we have shown how the inclusion of quasiparticle finite lifetimes in χ_0 yields good agreement between the calculations and the experiment. Strictly speaking, this approach is not rigorous in the framework of TDDFT, that is supposed to start from a response function built with the Kohn-Sham eigenfunction and eigenvectors, instead of the quasiparticle corrected ones (this means that all the quasiparticle effects should be described by the kernel and not by χ_0). For this reason we are interested studying the main features of a kernel able to provide the same accuracy as the TDLDA plus lifetimes.

At this aim we invert the problem trying to determine the kernel once the density response function χ is known. If we consider the Dyson's equations for the independent-particle polarizabilities built with and without lifetimes:

$$\begin{cases} \chi = \chi_0 + \chi_0[v_C + f_{XC\,LT} + f_{TDLDA}]\chi \\ \chi = \chi_{LT} + \chi_{LT}[v_C + f_{TDLDA}]\chi \end{cases} \tag{6.1}$$

by imposing the resulting χ to be equal, we formally obtain the kernel as:

$$f_{XC\,LT} = \chi_0^{-1} - \chi_{TDLDA}^{-1} \tag{6.2}$$

In Fig. 6.9 we show the resulting $f_{XC\,LT}$ for different $\mathbf{q}$ along the (111) direction for Si. It is interesting to note that the kernel is both energy and $\mathbf{q}$ dependent. Moreover, the lifetime description in this way does not only introduce an imaginary part to the kernel, but also modifies the real part, as compared with the TDLDA kernel. While the $\mathbf{q}$ dependence reflects the nonlocality of the kernel in real space, the energy dependence is linked with the non-locality in time. The latter dependence is of course expected to describe lifetime effects. By contrast, the TDLDA kernel is local in space and time independent.

The independent-particle polarizability χ_0 is, rigorously speaking, not invertable. However, inversion using similar matrix sizes as used in the calculation of the spectra, is possible. Differently, the kernel should be better defined since due to the difference in Eq. (6.2) the singular value of χ_0^{-1} and χ_{LT}^{-1} are expected to simplify each other. In Fig. 6.10 we represent χ_0^{-1} inverted with different matrix sizes. χ_0^{-1}. χ_0^{-1} as well as χ_{LT}^{-1}, are relatively unstable with respect to the number of $\mathbf{G}$ vector used for the calculation and the inversion. However, this dependence on the number of $\mathbf{G}$ vectors cancels out when the difference of Eq. (6.2) is taken. The kernel itself is much more stable than the χ_0^{-1} and χ_{LT}^{-1} alone. The spectra produced with the resulting kernels are virtually indistinguishable (see Fig. 6.11).

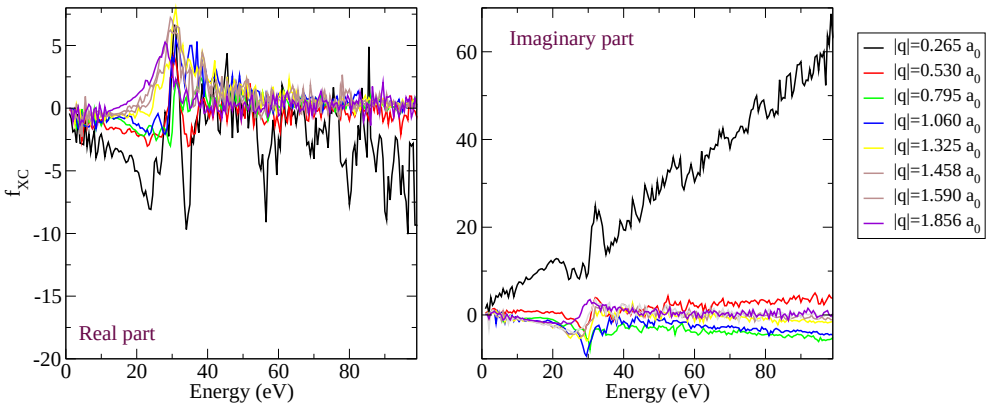

Figure 6.9: Exchange-correlation kernel $f_{XC\,LT}$ including lifetime-effects obtained according to Eq. (6.2) for the momentum transfers as indicated along (111) direction. Shown is the head of the matrix, i.e., the element $f_{XC\,LT\,\mathbf{G}=\mathbf{0},\mathbf{G}'=\mathbf{0}}$.

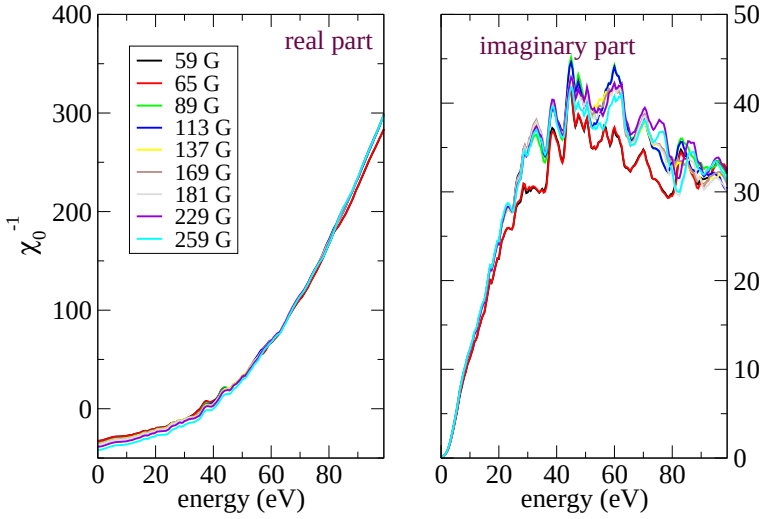

Figure 6.10: Inversion of the independent-particle polarizability χ_0^{-1} of Si with different numbers of **G** vectors. Calculation for $|\mathbf{q}| = 1.590\,a_0^{-1}$ along the (111) direction.

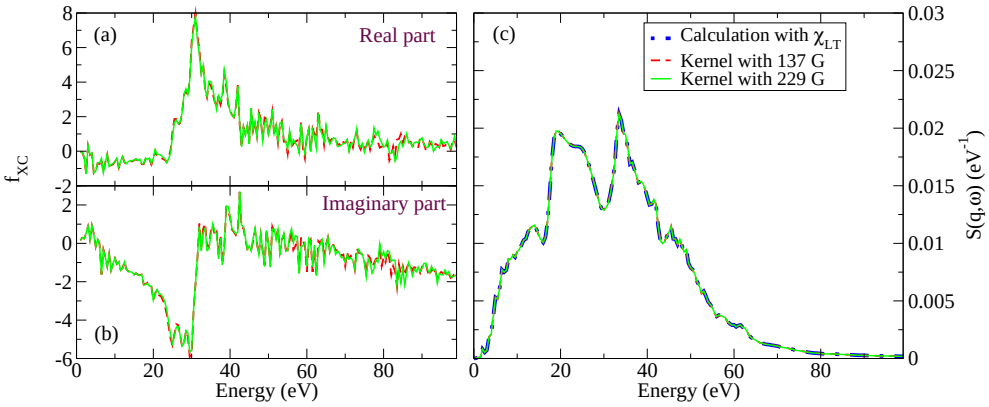

Figure 6.11: Panel (a) $f_{XC\,LT}$ calculated with two different numbers of **G** vectors, showing some differences but presenting the same main features. Panel (b) dynamical structure factors calculated with these kernels compared with the one calculated within TDLDA with lifetime inclusion. The resulting spectra are practically the same. Calculation for $|\mathbf{q}| = 1.590\ a_0^{-1}$ along the (111) direction.

Chapter 7

The optical properties of metals

In this chapter discuss the *ab initio* calculation of the optical properties of metals. The description of the small-$\mathbf{q}$ dielectric properties of a metallic system is a difficult task since it presents the same problems already described in Chapter 5 due to the description of intraband transitions. Even for semiconductors, standard TDDFT calculations, e.g. of bulk silicon, describes the loss function better than the optical absorption. The simple RPA and TDLDA are not able to describe the optical spectra and the inclusion of quasiparticle corrections (the difference of the DFT eigenvector are affected by the underestimation of the gap) and electron-hole interaction (excitonic effect included by solving the more complex Bethe-Salpeter equation) becomes necessary to provide good results [89]. This means that more complex kernels are necessary within the framework of TDDFT. Particular effort has been spent in building a kernel able to reproduce the effects coming from the quasiparticle correction and excitonic effects [46].

When dealing with metals, the effects which make RPA fail in the case of silicon are negligible. The *GW* corrections for a metal induce only a small reduction of the bandwidth, while excitons are not present since electrons and holes are better screened than in a semiconductor.

On the other hand metallic systems present the additional problem of the contributions to the response function due to intraband transitions. Despite the problem is the same as for the calculation of G_0W_0 correction we believe that the method applied in Chapter 5 is not efficient for dealing with optical properties. If that method would be applied to optical properties, it would require the evaluation of χ_0 for a large number of frequencies at finite $\mathbf{q}$ used only to perform the fit, with a not negligible computing effort.

The standard approach used in literature is essentially the description of the divergence due to the intraband transition thanks to the inclusion in the dielectric function of a Drude like contribution [8, 43]:

$$\epsilon(\mathbf{q} \to \mathbf{0}, \omega) = 1 - \frac{\omega_P^2}{\omega(\omega + i/\tau)} \tag{7.1}$$

where ω_P is the plasma frequency and τ is a parameter that describes the finite lifetimes of the quasiparticle due to the excitation induced by phonons or impurities. The

nontrivial part of this procedure is the evaluation of the plasma frequency ω_P, for calculating which, heavy integrations near the Fermi surface are required:

$$\omega_P = \lim_{\mathbf{q}\to\mathbf{0}} \frac{8\pi}{\mathbf{q}^2} \sum_j \int_{BZ} [f_j(\mathbf{k}-\mathbf{q}) - f_j(\mathbf{k})]\theta[f_j(\mathbf{k}-\mathbf{q}) - f_j(\mathbf{k})] \\ |\langle \mathbf{k}, j|e^{i\mathbf{q}\cdot\mathbf{r}}|\mathbf{k}-\mathbf{q}, j\rangle|^2 [\epsilon_j(\mathbf{k}) - \epsilon_j(\mathbf{k}-\mathbf{q})]. \tag{7.2}$$

The main disadvantage we find in such a solution is the difficulty to extend the method to highly anisotropic systems due to the fact that the Drude formula does not present any information on the direction of the small wavevector used for the calculations. A more complex method which models the anisotropies is also available [44].

Therefore, to deal with this problem we propose an approach different from the ones available in literature. The idea is to treat the intraband transitions by means of a perturbative expansion of the energies, which become treatable in the same way as for the interband ones. In the next section we will present the details of the method and in the rest of the chapter we will test the method on Al and ferromagnetic Fe.

7.1 Description of the method

In order to describe simple and complex metals, by going beyond the Drude model, we propose a direct implementation of the intraband contribution in the building of χ_0. Instead of using the transitions across the Fermi surface to evaluate ω_P we put them directly into the independent-particle polarizability. Of course since χ_0 is defined as summation over the transition one is allowed at any time to separate the inter- from the intra-band contribution and to sum them at a later time, so that Eq. (3.31) can be rewritten as:

$$\chi_{0\,\mathbf{G},\mathbf{G}'}(\mathbf{q},\omega) = \chi_0^{inter} + \chi_0^{intra} = \tag{7.3}$$
$$= -\frac{1}{V_{BZ}} \sum_{j\neq j'} \sum_{\sigma,\sigma'} \int_{BZ} d^3k \delta_{\sigma,\sigma'} \left[f(\epsilon_{j'}(\mathbf{k}+\mathbf{q})) - f(\epsilon_j(\mathbf{k}))\right] \frac{\tilde{\rho}_{j,j',\sigma,\sigma'\mathbf{G}}(\mathbf{k},\mathbf{q})\tilde{\rho}^*_{j,j',\sigma,\sigma'\mathbf{G}'}(\mathbf{k},\mathbf{q})}{\omega - [\epsilon_{j'}(\mathbf{k}+\mathbf{q}) - \epsilon_j(\mathbf{k})] + i\eta} +$$
$$-\frac{1}{V_{BZ}} \sum_{j} \sum_{\sigma,\sigma'} \int_{BZ} d^3k \delta_{\sigma,\sigma'} \left[f(\epsilon_j(\mathbf{k}+\mathbf{q})) - f(\epsilon_j(\mathbf{k}))\right] \frac{\tilde{\rho}_{j,j,\sigma,\sigma'\mathbf{G}}(\mathbf{k},\mathbf{q})\tilde{\rho}^*_{j,j,\sigma,\sigma'\mathbf{G}'}(\mathbf{k},\mathbf{q})}{\omega - [\epsilon_j(\mathbf{k}+\mathbf{q}) - \epsilon_j(\mathbf{k})] + i\eta}.$$

where $\tilde{\rho}_{j,j',\sigma,\sigma'\mathbf{G}}(\mathbf{k},\mathbf{q})$ is the matrix element $\langle \mathbf{k}, j, \sigma|e^{-i(\mathbf{q}+\mathbf{G})\cdot\hat{\mathbf{r}}}|\mathbf{k}+\mathbf{q}, j', \sigma'\rangle$,

The method we choose to add the intraband contributions is based on a first-order Taylor expansion of the dispersion law around the momenta for which the Kohn-Sham wavefunctions and eigenenergies are known; a schematic representation of this approach is sketched in Fig. 7.1. This expansion permits to approximate the energies of the states at $\mathbf{k}-\mathbf{q}/2$ and $\mathbf{k}+\mathbf{q}/2$ where $\mathbf{q}$ is a very small momentum. This choice is due to the interest in preserving the time reversal symmetry of the problem, because proceeding in this way the transition at the point $-\mathbf{k}$ will be perfectly symmetric.

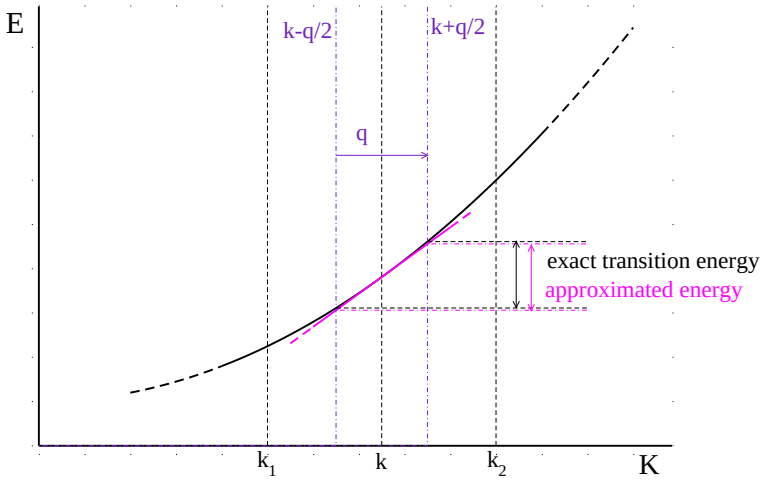

Figure 7.1: Graphical description of the expansion used for the band structure to describe the Drude contribution in χ_0. The band has been linearized to estimate the energies in $\mathbf{k} - \frac{\mathbf{q}}{2}$ and $\mathbf{k} + \frac{\mathbf{q}}{2}$.

To estimate the difference of the energies of the initial and final state we evaluate directly the first term of the expansion of the difference by using the Hellmann-Feynman theorem which sets that, considering an Hamiltonian dependent on a parameter, the derivative of the eigenenergy with respect to that parameter is the expectation value of the derivative of the Hamiltonian:

$$\frac{dE_\lambda}{d\lambda} = \langle \Psi | \frac{dH_\lambda}{d\lambda} | \Psi \rangle \tag{7.4}$$

For a Bloch periodic system the parameter is $\mathbf{k}$ and the derivative of the energy dispersion relation is the expectation value of the momentum operator[1]. For this reason the difference of energies can be approximated as:

$$\Delta\epsilon_j(\mathbf{k}) = \epsilon_j\left(\mathbf{k} + \frac{\mathbf{q}}{2}\right) - \epsilon_j\left(\mathbf{k} - \frac{\mathbf{q}}{2}\right) \simeq \mathbf{q} \cdot \frac{\partial \epsilon(\mathbf{k})}{\partial \mathbf{k}} = \mathbf{q} \cdot \langle \mathbf{k}, j | \hat{\mathbf{k}} | \mathbf{k}, j \rangle. \tag{7.5}$$

The other ingredients that are required to build χ_0 are the difference of the occupancies, and the matrix elements. The firsts can be easily evaluated as difference of the occupancies calculated at the energies corresponding to the initial and final state

$$f\left(\epsilon_j\left(\mathbf{k} + \frac{\mathbf{q}}{2}\right)\right) - f\left(\epsilon_j\left(\mathbf{k} - \frac{\mathbf{q}}{2}\right)\right) = f\left(\epsilon_j(\mathbf{k}) + \frac{\Delta\epsilon_j(\mathbf{k})}{2}\right) - f\left(\epsilon_j(\mathbf{k}) - \frac{\Delta\epsilon_j(\mathbf{k})}{2}\right). \tag{7.6}$$

This reveals to be an easier solution than performing an expansion also for the occupancies, because the Fermi-Dirac distribution can be evaluated with arbitrary precision, with much more accuracy than the Kohn-Sham energies.

The zeroth-order expansion of the matrix elements $\tilde{\rho}_{j,j,\sigma,\sigma'\mathbf{G}}(\mathbf{k}, \mathbf{q})$ is the orthonormalization between the wavefunctions of the initial and final states for the $\mathbf{G} = \mathbf{0}$ Fourier component, while a direct evaluation is possible in case of finite $\mathbf{G}$. Since also in the case of $\mathbf{G} = \mathbf{0}$ the condition of normalization for the eigenfunction is achieved by

[1] In principle, due to our pseudopotential approximation, there is also a term due to its non local part, but at this stage we neglect this contribution.

Fourier transform the product of the two wavefunctions in real space, this solution is used to calculate also the $\mathbf{G} = \mathbf{0}$ component neglecting further corrections. In formula this means:

$$\tilde{\rho}_{j,j,\sigma,\sigma'\mathbf{G}}(\mathbf{k},\mathbf{q}) = \mathcal{F}\left[\phi^*_{j,\sigma}(\mathbf{r})\phi_{j,\sigma'}(\mathbf{r})\right]. \tag{7.7}$$

Finally the Drude contribution χ_0^{intra} can be expressed as follow:

$$\chi^{intra}_{0\,\mathbf{G},\mathbf{G}'}(\mathbf{q},\omega) = -\frac{1}{2V_{BZ}}\sum_j\sum_\sigma\int_{BZ} d^3k \cdot \tag{7.8}$$

$$\left\{\left[f\left(\epsilon_j(\mathbf{k}) + \frac{\Delta\epsilon_j(\mathbf{k})}{2}\right) - f\left(\epsilon_j(\mathbf{k}) - \frac{\Delta\epsilon_j(\mathbf{k})}{2}\right)\right]\frac{\mathcal{F}\left[\phi^*_{j,\sigma}(\mathbf{r})\phi_{j,\sigma'}(\mathbf{r})\right]\mathcal{F}^*\left[\phi^*_{j,\sigma}(\mathbf{r})\phi_{j,\sigma'}(\mathbf{r})\right]}{\omega - \Delta\epsilon_j(\mathbf{k}) + i\eta}\right.$$

$$\left.+\left[f\left(\epsilon_j(\mathbf{k}) - \frac{\Delta\epsilon_j(\mathbf{k})}{2}\right) - f\left(\epsilon_j(\mathbf{k}) + \frac{\Delta\epsilon_j(\mathbf{k})}{2}\right)\right]\frac{\mathcal{F}\left[\phi_{j,\sigma}(\mathbf{r})\phi^*_{j,\sigma'}(\mathbf{r})\right]\mathcal{F}^*\left[\phi_{j,\sigma}(\mathbf{r})\phi^*_{j,\sigma'}(\mathbf{r})\right]}{\omega + \Delta\epsilon_j(\mathbf{k}) + i\eta}\right\}$$

This approach to deal with intraband transitions has been implemented in the `dp` code [81] and we applied it to bulk aluminum as benchmark system, and to ferromagnetic iron.

7.2 Optical properties of metallic aluminum

To test the present approach to the description of the intraband contribution to the response function we consider aluminum due to its jellium like behaviour. We will also compare our results with previous calculations [8] and with experimental measurements [90, 91].

7.2.1 The interband term and the random k-point sampling

The first problem one has to deal with in the case of metals is the slow convergence with the **k**-point mesh. A possible approach to improve the convergence is to use a shifted mesh of **k**-points, which converges faster because the mesh does not have the symmetries of the lattice [92]. Since optical properties involve transitions at the same **k**-point there is no need to use a regular spaced mesh. Indeed we found that an uniform random sampling performs even better than the shifted mesh due to the disappearence of the fictitious structures originated from the regular spacing (see Fig. 7.2), providing good results already with a limited number of **k**-points.

Another advantage of random meshes is the fact that to improve the accuracy of the Brillouin zone sampling it is not necessary to perform the calculations from the beginning but it is sufficient to add the new contributions in χ_0[2]:

$$\chi_0^{n_{\mathbf{k}1}+n_{\mathbf{k}2}} = \frac{n_{\mathbf{k}1}\chi_0^{n_{\mathbf{k}1}} + n_{\mathbf{k}2}\chi_0^{n_{\mathbf{k}2}}}{n_{\mathbf{k}1} + n_{\mathbf{k}2}}. \tag{7.9}$$

[2]This can be done taking care of the normalizations due to the total number of **k**-points and at condition that the mesh is generated respecting the constrain of mapping uniformly the Brillouin zone.

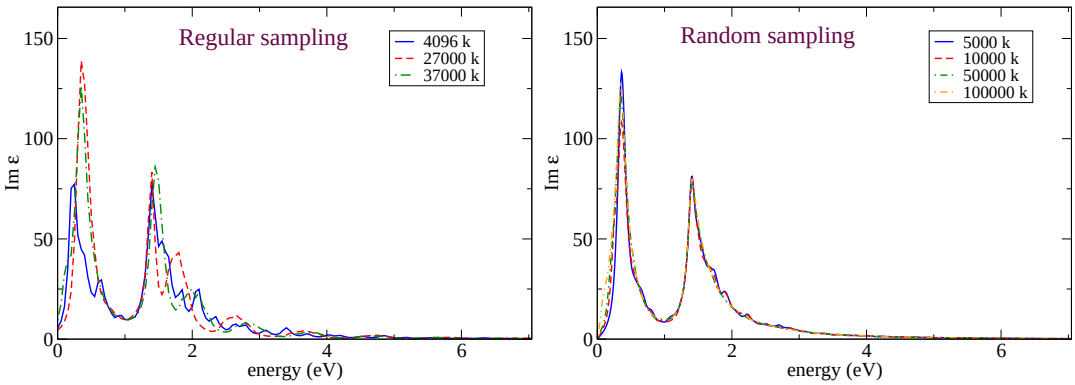

Figure 7.2: Interband contribution to the optical absorption of aluminum. Dependence of the results with the number of **k**-points used for sampling the Brillouin zone; left regular sampling, right random sampling.

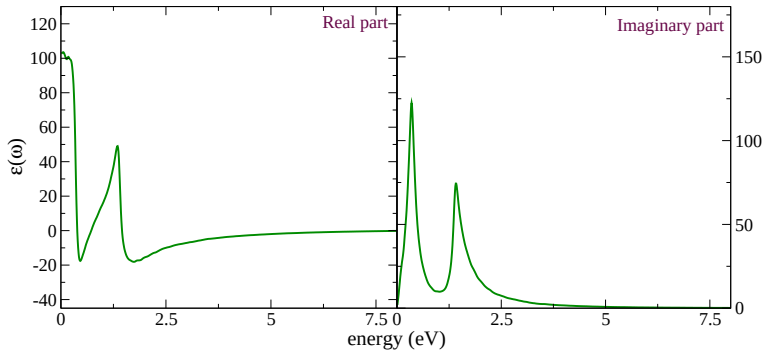

Figure 7.3: Real (left) and imaginary (right) part of the long wavelength limit for the dielectric function of aluminum. Only interband contribution are considered.

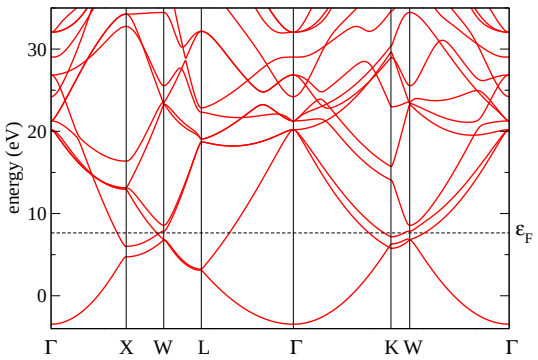

Figure 7.4: DFT band structure of metallic aluminum along some relevant symmetry directions. Notice around the Fermi energy at the W and K point the parallel bands originating the structure in the intraband dielectric function of Fig. 7.3.

For these reason in what follow a random sampling of the Brillouin zone will be used.

The resulting interband contribution to the dielectric function ϵ is plotted in Fig. 7.3. It is possible to see the presence of two structures at 0.5 eV and 1.5 eV in agreement with the result of Ref. [8]. The origin of these structure can be understood by looking at the band structure shown in Fig. 7.4. It si possible to attribute the 0.5 eV peak to the transitions between the two parallel bands close to the W point, while the other peak is due to the parallel bands close to the K point.

7.2.2 The inclusion of the Drude contribution into the dielectric function

Before comparing our results with the experiment, we present in this section the calculations performed for bulk aluminum, in order to test the accuracy and the limitations of the method used in this thesis. In particular we look at the effects of the convergence parameters on the resulting spectra and on the plasma frequency. We will neglect the convergence with respect to the cut-off energies and the **k**-points since they behave in a similar way as the well known case of semiconductors.

One crucial point is the dependence of the results with respect to the small imaginary part η added to the denominator of χ_0 necessary to avoid the divergencies at the poles. It has been already shown that this parameter has the effect of smoothing the peaks improving the **k**-point convergence. Calculations with different values of η are plotted in Fig. 7.5. While interband peaks becomes simply smoother for increasing η, this is decisive on the Drude peak. To discuss this point let us refer to the HEG case where the Lindard function computed in Sec. 4.1, is evaluated in the limit $\eta \to 0$. Its long wavelength limit is real and gives the Drude formula $\epsilon = 1 - \omega_P^2/\omega^2$. This implies that for describing optical absorption the presence of an imaginary infinitesimum is necessary. That is exactly what can be observed in the results of Fig. 7.5: the smallest value of η introduces a very thin peak at low frequencies, while only by using a rather large value for η it is possible to make the intraband peak to overlap with the first interband transition as it is evident in the experiment (see next section). In a similar way previous calculations of the optical properties use Eq. (7.1) to describe the intraband transitions, in order to provide the correct $\Im\epsilon$. In Eq. (7.1) the parameter τ introduces the requested imaginary part in the dielectric function and it is interpreted as the quasiparticle lifetime due to phonons and impurities. Of course from the point of view of the formalism applied in this thesis we have no way to determine *ab-initio* its value, so we are forced to tune it in order to have a good agreement with the experiment.

Another effect related to this issue is the way we introduce the intraband tansition in χ_0. Since the transitions are directly included in χ_0 the resulting spectra corresponds to a finite but very small-**q** calculation. This means that the computed imaginary part of the dielectric function presents an intense, but not diverging, peak at very low frequency (not visible in the figures). Similarly the real part of ϵ does not tend to $-\infty$ when $\omega \to 0$, as in the model function, but it will present an huge negative peak, which grows to its positive finite limit for $\omega = 0$. This make difficult to conclude something

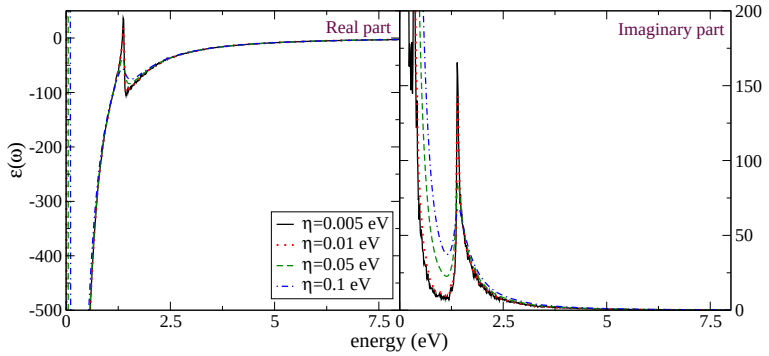

Figure 7.5: Calculation for the dielectric function of aluminum with different imaginary broadening η in the building χ_0.

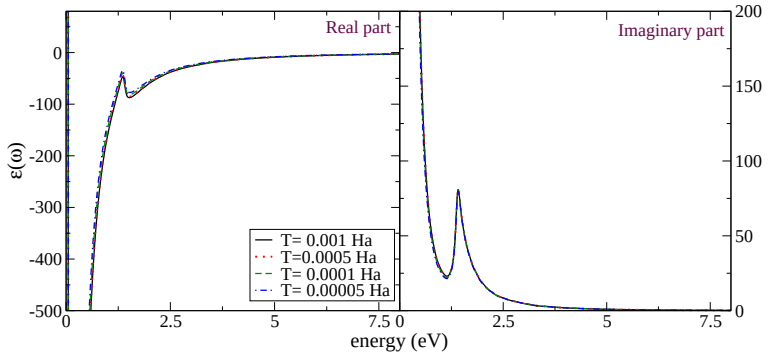

Figure 7.6: Calculation for the dielectric function of aluminum with different smearing temperatures.

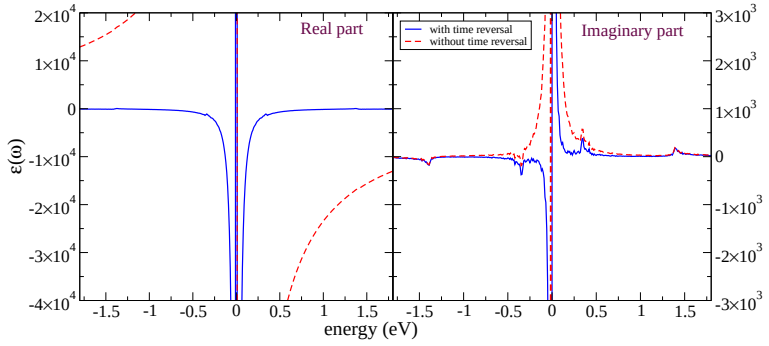

Figure 7.7: Calculation for the dielectric function of aluminum with and without time reversal symmetry for the **k**-point sampling.

Table 7.1: Palsmon energy of aluminum calculated as the zero of the real part of the dielectric function. The calculation are performed as function of the smearing temperature for two different broadenings. All values are in eV.

T_{smear} (Ha)	$1 \cdot 10^{-3}$	$5 \cdot 10^{-4}$	$1 \cdot 10^{-4}$	$5 \cdot 10^{-5}$	$1 \cdot 10^{-5}$
			$\eta = 0.05$ eV		
ω_P	15.73	15.58	15.29	14.96	16.94
			$\eta = 0.005$ eV		
ω_P	15.73	15.58	15.28	14.96	16.94

for frequencies smaller than $\approx |\mathbf{q}|k_F$, but also from an experimental approach this part of the spectra is not accessible.

Another parameter that must be carefully converged in metallic systems is the electronic temperature. This parameter is fundamental because of the finiteness of the **k**-point mesh. Indeed it is very difficult to find a suitable number of **k**-points with energy so close to the Fermi level such as to give a non zero contribution to χ_0. In Fig. 7.6 we present the effect of temperature on the calculated long wavelength limit of the dielectric function. Only small differences are present between the curves. The general trend is that by decreasing the electronic temperature the real part moves to lower frequencies (this is the same as what discussed in the previous chapter about the small-**q** convergence properties of the loss function). On the other hand, when the smearing temperature is too low the evaluation of the Fermi energy becomes difficult with a finite set of **k**-points and the spectra becomes meaningless.

In order to understand the effect of the smearing on the calculated spectra it is possible to compare the plasma frequency calculated for different electronic temperatures. The plasmon has been defined to be the zero of the real part of ϵ (table 7.1), since the local field effects are negligible in Al. The results show that the plasma frequency decreases with the electronic temperature until the plasmon becomes meaningless for a too low temperature.

A last comment deals with satisfying the time reversal invariance of the transitions contributing to the Drude peaks. As pointed out in section 7.1, we want to include in our calculation both the transitions at **k** and $-\mathbf{k}$. The reason is to preserve the symmetry $\epsilon(\omega) = \epsilon^*(-\omega)$ which cannot be satisfied if the resonant transition is not compensated with the antiresonant one. In fig 7.7 we show the results of a calculation of ϵ with or without the contributions coming from antiresonant transition. The result shows the crucial role played by the inclusion of both terms in order to give a correct evaluation of the dielectric function.

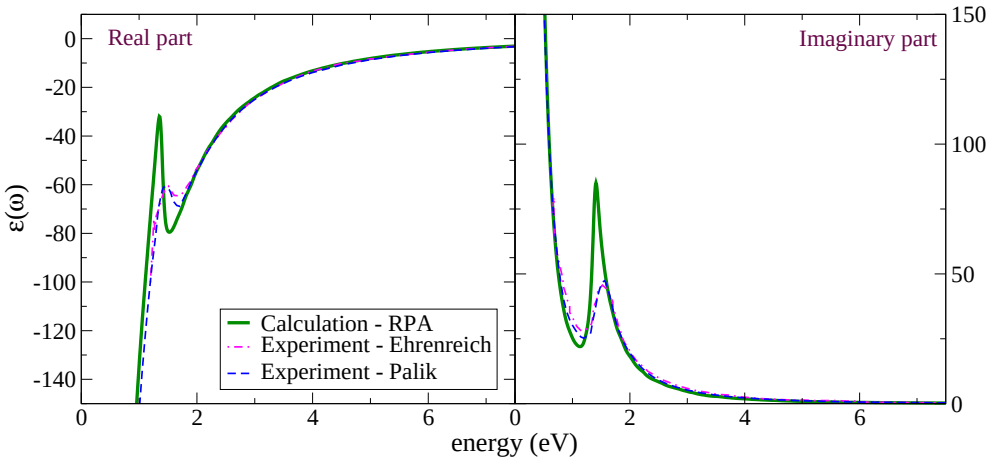

Figure 7.8: Comparison of calculated and experimental long wavelength limit of the dielectric function for aluminum. Green solid the calculated RPA results compared with the data tabuled by Palik [90] (dotted) an by Ehrenreich [91] (dash-dotted). Calculation are performed with $\eta = 0.05$ eV and $T_{\text{smear}} = 5\ 10^{-5}$ Ha.

7.2.3 Comparison with the experiment

To compare our results with the experiment we compute the response function using 10^5 random $\mathbf{k}$-points, 20 states (occupied and empty), an electronic temperature of 5 10^{-5} Ha, and a broadening $\eta = 0.05$ eV. In Fig. 7.8 the comparison of the RPA results with two sets of experimental measurements tabuled by Palik [90] an by Ehrenreich [91] is represented. It is possible to observe a good agreement between the calculation and experiment. Only the interband peak is located at a slightly too low energy and it is not broad enough.

We also perform calculation with the same kernels used in chapter 6 for the IXS spectra to investigate their effect on the optical properties. We performed calculation with TDLDA, the Gross and Kohn kernel, the Hubbard local field factor and the Corradini kernel. In Fig. 7.9 we plot the comparison between RPA and the calculation performed with these kernels. We observe that the kernels does not produce differences with respect to RPA. This can be explained with the fact that f_{XC} is smaller than the Coulombian potential v_C (which diverges for small $\mathbf{q}$), so that the sum of the two is practically equal to v_C.

7.2.4 The loss function

Starting from the results just discussed it is possible to easily obtain the loss function of aluminum. We already discussed its properties for finite momentum transfer in Chapter 6. On the other hand, measurements are possible also in the long wavelength limit [93], which is addressed in this section. Figure 7.10 reports the calculated and experimental loss function of aluminum for $\mathbf{q} = \mathbf{0}$. The calculation is in good

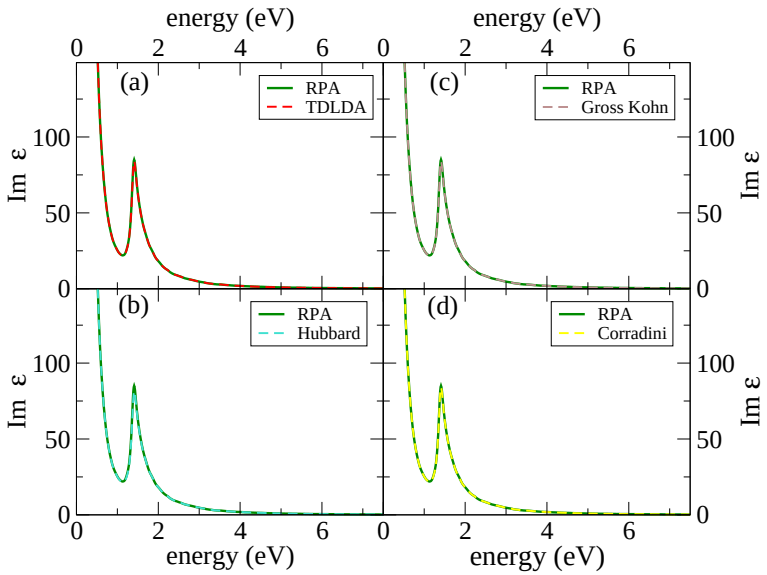

Figure 7.9: Calculation for the imaginary part of the dielectric function of aluminum with different kernel. Panel (a) shows the compartison with RPA and TDLDA, (b) the one with RPA and the Gross and Kohn kernel, (c) the one with RPA and the Hubbard local field factor and (d) the one with RPA and the Corradini kernel.

agreement with the experimental plasmon, except for a small underestimation of its energy. In addition, the weak 7 eV structure present in the experiment is not described by our calculation. For comparison Fig. 7.10 reports also the loss function calculated considering only the interband contributions. This calculation is very different from the other two results, showing the crucial role played by the Drude.

7.3 Optical properties of ferromagnetic iron

In the previous section we have shown that our method works well in bulk aluminum. On the other hand we want to test its performance on a more complex metal like ferromagnetic iron. The complexity of this system is not related to geometrical properties and anisotropies since it has a bcc lattice. The electronic structure, plotted in Fig. 7.11, however, presents more difficulties than in the case of aluminum: this material is magnetic and the Fermi energy crosses the narrow $3d$ band. The availability of a fair number of spectroscopic measurements makes this metal particularly appealing as a test case.

7.3.1 Optical absorption

The calculation of optical properties of bulk Fe is performed in the same way as for aluminum. First we perform a ground-state calculation with the `abinit` code in the LSDA approximation as discussed in Ref. [94], obtaining the band structure, plotted in

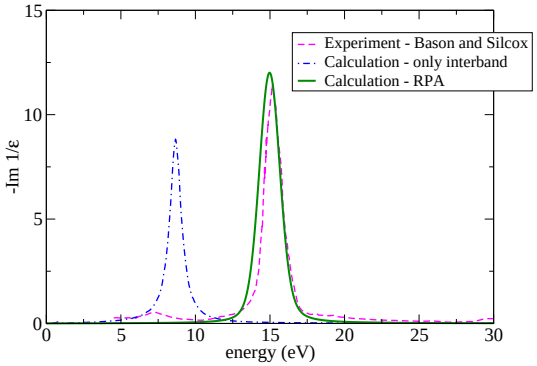

Figure 7.10: Comparison of measured (dashed) and computed (solid) electron energy loss spectra for aluminum at small momentum transfer. The calculation is performed with $\eta = 0.05$ eV, $T_{\rm smear} = 5\ 10^{-5}$ Ha. An additional Gaussian broadening of 0.6 eV is added to the spectrum. The experiment from Ref. [93] renormalized by application of the *f*-sum rule. The plot includes the loss function calculated with only the interband contributions (dot-dashed).

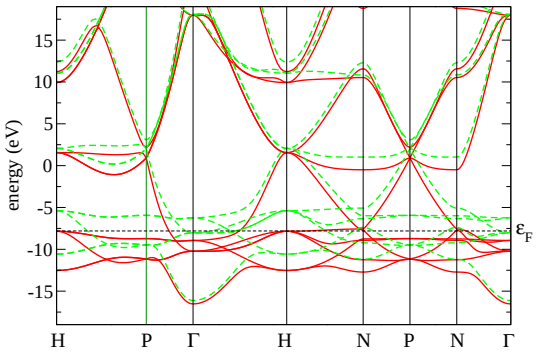

Figure 7.11: Iron band structure. LSDA calculation performed according to Ref. [94] for the two spin components, red solid and green dotted.

Fig. 7.11. Beyond this we computed the dielectric response with the `dp` code, applying the method presented in Sec. 7.1 for dealing with the Drude contribution. We map the Brillouin zone with a mesh of 40000 random **k**-points. For the calculation of the optical properties we include 40 bands. In this section we discuss a calculation performed with $\eta = 0.05$ eV and an electronic temperature of $1{\cdot}10^{-5}$ Ha. This set of parameters, according to the discussion of Sec. 7.2.2, is the one providing the best converged results.

The comparison of the calculated results with the experiments [90, 95], plotted in Fig. 7.12, is not so convincing as in the case of aluminum. The imaginary part of the calculated dielectric function of iron looks quite close to both the experimental data. The main differences are a slight overestimation of the energy interband peak, which the calculation puts at 2.7 eV while in the experiment is placed at lower energy an is much broaden. In addition there is some disagreement in the region between 0.5-1 eV where the Drude tail overlaps the interband part of the spectra. This mismatch is more evident in the real pert of ϵ. Indeed the calculated dielectric function become positive between 0.4 and 2.7 eV.

To understand weather these differences can be attributed to the evaluation of the intra- or the inter-band contribution to χ_0, we analyze the two terms separately. They are plotted in Fig. 7.13. The imaginary part of ϵ for small energies is dominated by the Drude term. For intermediate energies both terms contribute to the total spectra, while at high energy the main contribution is the interband one. It is anyway interesting to

notice the rapid decrease of the Drude peak due to the small average Fermi velocity in this system, and the presence of nonzero interband contributions even at very small energies, due to the presence of electronic bands very close to the Fermi energy[3]. The analysis of the real part leads to similar shows that the responsible for $\Re\epsilon$ becoming positive is the interband contribution which is not compensated by the Drude tail.

We also checked the effect of local fields. Since metallic iron is very different from the HEG, their effect is not obvious. The resulting RPA calculations with and without local field effects are plotted in Fig. 7.14 , showing substantially no effect.

The calculation presented here leaves still some questions about the origin of the discrepancies in the comparison of our results with experiments. The main point is to understand why the real part of the calculated dielectric function becomes positive in the region 0.4 - 2.7 eV, while in the experiment it is negative. Our impression is that there is some missing physics in the simple RPA calculation. For example in this treatment the constant η used for the present calculation is kept constant. Accordingly to what already discussed in this work it plays the role of the quasiparticle finite lifetimes, which is in fact energy dependent and, moreover, has been shown to be different for the two spin components [96]. A more accurate treatment of their effect is, therefore, to be evaluated. On the other hand another point to be investigated is the effect of the small $\mathbf{q}$ used in these calculations: the weak dispersion at the Fermi surface make us suspect that the $\mathbf{q}$ used in the calculation may be too small. Of course iron is not as simple as aluminum and it is not obvious how much the problem affecting the silicon optical properties can be relevant also for this case. In conclusion there are still open questions regarding our results and a more accurate investigation is therefore required.

7.3.2 The loss function

Analogously to the case of aluminum we also compare our EEL results with the experiment. The parameters used for the calculation are the same used in the previous section, but a Gaussian broadening of 2 eV has been added to the computed spectra. The spectra for this systems are more complex due to the more complex iron band structure. As a consequence, when comparing the calculated spectra with and without the intraband contributions (Fig. 7.15 panel a), the differences are very small and located in the small-frequency region. Consequently the main features of the loss function are due to interband transitions. The agreement with the calculations is rather good considering the complexity of the system. The main structure at 23.5 eV in the experimental spectrum corresponds to a collective excitation of the $4s$ and $3d$ electron. In the calculation we overestimate the energy of this plasmon by less than 1 eV. The other structures present in the experimental and theoretical spectra have been attributed to single particle excitation, but the complexity of the band structure makes

[3]See for example in Fig. 7.11 the spin down component around the Γ-H direction or the spin up around the N-point.

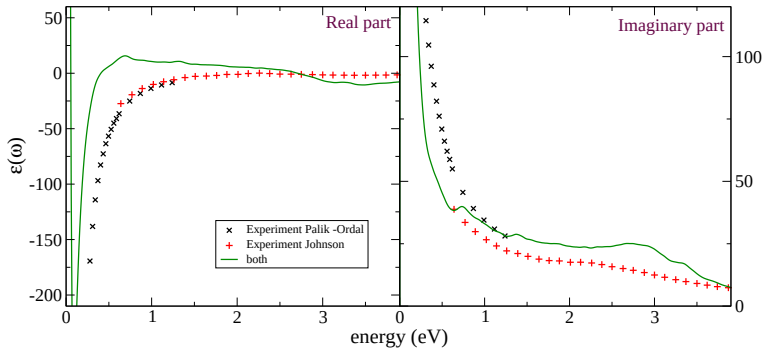

Figure 7.12: Optical properties of bulk iron. Experiment tabled by Palik [90] (crosses) or performed by Johnson and Christy [95] (plus) are compared with our RPA calculation (solid line).

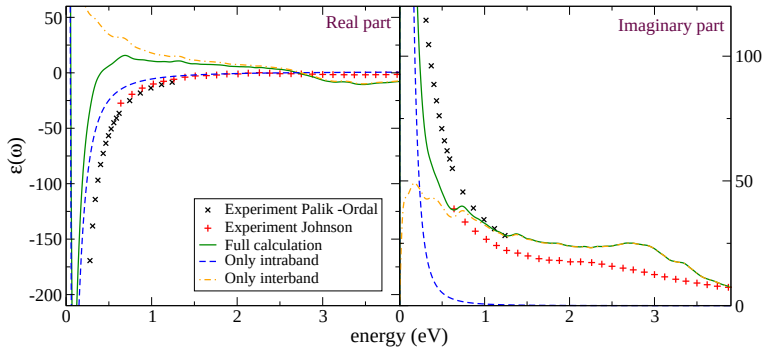

Figure 7.13: Individual inter- (dot-dashed) and intra-band (dashed) contributions to the total (solid) dielectric function of iron. Experimental points are also plotted for reference.

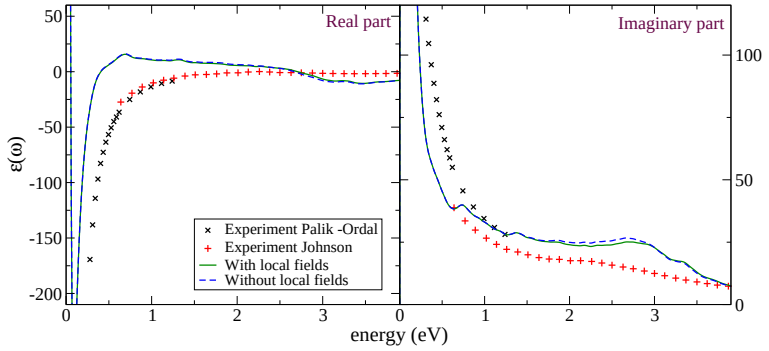

Figure 7.14: Calculated RPA dielectric function for iron with (solid) and without (dashed) local field effects. Experimental points are also plotted for reference.

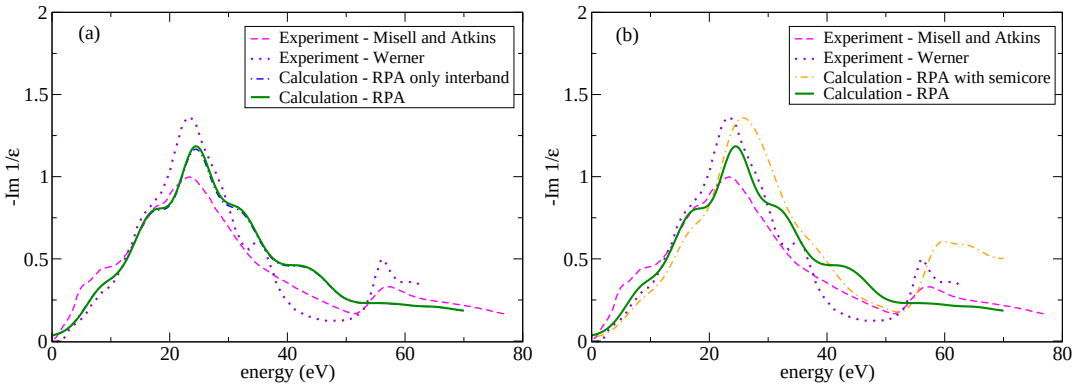

Figure 7.15: Comparison of measured and calculated electron energy loss spectra for iron at zero momentum transfer. The calculation is performed with $\eta = 0.05$ eV, $T_{\mathrm{smear}} = 1\ 10^{-5}$ Ha. An additional Gaussian broadening of 2 eV is added to the spectrum. The experiments from Ref. [97, 98]. (a) comparison of calculations with/without the Drude contribution and (b) inclusion of the semicore.

it difficult and not univocal the attribution of these structures to specific transitions [97, 99]

In the spectra it is also visible a structure at 55-60 eV which can be attributed to transitions involving a core state which is implicitly included in our calculation, trough the pseudopotential. To demonstrate the origin of this structure we performed a calculation including explicitly the $3s$ and $3p$ semicore electrons in the calculation. The calculation was performed with the same **k**-point mesh, smearing temperature and broadening η. A larger number of plane waves is required to reach convergence due to the high localization of the semicore states. For the pseudopotential details see Ref. [94]. The resulting spectrum is plotted in Fig. 7.15 (b). Our calculation with the semicore states correctly reproduces the 55 eV peak with a slightly overestimated intensity. In addition there are some differences in the calculated spectra also in the low energy region. These differences are due to the differences in the valence band structure induced by the introduction of the semicore states.

Part III

Appendices

Appendix A

Symmetry consideration for the response functions

In the present appendix we point out a few properties of the many body response function under the main symmetries of a periodic solid. In what follows we refer in general to χ_0, χ, and ϵ, pointing out the differences whenever present.

A.1 Lattice periodicity

The Bloch theorem on the wavefunctions implies that they can be written as a plane wave times a function with the lattice periodicity. The translational invariance for the two-particle response function reads:

$$\chi(\mathbf{r}, \mathbf{r}', \omega) = \chi(\mathbf{r} + \mathbf{R}, \mathbf{r}' + \mathbf{R}, \omega), \tag{A.1}$$

where $\mathbf{R}$ is a lattice vector and it is crucial that the invariance applies with a translation of both the two arguments by the same vector.

Passing in reciprocal space by Fourier transform this invariance implies that:

$$\chi(\mathbf{q}_1, \mathbf{q}_2, \omega) = \int d^3r d^3r' e^{-i\mathbf{q}_1\mathbf{r}} e^{i\mathbf{q}_2\mathbf{r}'} \chi(\mathbf{r}, \mathbf{r}', \omega) = \tag{A.2}$$

$$= \int d^3r d^3r' e^{-i\mathbf{q}_1\mathbf{r}} e^{i\mathbf{q}_2\mathbf{r}'} \chi(\mathbf{r} + \mathbf{R}, \mathbf{r}' + \mathbf{R}, \omega) \tag{A.3}$$

By a shift of the integration variables and collecting the exponential one deduces:

$$\chi(\mathbf{q}_1, \mathbf{q}_2, \omega) = \int d^3r d^3r' e^{-i\mathbf{q}_1\mathbf{r}} e^{i\mathbf{q}_2\mathbf{r}'} e^{i(\mathbf{q}_2 - \mathbf{q}_1)\mathbf{R}} \chi(\mathbf{r}, \mathbf{r}', \omega) \tag{A.4}$$

By comparing Eq. A.4 with Eq. A.2 we obtain the condition $e^{i(\mathbf{q}_2 - \mathbf{q}_1)\mathbf{R}} = 1$. This implies that the two arguments $\mathbf{q}_1$ and $\mathbf{q}_2$ must differ by a reciprocal lattice vector, and since

we can always write a vector in reciprocal space as sum of a contribution $\mathbf{q}$ inside the Brillouin zone plus a reciprocal lattice vector $\mathbf{G}$ we get the following dependence for χ:

$$\chi_{\mathbf{G},\mathbf{G}'}(\mathbf{q},\omega) \tag{A.5}$$

where $\mathbf{q}$ is inside the first Brillouin zone and $\mathbf{G}$ and $\mathbf{G}'$ are two reciprocal lattice vectors. For any $\mathbf{q}$ and ω, χ can therefore be thought as a matrix whose indexes are $\mathbf{G}$ and $\mathbf{G}'$

A.2 Time reversal invariance

Time reversal symmetry is a property of isolated physical systems due to the fact that the Shrödinger equation is invariant by replacing the time variable t with $-t$, inverting the momenta, flipping the y component of spin and taking the complex conjugate of Ψ. For a system of electrons it implies that, in the absence of magnetic field and with spin degeneracy, the Bloch wavefunction of opposite momentum are one the complex conjugate of the other $\Psi_{\mathbf{k},j}(\mathbf{r}) = \Psi^*_{-\mathbf{k},j}(\mathbf{r})$ and they are degenerate.

This symmetry implies the invariance of the correlator χ_0 and χ under the exchange of the spatial coordinates. We report the demonstration for χ_0. We start from the expression for the polarizability in direct space with inverted variables $\mathbf{r}$ and $\mathbf{r}'$:

$$\chi_0(\mathbf{r}',\mathbf{r},\omega) =$$

$$= \frac{2}{V_{BZ}} \sum_{i,j} \int_{BZ}\int_{BZ} d^3k d^3k' \, (f_{\mathbf{k}',i} - f_{\mathbf{k},j}) \, \frac{\Psi^*_{\mathbf{k},j}(\mathbf{r}')\Psi_{\mathbf{k}',i}(\mathbf{r}')\Psi^*_{\mathbf{k}',i}(\mathbf{r})\Psi_{\mathbf{k},j}(\mathbf{r})}{\omega - (\epsilon_j(\mathbf{k}) - \epsilon_i(\mathbf{k}')) + i\eta}. \tag{A.6}$$

By using time reversal on the wavefunctions:

$$\chi_0(\mathbf{r}',\mathbf{r},\omega) =$$

$$= \frac{2}{V_{BZ}} \sum_{i,j} \int_{BZ}\int_{BZ} d^3k d^3k' \, (f_{-\mathbf{k}',i} - f_{-\mathbf{k},j}) \, \frac{\Psi_{-\mathbf{k},j}(\mathbf{r}')\Psi^*_{-\mathbf{k}',i}(\mathbf{r}')\Psi_{-\mathbf{k}',i}(\mathbf{r})\Psi^*_{-\mathbf{k},j}(\mathbf{r})}{\omega - (\epsilon_j(-\mathbf{k}) - \epsilon_i(-\mathbf{k}')) + i\eta} = \tag{A.7}$$

By replacing the integration variable $\mathbf{k} \leftrightarrow -\mathbf{k}$ and $\mathbf{k}' \leftrightarrow -\mathbf{k}'$ and reordering the eigenfunctions in the numerator we obtain

$$\chi_0(\mathbf{r}',\mathbf{r},\omega) =$$

$$= \frac{2}{V_{BZ}} \sum_{i,j} \int_{BZ}\int_{BZ} d^3k d^3k' \, (f_{\mathbf{k}',i} - f_{\mathbf{k},j}) \, \frac{\Psi^*_{\mathbf{k},j}(\mathbf{r})\Psi_{\mathbf{k}',i}(\mathbf{r})\Psi^*_{\mathbf{k}',i}(\mathbf{r}')\Psi_{\mathbf{k},j}(\mathbf{r}')}{\omega - (\epsilon_j(\mathbf{k}) - \epsilon_i(\mathbf{k}')) + i\eta} =$$

$$= \chi_0(\mathbf{r},\mathbf{r}',\omega). \tag{A.8}$$

In reciprocal space the symmetry property (A.8) implies that:

$$\chi_{\mathbf{G},\mathbf{G}'}(\mathbf{q},\omega) = \chi_{-\mathbf{G}',-\mathbf{G}}(-\mathbf{q},\omega) \tag{A.9}$$

Such property does not carry forward simply to $\epsilon^{-1} = 1 - v_C\chi$ because of the presence of the Coulombian potential term $v_C = \delta_{\mathbf{G},\mathbf{G}'}\frac{4\pi}{|\mathbf{q}+\mathbf{G}|^2}$.

An other consequence of time reversal invariance applies for purely imaginary frequency: in this case χ_0 and, depending on the kernel, even χ and ϵ are real functions in direct space. Here follows the demonstration for χ_0:

$$\chi_0^*(\mathbf{r},\mathbf{r}',i\omega) = \chi_0(\mathbf{r},\mathbf{r}',-i\omega) = \chi_0(\mathbf{r}',\mathbf{r},i\omega) = \chi_0(\mathbf{r},\mathbf{r}',i\omega) \tag{A.10}$$

In reciprocal space this will imply that χ_0 is an Hermitian matrix of $\mathbf{G}$ and $\mathbf{G}'$ for every $\mathbf{q}$. The same applies to χ, but does not apply to ϵ^{-1}.

A.3 Point group

In general a crystal often has other symmetries in addition to the ones already cited. The disposition of atoms in the unit cell makes the crystal invariant under a set of transformation originating the so called point group. These operation are in general unitary transformations (inversions, rotations or a combination of the two); sometimes it is necessary to introduce a translation to have the crystal invariance (non symmorphic operation). These symmetries permit in general to reduce to study the original problem in a region of the reciprocal space smaller than the first Brillouin zone that is called the irreducible Brillouin zone.

The polarizability presents the following invariance under these symmetries:

$$\chi(R\mathbf{r}+\tau, R\mathbf{r}'+\tau,\omega) = \chi(\mathbf{r},\mathbf{r}',\omega) \tag{A.11}$$

where R is theappropriate rotation matrix and τ is the translation vector. The relation corresponding to (A.11) but in reciprocal space is:

$$\chi_{\mathbf{G},\mathbf{G}'}(\mathbf{q},\omega) = e^{iR^{-1T}(\mathbf{G}-\mathbf{G}')\cdot\tau}\chi_{R^{-1T}\mathbf{G},R^{-1T}\mathbf{G}'}(R^{-1T}\mathbf{q},\omega). \tag{A.12}$$

Appendix B

The dynamic structure factor

B.1 Definition

We consider in this appendix the description of the process inelastic scattering of a particle by a solid system [100, 101]. The Fermi golden rule permits us to write the differential cross section of such a process in a perturbation theory framework. This quantity, in both when the perturbing system is a charged particle or when it is x-ray radiation, is proportional to suitable combination of the matrix elements of the density operator:

$$\frac{d^2\sigma}{d\Omega dE} \propto \sum_{j,j'} P_{j'} \left| < \Psi_{j'} | e^{i\mathbf{q}\cdot\mathbf{r}} \hat{n}(\mathbf{r}) | \Psi_j > \right|^2 \delta(\omega - (E_j - E_{j'})). \tag{B.1}$$

where $P_{j'} = e^{-E_{j'}/k_B T}$ are the Boltzmann weights. This relation which defines the dynamical structure factor as:

$$S(\mathbf{q},\omega) = \frac{1}{n} \sum_{j,j'} P_{j'} \left| < \Psi_{j'} | e^{i\mathbf{q}\cdot\mathbf{r}} \hat{n}(\mathbf{r}) | \Psi_j > \right|^2 \delta(\omega - (E_j - E_{j'})). \tag{B.2}$$

B.2 The fluctuation and dissipation theorem

By substituting the Lehmann expansion for the density-density response function into Eq. (3.11), the microscopic dielectric function will be expressed as:

$$\begin{aligned} \epsilon^{-1}_{\mathbf{G},\mathbf{G}'}(\mathbf{q},\omega) = 1 + \frac{4\pi}{(\mathbf{q}+\mathbf{G})^2} \frac{1}{V_{BZ}} \sum_{j,j'} \frac{P_{j'} - P_j}{\omega - (E_j - E_{j'}) + i\eta} \\ < \Psi_j | e^{-i(\mathbf{q}+\mathbf{G})\cdot\mathbf{r}} \hat{n}(\mathbf{r}) | \Psi_{j'} > < \Psi_{j'} | e^{i(\mathbf{q}+\mathbf{G}')\cdot\mathbf{r}'} \hat{n}(\mathbf{r}') | \Psi_j >, \end{aligned} \tag{B.3}$$

where the energies and the wave-functions are the ones of the interacting system and $\hat{n}(\mathbf{r})$ is the density operator. When passing to the macroscopic one through the proce-

dure explained in Sec. 3.3 it becomes:

$$\epsilon_M^{-1}(\mathbf{q},\omega) = 1 + \frac{4\pi}{\mathbf{q}^2}\frac{1}{V_{BZ}}\sum_{j,j'}\frac{P_{j'} - P_n}{\omega - (E_j - E_{j'}) + i\eta}\left|< \Psi_{j'}|e^{i\mathbf{q}\cdot\mathbf{r}}\hat{n}(\mathbf{r})|\Psi_j >\right|^2. \qquad \text{(B.4)}$$

By separating the real and imaginary part by the principal values it is possible to write the imaginary part of ϵ_M:

$$\begin{aligned}
\Im\epsilon_M^{-1}(\mathbf{q},\omega) &= -\frac{4\pi^2}{\mathbf{q}^2}\sum_{j,j'}(P_{j'} - P_j)\left|< \Psi_{j'}|e^{i\mathbf{q}\cdot\mathbf{r}}\hat{n}(\mathbf{r})|\Psi_j >\right|^2\delta(\omega - (E_j - E_{j'})) = \\
&= -\frac{4\pi^2}{\mathbf{q}^2}\sum_{j,j'}P_{j'}\Big[\left|< \Psi_{j'}|e^{i\mathbf{q}\cdot\mathbf{r}}\hat{n}(\mathbf{r})|\Psi_j >\right|^2\delta(\omega - (E_j - E_{j'})) + \\
&\quad - \left|< \Psi_{j'}|e^{-i\mathbf{q}\cdot\mathbf{r}}\hat{n}(\mathbf{r})|\Psi_j >\right|^2\delta(\omega + (E_j - E_{j'}))\Big] \qquad \text{(B.5)}
\end{aligned}$$

Comparing Eq. (B.5) with the definition of the dynamic structure factor one gets (B.2):

$$\begin{aligned}
\Im\epsilon_M^{-1}(\mathbf{q},\omega) &= \frac{4\pi^2 n}{\mathbf{q}^2}[S(\mathbf{q},\omega) - S(\mathbf{q},-\omega)] = \qquad \text{(B.6)} \\
&= \frac{4\pi^2 n}{\mathbf{q}^2}[1 - e^{-\omega/k_BT}]S(\mathbf{q},-\omega)
\end{aligned}$$

which is the conclusion of the fluctuation and dissipation theorem [100].

Appendix C

The *f*-sum rule

The deduction of this sum rule for the dynamic structure factor starts from the following commutation relation [100, 102]:

$$\left[e^{-i\mathbf{qr}}\sum_i \delta(\mathbf{r}-\mathbf{r}_i), \left[H, e^{i\mathbf{qr}}\sum_i \delta(\mathbf{r}-\mathbf{r}_i)\right]\right] = Nq^2. \tag{C.1}$$

By taking the matrix element over a state $|\Psi_\alpha\rangle$ and inserting appropriately the representation of the identity $\sum_\beta |\Psi_\beta\rangle\langle\Psi_\beta|$ the previous relation becomes:

$$\sum_\beta \left|\langle\Psi_\beta|e^{i\mathbf{qr}}\sum_i \delta(\mathbf{r}-\mathbf{r}_i)|\Psi_\alpha\rangle\right|^2 (E_\beta - E_\alpha) = N\frac{q^2}{2}. \tag{C.2}$$

Summing up over the states $|\Psi_\alpha\rangle$ and dividing by the cell volume Eq. (C.2) becomes:

$$\frac{1}{V_{BZ}}\sum_{\alpha,\beta} P_\alpha \left|\langle\Psi_\beta|e^{i\mathbf{qr}}\sum_i \delta(\mathbf{r}-\mathbf{r}_i)|\Psi_\alpha\rangle\right|^2 (E_\beta - E_\alpha) = n\frac{q^2}{2}. \tag{C.3}$$

It can be easily observed that the left term of Eq. (C.3) is proportional to the loss function. This permit to write the *f*-sum rule:

$$\int_0^\infty -\Im\frac{1}{\epsilon(\mathbf{q},\omega)}\omega d\omega = \frac{4\pi^2}{\mathbf{q}^2}\frac{n\mathbf{q}^2}{2} = \frac{4\pi^2 n}{2} \tag{C.4}$$

In particular, it is possible to recognize on the right term of the previous equation the expression for the plasma frequency ω_P for the HEG of density n. In this sense the sum rule can be written as

$$\int_0^\infty -\Im\frac{1}{\epsilon(\mathbf{q},\omega)}\omega.d\omega = \frac{\omega_P}{2} \tag{C.5}$$

In addition by definition of $S(\mathbf{q},\omega)$ the sum rule can be equivalently written in the limit $T \to 0$

$$\int_0^\infty S(\mathbf{q},\omega)\omega d\omega = \frac{\mathbf{q}^2}{2}. \tag{C.6}$$

Appendix D

The Kramers-Kronig relation

The Lehamn representation of the retarded response functions shows clearly that, when the frequency domain is extended to the whole complex plane, their poles are placed just below the real axis, implying the analyticity in the upper half-plane. This is the basis for the deduction of the Kramers-Kronig relation [36].

D.1 The relations

The deduction starts by considering that the shown analyticity of χ implies that the following contour integration vanishes

$$\int_{\Gamma} \frac{1}{2\pi i} \frac{\chi(\mathbf{q}, z)}{z - \omega} dz = 0, \tag{D.1}$$

where the countour Γ is composed by the real axis with a small semicircle in the upper half plane to skip the pole at $z = \omega$, and is closed with the semicircle of radius going to infinity. If this contour is separated into its single segments and the integration is performed separately, the contribution due to the semicircle at infinite is zero due to the integrand vanishing in such a limit. The remaining contributions yield

$$\int_{-\infty}^{\infty} \frac{1}{2\pi i} \frac{\chi(\mathbf{q}, \omega')}{\omega' - \omega} d\omega' - \frac{1}{2}\chi(\mathbf{q}, \omega) = 0. \tag{D.2}$$

Rearranging the previous result and separating real and imaginary part we get:

$$\Re\chi(\mathbf{q}, \omega) = \frac{1}{\pi} P \int_{-\infty}^{\infty} \frac{\Im\chi(\mathbf{q}, \omega')}{\omega' - \omega} d\omega' \tag{D.3}$$

$$\Im\chi(\mathbf{q}, \omega) = -\frac{1}{\pi} P \int_{-\infty}^{\infty} \frac{\Re\chi(\mathbf{q}, \omega')}{\omega' - \omega} d\omega' \tag{D.4}$$

which are the Kramers-Kronig relations By using the property $\chi(\mathbf{q},\omega) = \chi^*(\mathbf{q},-\omega)$ the previous relations can be written in a different form:

$$\Re\chi(\mathbf{q},\omega) = \frac{2}{\pi}P\int_0^\infty \frac{\omega'\Im\chi(\mathbf{q},\omega')}{\omega'^2-\omega^2}d\omega' \tag{D.5}$$

$$\Im\chi(\mathbf{q},\omega) = -\frac{2\omega}{\pi}P\int_0^\infty \frac{\Re\chi(\mathbf{q},\omega')}{\omega'^2-\omega^2}d\omega'. \tag{D.6}$$

These relation for the dielectric functionimply that

$$\Re\epsilon(\mathbf{q},\omega) = 1 + \frac{2}{\pi}P\int_0^\infty \frac{\omega'\Im\epsilon(\mathbf{q},\omega')}{\omega'^2-\omega^2}d\omega' \tag{D.7}$$

$$\Im\epsilon(\mathbf{q},\omega) = -\frac{2\omega}{\pi}P\int_0^\infty \frac{\Re\epsilon(\mathbf{q},\omega')-1}{\omega'^2-\omega^2}d\omega'. \tag{D.8}$$

D.2 Numerical evaluation

The presence of a pole in the integrand makes the numerical evaluation of the principal value integration required by the Kramers-Kronig relation not possible with standard discrete algorithms. The simplest solution one can think at is just to perform the integration with the rectangular method just skipping the contribution at the pole. This method reveals too simple and is not able to provide particularly accurate results. In this thesis we choose the algorithm described in the following.

We start by separating separate the part contributing to the pole so that the relation becomes:

$$\int_0^\infty \frac{f(\omega')}{\omega^2-\omega'^2}d\omega' = \int_0^\infty \frac{f(\omega')}{\omega+\omega'}\frac{1}{\omega-\omega'}d\omega' = \int_0^\infty \frac{g(\omega,\omega')}{\omega-\omega'}d\omega' \tag{D.9}$$

We perform the integration with a regular sampling which contains $\omega = \omega'$ and stop the integration at a large frequency where the integrand is practically zero.

The total integral is estimated by the sum of many contributions computed on the individual intervals $[\omega_j, \omega_{j+1}]$ of width Δ. In the case the pole is not at one extremum of the integration interval, the contribution to the result is evaluated by estimating $g(\omega,\omega')$ as its average at the extrema (since it is evaluated numerically it is known only at those points) and performing analytically the remaining integration; in formula:

$$\int_{\omega_j}^{\omega_{j+1}} \frac{g(\omega,\omega')}{\omega-\omega'}d\omega' = \frac{g(\omega,\omega_j)+g(\omega,\omega_{j+1})}{2}\log\left(\frac{\omega-\omega_{j+1}}{\omega-\omega_j}\right). \tag{D.10}$$

The remaining case, with the pole at one of the integration extremum is more complicated. To perform which we proceed by calculating the contribution of both the intervals $[\omega-\Delta,\omega]$ and $[\omega,\omega+\Delta]$ together since it requires to evaluate

$$P\int_{\omega-\Delta}^{\omega+\Delta} \frac{g(\omega,\omega')}{\omega-\omega'}d\omega' = \lim_{\eta\to 0}\int_{\omega-\Delta}^{\omega-\eta} \frac{g(\omega,\omega')}{\omega-\omega'}d\omega' + \int_{\omega+\eta}^{\omega+\Delta} \frac{g(\omega,\omega')}{\omega-\omega'}d\omega' = \tag{D.11}$$

Performing the integration by parts this contribution becomes:

$$\begin{aligned} = \lim_{\eta\to 0} \quad & g(\omega,\omega'-\eta)\log(\eta) - g(\omega,\omega'+\eta)\log(\eta) - g(\omega,\omega'-\Delta)\log(\Delta) + \\ + \quad & g(\omega,\omega'+\Delta)\log(\Delta) - \int_{\omega-\Delta}^{\omega-\eta} g'(\omega,\omega')\log|\omega-\omega'|d\omega' + \\ + \quad & \int_{\omega+\eta}^{\omega+\Delta} g'(\omega,\omega')\log|\omega-\omega'|d\omega' = \end{aligned} \tag{D.12}$$

where $g'(\omega,\omega')$ is the derivative of g with respect to ω'. The first two addends simplify in the limit $\eta \to 0$. By changing the variable in the first integral as $\omega'' = 2\omega - \omega'$ and recalling $\omega'' + \omega'$ it becomes:

$$\begin{aligned} = \lim_{\eta\to 0} \quad & -g(\omega,\omega'-\Delta)\log(\Delta) + g(\omega,\omega'+\Delta)\log(\Delta) + \\ + \quad & \int_{\omega+\eta}^{\omega+\Delta} [g'(\omega,\omega') - g'(\omega,2\omega-\omega')]\log|\omega-\omega'|d\omega' = \end{aligned} \tag{D.13}$$

approximating the derivative $g'(\omega,\omega') \simeq [g(\omega,\omega+\Delta) - g(\omega,\omega)]/\Delta$, $g'(\omega,2\omega-\omega') \simeq [g(\omega,\omega) - g(\omega,\omega-\Delta)]/\Delta$ and performing the remain integration analytically the contribution of the two intervals results:

$$P\int_{\omega-\Delta}^{\omega+\Delta} \frac{g(\omega,\omega')}{\omega-\omega'}d\omega' = g(\omega,\omega+\Delta) - g(\omega,\omega-\Delta) \tag{D.14}$$

Conclusions

In this work we have developed new numerical methods and performed *ab initio* simulations aimed to improve our understanding of experiments probing single quasiparticle excitations and dielectric properties of materials, focusing our attention on metallic systems. We investigated the properties of these systems by using two well established, but still challenging, methods: the GW approximation and the TDDFT-linear response formalism. Our attention has been devoted mainly to the dielectric/density-response of metals, which is the fundamental ingredient for all calculations presented in this thesis and to understand the excited state properties of a solid.

As first application we devoted our attention to single quasiparticle excitations of metals. At this aim we performed G_0W_0 calculations for the HEG, sodium and aluminum. We found the opening of an unphysical gap in the G_0W_0 dispersion attributed to the omission of the intraband contribution in the screened interaction. To correct this problem we proposed a simple, costless, method based in the determination of the small wavevector contribution to the polarizability by fitting the finite-$\mathbf{q}$ asymptotic. The so obtained results close the unphysical gap. In addition our results provide comparable bandwidths compared to previous calculation and with photoemission experiments.

We devoted our attention also to the interpretation of dielectric spectroscopies starting from the inelastic X-ray scattering spectroscopies. We compared numerical calculation of the dielectric response in TDDFT linear response formalism with measured dynamical structure factor for sodium and aluminum. The calculations were performed with electronic correlations treated at different level by the use of different exchange and correlation kernels (RPA, TDLDA, Gross-Kohn kernel, Hubbard local field factor and Corradini kernel). The best agreement was obtained with TDLDA with the inclusion of finite quasiparticle lifetimes. While the plasmon is described quite well by all the kernels (with the exception of RPA which slightly overestimate it), as soon as the momentum transfer enter in the particle hole creation region the agreement worsens and the inclusion of lifetimes becomes decisive to improve the agreement theory-experiment. For the larger $\mathbf{q}$ the agreement remain unsatisfactory and at this stage the reason is not clear.

In this framework we tried to discuss also the problem originated by the fact that lifetimes effects should not be inserted by hand in χ_0, but the kernel should take them into account. Such effects are described by the TDLDA kernel. To move into the direction of a kernel describing also the effects coming from the imaginary part of the

quasiparticle energy, we inverted the problem to have some hints on the aspect of the unknown kernel. Despite the conceptual problems in performing the inversions, we showed how the kernel should be far from trivial, sine it has to present not only an expected imaginary part and a non locality in time, but it is relevant also its real part and a nonlocality in space (dependence on the wavevector).

The last application of *ab initio* techniques we analyzed is devoted to the calculation of optical properties of metallic systems. At this aim we introduced a new approach to deal with the intraband term based on the direct inclusion of the transition in the building χ_0, by evaluating the difference of energies appearing at the denominator by the Helmann-Feynman theorem. We tested the performance of our approach on bulk aluminum calculating both the dielectric properties and the loss function. In both cases we obtained good agreement withe experiments.The description of the broadening of the spectra which remains an adjustable parameters remain missing in the theory. We applied this approach also to bulk iron. We calculated the same quantities as for aluminum with an additional calculation with semicore due to the clear visibility of the edge in the energy loss experiment. While the agreement for the loss function remains satisfactory also for this system, there are still some open point to understand the behaviour of the optical spectra.

Bibliography

[1] R. M. Dreizler and E. K. U. Gross, *Density Functional Theory*, Springer-Verlag, Berlin, 1990.

[2] For a review see: G. Onida, L. Reining, and A. Rubio, Rev. Mod. Phys. **74**, 601 (2002).

[3] M. S. Hybertsen and S. G. Louie, Phys. Rev. B **34**, 5390 (1986).

[4] H.-Ch. Weissker et al., Phys. Rev. Lett. **97**, 237602 (2006).

[5] L. Reining, V. Olevano, A. Rubio, and G. Onida, Phys. Rev. Lett. **88**, 066404 (2002).

[6] L. Hedin and S. Lundqvist, Effects of electron-electron and electron-phonon interactions on the one-electron states of solids, in *Solid state physics*, edited by F. Seitz, D. Turnbull, and H. Ehrenreich, page 1, Academic Press, New York, 1969.

[7] G. D. Mahan, *Many particle physics*, Plenum Press, New York, 1981.

[8] K.-H. Lee and K. J. Chang, Phys. Rev. B **49**, 2362 (1994).

[9] M. Cazzaniga, Computation of electronic properties of metallic surfaces: total energy and quasiparticle excitations, Master's thesis, Universitá degli Studi di Milano, 2005.

[10] P. Hohenberg and W. Kohn, Phys. Rev. **136**, B864 (1964).

[11] W. Kohn and L. J. Sham, Phys. Rev. **140**, A1133 (1965).

[12] D. M. Ceperley and B. J. Alder, Phys. Rev. Lett. **45**, 566 (1980).

[13] J. P. Perdew and A. Zunger, Phys. Rev. B **23**, 5048 (1981).

[14] S. H. Vosko, L. Wilk, and M. Nusair, Can. J. Phys. **58**, 1200 (1980).

[15] J. P. Perdew and Y. Wang, Phys. Rev. B **45**, 13244 (1992).

[16] J. P. Perdew and W. Yue, Phys. Rev. B **33**, 8800 (1986).

[17] M. C. Payne, M. P. Teter, D. C. Allan, T. A. Arias, and J. D. Joannopoulos, Rev. Mod. Phys. **64**, 1045 (1992).

[18] N. W. Ashcroft and N. D. Mermin, *Solid State Physics*, Harcourt College Publishers, Orlando, 1976.

[19] V. M. Galitskii and A. B. Migdal, Sov. Phys.-JEPT **7**, 96 (1958).

[20] A. L. Fetter and J. D. Walecka, *Quantum Theory of Many-particle Systems*, McGraw-Hill, San Francisco, 1971.

[21] M. Gell-Mann and F. Low, Phys. Rev. **84**, 350 (1951).

[22] G. C. Wick, Phys. Rev. **80**, 268 (1950).

[23] L. Hedin, J. Phys.: Condens. Matter **11**, R489 (1999).

[24] F. Aryasetiawan and O. Gunnarsson, Rep. Prog. Phys. **61**, 237 (1998).

[25] L. Hedin, Phys. Rev. **139**, A796 (1965).

[26] M. van Schilfgaarde, T. Kotani, and S. Faleev, Phys. Rev. Lett. **96**, 226402 (2006).

[27] T. Kotani, M. van Schilfgaarde, and S. V. Faleev, Phys. Rev. B **76**, 165106 (2007).

[28] R. W. Godby, M. Schlüter, and L. J. Sham, Phys. Rev. B **37**, 10159 (1988).

[29] B. Holm and U. von Barth, Phys. Rev. B **57**, 2108 (1998).

[30] W.-D. Schöne and A. G. Eguiluz, Phys. Rev. Lett. **81**, 1662 (1998).

[31] G. D. Mahan and B. E. Sernelius, Phys. Rev. Lett. **62**, 2718 (1989).

[32] M. A. L. Marques and E. K. U. Gross, Ann. Rev. Phys. Chem. **55**, 427 (2004).

[33] S. Botti, A. Schindlmayr, R. Del Sole, and L. Reining, Rep. Progr. Phys. **70**, 357 (2007).

[34] E. Runge and E. K. U. Gross, Phys. Rev. Lett. **52**, 997 (1984).

[35] R. van Leeuwen, Phys. Rev. Lett. **80**, 1280 (1998).

[36] G. F. Giuliani and G. Vignale, *Quantum Theory of the Electron Liquid*, Cambridge university press, Cambridge, 2005.

[37] E. K. U. Gross and W. Kohn, Phys. Rev. Lett. **55**, 2850 (1985).

[38] H. Ehrenreich, Electromagnetic transport in solids: Optical properties and plsma effects, in *Rendiconti della scuola internazionale di Fisica Enrico Fermi, XXXIV corso, Proprietá ottiche dei solidi*, edited by J. Tauc, page 106, Academic Press, New York, 1966.

[39] S. L. Adler, Phys. Rev. **126**, 413 (1962).

[40] N. Wiser, Phys. Rev. **129**, 62 (1963).

[41] M. S. Hybertsen and S. G. Louie, Phys. Rev. B **35**, 5585 (1987).

[42] L. Caramella, G. Onida, F. Finocchi, L. Reining, and F. Sottile, Phys. Rev. B **75**, 205405 (2007).

[43] E. G. Maksimov, I. I. Mazin, S. N. Rashkeev, and Y. A. Uspensky, J. Phys. F: Met. Phys. **18**, 833 (1988).

[44] A. Marini, G. Onida, and R. Del Sole, Phys. Rev. B **64**, 195125 (2001).

[45] F. Sottile, *Response functions of semiconductors and insulators: from the Bethe-Salpeter equation to time-dependent density functional theory*, PhD thesis, Ecole Polytechnique, 2003.

[46] L. Reining, V. Olevano, A. Rubio, and G. Onida, Phys. Rev. Lett. **88**, 066404 (2002).

[47] S. Rahman and G. Vignale, Phys. Rev. B **30**, 6951 (1984).

[48] M. Corradini, R. Del Sole, G. Onida, and M. Palummo, Phys. Rev. B **57**, 14569 (1998).

[49] S. Moroni, D. M. Ceperley, and G. Senatore, Phys. Rev. Lett. **75**, 689 (1995).

[50] K. Tatarczyk, A. Schindlmayr, and M. Scheffler, Phys. Rev. B **63**, 235106 (2001).

[51] K. Sturm, Adv. Phys. **31**, 1 (1982).

[52] K. Sturm and L. E. Oliveira, Phys. Rev. B **24**, 3054 (1981).

[53] E.-N. Foo and J. J. Hopfield, Phys. Rev. **173**, 635 (1968).

[54] K. Sturm and L. E. Oliveira, Phys. Rev. B **30**, 4351 (1984).

[55] M. M. Rieger, L. Steinbeck, I. D. White, H. N. Rojas, and R. W. Godby, Comp. Phys. Comm. **117**, 211 (1999).

[56] G. Onida, L. Reining, R. W. Godby, R. Del Sole, and W. Andreoni, Phys. Rev. Lett. **75**, 818 (1995).

[57] L. Reining, G. Onida, and R. W. Godby, Phys. Rev. B **56**, R4301 (1997).

[58] M. Rohlfing, P. Krüger, and J. Pollmann, Phys. Rev. B **48**, 17791 (1993).

[59] M. Palummo, R. Del Sole, L. Reining, F. Bechstedt, and G. Cappellini, Solid State Comm. **95**, 393 (1995).

[60] S. Massidda, A. Continenza, M. Posternak, and A. Baldereschi, Phys. Rev. B **55**, 13494 (1997).

[61] J. A. Soininen, J. J. Rehr, and E. L. Shirley, J. Phys.: Condens. Matter **15**, 2573 (2003).

[62] `http://www.abinit.org`.

[63] X. Gonze et al., Zeit. Kristall. **220**, 558 (2005).

[64] M. Cazzaniga, N. Manini, L. G. Molinari, and G. Onida, Phys. Rev. B **77**, 035117 (2008).

[65] M. Stankovski, private communication.

[66] J. E. Northrup, M. S. Hybertsen, and S. G. Louie, Phys. Rev. B **39**, 8198 (1989).

[67] I.-W. Lyo and E. W. Plummer, Phys. Rev. Lett. **60**, 1558 (1988).

[68] H. J. Levinson, F. Greuter, and E. W. Plummer, Phys. Rev. B **27**, 727 (1983).

[69] W. Schülke, J. Phys.: Cond. Mat. **13**, 7557 (2001).

[70] M. Ehrnsperger and H. Bross, J. Phys.: Cond. Mat. **9**, 1225 (1997).

[71] W. Schülke, J. R. Schmitz, H. Schulte-Schrepping, and A. Kaprolat, Phys. Rev. B **52**, 11721 (1995).

[72] Y. Takada and H. Yasuhara, Phys. Rev. Lett. **89**, 216402 (2002).

[73] C. Sternemann et al., Phys. Rev. Lett. **95**, 157401 (2005).

[74] B. C. Larson et al., Phys. Rev. Lett. **77**, 1346 (1996).

[75] B. C. Larson et al., J. Phys. Chem. Sol. **61**, 391 (2000).

[76] J. Z. Tischler, B. C. Larson, P. Zschack, A. Fleszar, and A. G. Eguiluz, Phys. Stat. Sol. (b) **237**, 280 (2003).

[77] G. Tirao, G. Stutz, V. M. Silkin, E. V. Chulkov, and C. Cusatis, J. Phys.: Cond. Mat. **19**, 046207 (2007).

[78] I. G. Gurtubay et al., Phys. Rev. B **72**, 125117 (2005).

[79] I. G. Gurtubay, J. M. Pitarke, I. Campillo, and A. Rubio, J. Comp. Mat. Sci. **22**, 123 (2001).

[80] S. Huotari, T. Pylkkane, and G. Monaco, private communication.

[81] `http://www.dp-code.org`.

[82] A. vom Felde, J. Sprösser-Prou, and J. Fink, Phys. Rev. B **40**, 10181 (1989).

[83] A. A. Quong and A. G. Eguiluz, Phys. Rev. Lett. **70**, 3955 (1993).

[84] K. Sturm and A. Gusarov, Phys. Rev. B **62**, 16474 (2000).

[85] K. W. K. Shung, B. E. Sernelius, and G. D. Mahan, Phys. Rev. B **36**, 4499 (1987).

[86] W.-D. Schöne, R. Keyling, M. Bandić, and W. Ekardt, Phys. Rev. B **60**, 8616 (1999).

[87] I. Campillo et al., Phys. Rev. B **61**, 13484 (2000).

[88] J. S. Dolado, V. M. Silkin, M. A. Cazalilla, A. Rubio, and P. M. Echenique, Phys. Rev. B **64**, 195128 (2001).

[89] S. Albrecht, L. Reining, R. Del Sole, and G. Onida, Phys. Rev. Lett. **80**, 4510 (1998).

[90] E. D. Palik, *Handbook of optical constants of solids*, Academic Press, San Diego, 1998.

[91] H. Ehrenreich, H. R. Philipp, and B. Segall, Phys. Rev. **132**, 1918 (1963).

[92] L. X. Benedict, E. L. Shirley, and R. B. Bohn, Phys. Rev. B **57**, R9385 (1998).

[93] P. E. Batson and J. Silcox, Phys. Rev. B **27**, 5224 (1983).

[94] L. Caramella, *Theoretical spectroscopy of realistic condensed matter systems*, PhD thesis, Universitá degli Studi di Milano, 2008.

[95] P. B. Johnson and R. W. Christy, Phys. Rev. B **9**, 5056 (1974).

[96] V. P. Zhukov, E. V. Chulkov, and P. M. Echenique, Phys. Rev. Lett. **93**, 096401 (2004).

[97] D. L. Misell and A. J. Atkins, Philosophical Magazine **27**, 95 (1973).

[98] W. S. M. Werner, Surf. Sci. **601**, 2125 (2007).

[99] B. Egert and G. Panzner, J. Phys. F: Metal Phys. **11**, L233 (1981).

[100] P. Nozieres and D. Pines, *The Theory of Quantum Liquids*, Perseus books, Cambridge, 1966.

[101] S. K. Sinha, J. Phys.: Condens. Matter **13**, 7511 (2001).

[102] G. Grosso and G. Pastori Paravicini, *Solid State Physics*, Academic Press, San Diego, 2003.

Acknowledgements

First of all I want to thank my supervisor Prof. Giovanni Onida for permitting me to perform this thesis work and for all the scientific and non scientific support during these three years. I would like to thank also all the people who helped me as cosupervisor at different levels: Dr. Nicola Manini, Dr. Luca Guido Molinari, Dr. Lucia Reining and Dr. Hans-Christian Weissker. I am grateful to them not only because they taught me the researcher's work, but also because they gave me the great opportunity of working in very stimulating places and groups in Milan, Paris and Grenoble. A particular acknowledgement is for Dr. Nicola Manini and for the referee of this thesis Dr. Andrea Marini for their careful reading of this manuscript. Another acknowledgement is for my mentor Prof. Rex Godby for his precious insight of the scientific community.

I would like to acknowledge the institutions which provided support during this work, starting from my institution, the Physics department of the Università degli Studi di Milano, and the Laboratoire des Solids Irradies of the Ecole Polytechique for guesting me during my PhD. My gratitude is addressed also to the NANOQUANTA network of excellence and the ETSF, which permitted me to interact with a large number of scientists from the whole Europe. It is dutiful to mention also the ESFR for the beam time used to perform some of the experiments dealt in this thesis and the CINECA for providing computing time.

I would like to thank also all the people I had occasion to work and discuss with in these three years, especially Dr. Katalin Gaal-Nagy, Dr. Francesco Sottile, Dr. Guido Fratesi, Dr. Valerio Olevano, Dr. Matteo Gatti, Dr. Pina Romaniello and the experimentalists I worked with during this thesis work Dr. Giulio Monaco, Dr. Simo Huotari and Dr. Jorge Serrano. I am also grateful to all the people I had occasion to discuss with at the different conferences I attended, in particular: Dr. Claudio Verdozzi, Dr. Pablo Garcia-Gonzales, Martin Stankovski, Dr. Fabien Bruneval.

Let me acknowledge also all the people I shared the office and the working time with in these years starting from Lucia Caramella. Now it is the turn of all the people in Milan (I omit the ones already cited): Andrea Bordoni, Andrei Incze, Davide Sangalli, Tereza Sedivcova, Carlo Motta and Federico Bonelli; and the people in Paris: Arian Berger, Julien Vidal, Eleonora Luppi, Wojtek Welnic, Federico Iori.

Let me conclude by thanking also the system managers of Milan and Paris, Paolo Salvestrini and Andrea Cucca, because without their help I would not have been able to perform all the computation required by this work.